Hot electrons in cool nanocrystals

de Weerd, C.

Publication date
2018
Document Version
Final published version
License
Other

Hot electrons in cool nanocrystals

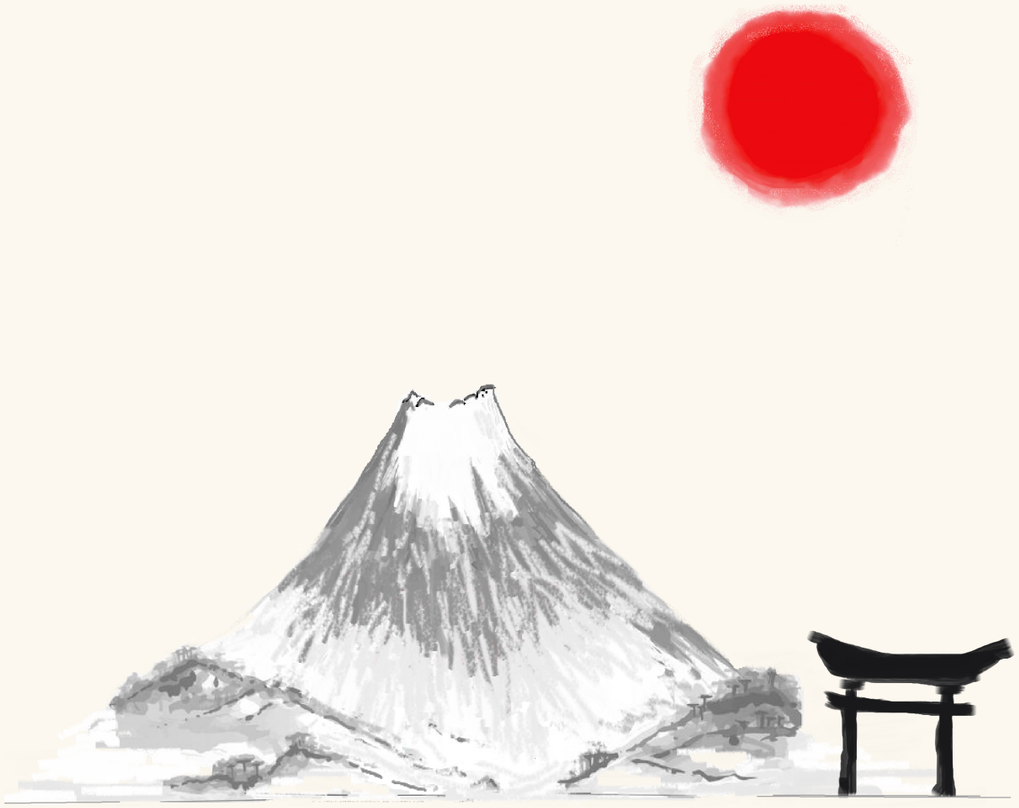

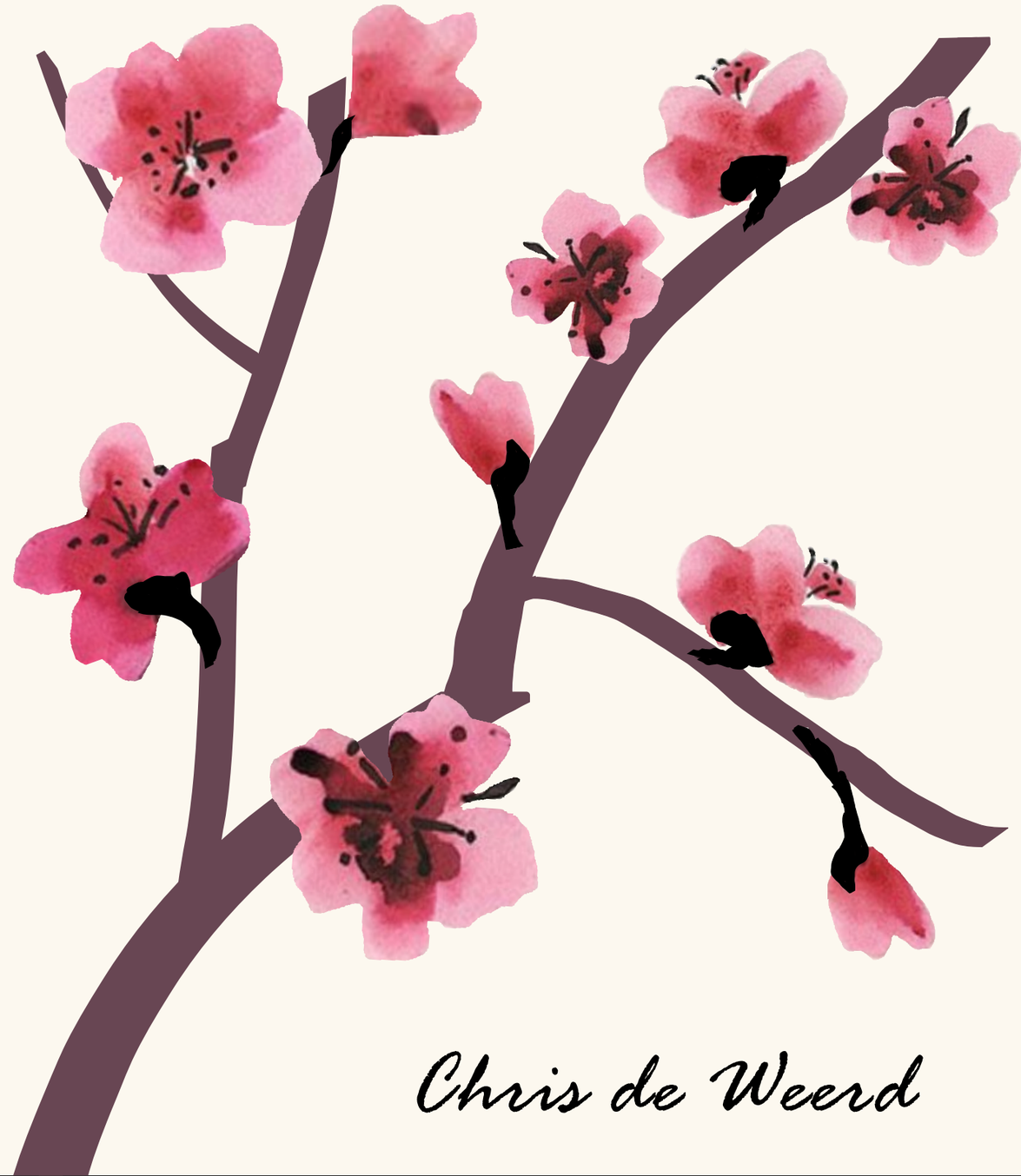

Chris de Weerd

Hot electrons in cool nanocrystals

Chris de Weerd

ISBN: 978-94-028-1151-3

Cover design by:

Hot electrons in cool nanocrystals

ACADEMISCH PROEFSCHRIFT

ter verkrijging van de graad van doctor
aan de Universiteit van Amsterdam
op gezag van de Rector Magnificus
prof. dr. ir. K.I.J. Maex
ten overstaan van een door het College voor Promoties
ingestelde commissie,
in het openbaar te verdedigen in de Agnietenkapel
op donderdag 4 oktober 2018, te 12:00 uur

door

Chris de Weerd

geboren te Alkmaar

Promotiecommissie:

Promotores:	Prof. dr. T. Gregorkiewicz	Universiteit van Amsterdam
	Prof. dr. W.C. Sinke	Universiteit van Amsterdam
Overige leden:	Prof. dr. J. Linnros	Royal institute of Technology, Stockholm
	Prof. dr. L.D.A. Siebbeles	Technische Universiteit Delft
	Prof. dr. J. Gómez Rivas	Technische Universiteit Eindhoven
	Prof. dr. M.S. Golden	Universiteit van Amsterdam
	Prof. dr. P. Schall	Universiteit van Amsterdam
	Prof. dr. H Zhang	Universiteit van Amsterdam

Faculteit der Natuurwetenschappen, Wiskunde en Informatica

UNIVERSITY OF AMSTERDAM

The work described in this thesis was performed in the group of Tom Gregorkiewicz (TGG) at the Institute of Physics at the University of Amsterdam, Science Park 904 1098 XH Amsterdam. It is part of and financed by the research programme (A1604M) of the Netherlands Organization for Scientific Research (NWO).

Contents

List of frequently used abbreviations

Abbreviation:	Description:
ADF	Atomic dark field
AR	Auger recombination
CCD	Charged coupled device
CM	Carrier multiplication
DLS	Dynamic light scattering
EDS	Energy-dispersive X-ray spectroscopy
EELS	Electron energy loss spectroscopy
Ge	Germanium
(HR)-TEM	(High resolution) transmission electron microscopy
IP-NC(s)	All-inorganic perovskite nanocrystal(s)
LED(s)	Light emitting diode(s)
MEG	Multiple exciton generation
NIR	Near-infrared
OD	Optical density
PIB	Photo-induced bleach
PIA	Photo-induced absorption
PL	Photoluminescence
PMT	Photomultiplier tube
PV	Photovoltaics
QC	Quantum confinement
QY	Quantum yield
Si	Silicon
(S)TEM	(Scanning) transmission electron microscopy
TA	Transient absorption
UV	Ultraviolet
XRD	X-ray diffraction
ZLP	Zero-loss peak

1

Introduction

This Chapter contains a brief introduction to each of the different concepts and topics that play a central role in this thesis. Approximately five years ago, the project started with a clear focus on silicon and germanium nanocrystals, which stood at the center of the research in TGG. Quite soon however, the bright and colorful perovskite nanocrystals made their introduction and turned our plans upside down. Gradually but definitively, the subject of many of our studies smoothly transitioned towards this new fascinating family of materials. Owing to their direct band gap and high optical activity, the perovskites lend themselves very well for optical spectroscopy, which is at the heart of this thesis. In addition, they are also extremely suitable for single nanoparticle analysis through e.g. microscopy, which we performed with our collaborators in Japan. This resulted in many beautiful experiments and studies, and eventually papers, most of which are discussed in this thesis.

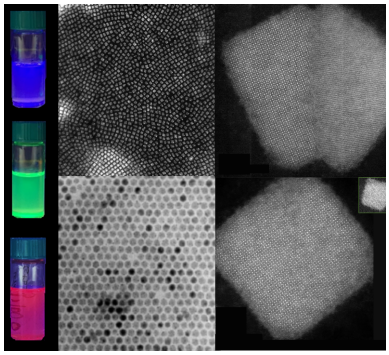

1.1 Synergy of this thesis

In this introductory Chapter, the semiconductor materials which are addressed in this thesis are introduced, in their respective order of appearance. First, the all-inorganic perovskite nanocrystals (IP-NCs) are discussed and their general optical and structural properties are summarized. The subsequent eight Chapters are solely devoted to IP-NCs. The introduction concludes with an overview concerning the general characteristics of silicon, germanium and graphene NCs, that are the three materials whose optical properties are compared in the last Chapter of this thesis. In each Chapter, the experimental techniques that were used and are relevant for the discussed study, are described. Chapter 2 discusses carrier multiplication in $CsPbI_3$ NCs which is revealed by ultrafast transient absorption spectroscopy. An additional fast component is systematically investigated in the photo-induced bleach transients; we argue that it arises due to Auger recombination of multiple excitons, appearing in one NC upon absorption of a single photon of sufficiently large energy above twice the band gap energy. The results also provide a unique and new insight into the carrier multiplication mechanism. In Chapter 3, important insights into the energy structure of $CsPbBr_3$ NCs are revealed as well as a coupling between individual NCs. This is done by making use of electron energy loss spectroscopy (EELS) and scanning transmission electron microscopy (STEM). A comparison is made between the absorption spectrum of isolated and ensemble embedded single NCs, which demonstrates that neighboring NCs couple with each other and thereby modify their energy structure. While preparing $CsPbBr_3$ NCs, the synthesis can also yield insulating Cs_4PbBr_6 NCs, in addition to the semiconducting IP-NCs. This is discussed in Chapter 4 where it is shown that the two phases are independent of each other's presence but can also hybridize. Existing controversies in the literature regarding the optical properties of the two materials are discussed, and conclusively resolved by studying single $CsPbBr_3$ and Cs_4PbBr_6 NCs. In Chapter 5, it is revealed that upon drop-casting, a layer of single IP-NCs can spontaneously merge into larger nanostructures without visible defects. It is shown that the merging process is promoted by humidity and mild temperature treatments and can be arrested by electron beam irradiation. Apart from an effective coupling, also energy transfer between proximal NCs is demonstrated, which is described in Chapter 6. The transfer is driven by the concentration gradient of excited NCs in the colloid and/or by the band gap energy difference induced by the NC's size. Next, in Chapter 7 the encapsulation of IP-NCs is addressed, which solves the problem of them being incompatible with polar solvents. In addition, it is shown that the encapsulation stabilizes the chemical composition of IP-NCs, and the typically occurring halide exchange is completely arrested. In Chapter 8, photon recycling in $CsPbBr_3$ NCs is investigated using optical spectroscopy. The spectral changes induced by increasing the NC concentration, as well as changing the distance between excitation and emission collection, are studied. All experimental results are compared with the calculated prediction based on the Beer-Lambert law. The observed discrepancy between the experiment and the prediction, provides the most direct evidence of photon recycling. Chapter 9 summarizes the potential of the IP-NCs for different devices and applications and serves as an outlook. Finally, Chapter 10 addresses the optical properties of butyl-terminated silicon and germanium NCs, which are compared with those of graphene NCs. The discussed observations indicate a different microscopic origin for the absorption and radiative recombination mechanisms - which is the case for all three investigated NC systems.

1.2 Perovskite materials

Maybe the most researched material in the last few years, are the metal halide semiconductors with perovskite structure. The optimal range of band gap energy values, high emission efficiencies and good carrier mobilities with a high defect tolerance [1] make them very suitable for various applications. Much of the progress in this research field has been obtained for the organic-inorganic hybrid perovskites [2–4] (e.g. $CH_3CH_3PbI_3$, $CH_3NH_3PbI_3$, etc.) with the general formula $APbX_3$, where the A stands for an organic group and X is a halide atom (Cl, Br or I). However, for demanding and large-scale applications, such as photovoltaics (PV), excellent long-term chemical and structural stability under extreme operating conditions is a necessity. For these hybrid materials, this has not yet been demonstrated at a sufficient level. Very recently, the synthesis of $CsPbX_3$ (X = Cl, Br, I) IP-NCs has been developed, replacing the organic cation with the less volatile Cs. [5] The IP-NCs combine the advantages of perovskites (low-temperature/low cost production, band gap tuning by composition) with the typical NC features induced by quantum confinement (QC), e.g. band gap tunability by size, and a possibility of surface functionalization. [5–7] At the same time, being free from the organic component, the IP-NCs pose an improvement with respect to the stability, which makes them attractive candidates for a diverse range of PV and optoelectronic applications, for instance solar cells, LEDs, lasers and detectors. [2, 8–12] The outstanding characteristics of this novel material and the application potential in optoelectronics and PV [13–16] stimulated related investigations of stability, [17] improvements regarding the tunability of the optical properties, [18] and lasing. [19] It also has stimulated the chemistry labs to focus their efforts on development of synthesis protocols that could yield high quality NCs with easy methods and high output.

In addition to the hot-injection technique reported first, [5] a number of different fabrication procedures have been proposed, such as reprecipitation at room temperature, [20] single-step non-injection method, [21] microfluidic systems, [22, 23] open-air syntheses, [24] inks, [25] room-temperature and gram-scale process, [26] etc. In a parallel effort, the development of lead-free perovskite NCs has been also pursued. [27, 28] Even though new results are daily being added to the vastly extending literature on this nanomaterial, [29] there remain many unanswered questions within this versatile and exciting research field.

1.2.1 General optical characterization

The IP-NCs feature extremely efficient emission [30] and fast radiative recombination [31] which are the major reasons for their popularity within the optoelectronic and photonic community. By using a variety of precursors during synthesis and changing the halide, their emission color can be easily adjusted. [7] In that way, their chemical composition can be precisely tuned yielding different optical properties. Figure 1.1a shows an exemplary image of the IP-NCs with different compositions of the halide atoms and/or a combination, under UV illumination (λ_{exc} = 365 nm). The corresponding PL and absorption spectra are presented in figure 1.1b (dotted and solid lines, respectively), showing that the whole visible range of wavelengths can be covered. By changing the reaction temperature, the NC size can be conveniently controlled ($\sim$ 4-15 nm), which allows for further fine tuning of the emission color. The IP-NCs feature short radiative recombination times ($>$1-30 ns, figure 1.1c) and extremely high PL quantum yields, between 50-90%, with narrow

emission band widths, a sharp absorption onset and a narrow size distribution. Figure 1.1d shows an atomic dark field (ADF) TEM image of fresh drop-casted $CsPbBr_3$ NCs and it illustrates their monodispersity. This can be more clearly observed in figure 1.1e, where a high-resolution ADF image of the NCs is presented, revealing their (almost) cubic orientation and shape which corresponds to the perovskite structure.

1.2.2 Crystal structure, phase transitions, and stability

In order to efficiently tune the optical properties of IP-NCs, it is crucial to understand their structure-property relationship, which requires precise knowledge of the crystallographic structure. It is well-known that $CsPbX_3$ crystallizes in orthorhombic, tetragonal, and cubic symmetries, where at high temperatures the cubic structure generally appears. [32–34] At lower temperatures, a phase transition to a perovskite phase with lower-symmetry takes place, e.g. at 320 K $CsPbCl_3$ exhibits transition to the tetragonal phase, at 316 K to the orthorhombic phase and at 310 K to the monoclinic phase. Also $CsPbBr_3$ exhibits the cubic phase above room temperature, and at lower temperatures it changes to lower symmetry. [32, 35, 36] However, there are some controversies regarding the phase of $CsPbBr_3$, with studies showing the crystal structure of $CsPbBr_3$ NCs being cubic [5, 37, 38] or orthorhombic. [6] Recent work of Cottingham and Brutchey [39] shows convincing evidence, by synchrotron X-ray total scattering data, that the phase is preferably orthorhombic. The presence of Bragg reflections in their diffraction patterns of $CsPbBr_3$ NCs reveals mostly the orthorhombic structure. The experimental findings of Bertolotti *et al.* [34] confirm this in more detail, by showing that the local structure is indeed not cubic but contains domains which exhibit orthorhombic tilting. They also show that $CsPbI_3$ NCs have an orthorhombic phase, isostructural to that of the γ-$CsPbBr_3$ phase.

Of the three basic halides (Cl, Br and I), the $CsPbCl_3$ and $CsPbBr_3$ NCs proved to be the most stable compositions, but the $CsPbX_3$ perovskite with the more suitable band gap energy for PV applications is the cubic (α-phase) $CsPbI_3$ ($E_{gap} \sim 1.73$ eV). For this material, below 588 K the more thermodynamically favorable orthorhombic phase (δ-phase) is preferred, also known as the "yellow phase", which is insulating. [40] This transformation can be countered by partial substitution of the I anion by Br through synthesizing $CsPb(Br_xI_x)_3$ [41] which stabilizes the structure, but in return upshifts its band gap, which is unfavorable for PV. However, based on an improved synthesis method by Swarnkar *et al.*, using methyl acetate in the purification steps, [42] the α-$CsPbI_3$ NCs can be made stable at room temperature, well below the phase transition temperature for $CsPbI_3$ thin film or bulk materials. Their demonstration of a stable solar cell based on α-$CsPbI_3$ NCs with 13.43% efficiency, [15] changed the status of IP-NCs from being a scientific curiosity to a highly-promising new alternative for perovskite-based PV applications.

1.3 Silicon

Si has a band gap energy of 1.1 eV and falls in close to the range for which the maximum solar conversion efficiency can be achieved, as calculated by Shockley and Queisser in 1961. [43] However, one major drawback is its indirect band gap which results in a low absorption cross section; also light emission from bulk Si is relatively poor. In figure 1.2 the energy dispersion diagram of

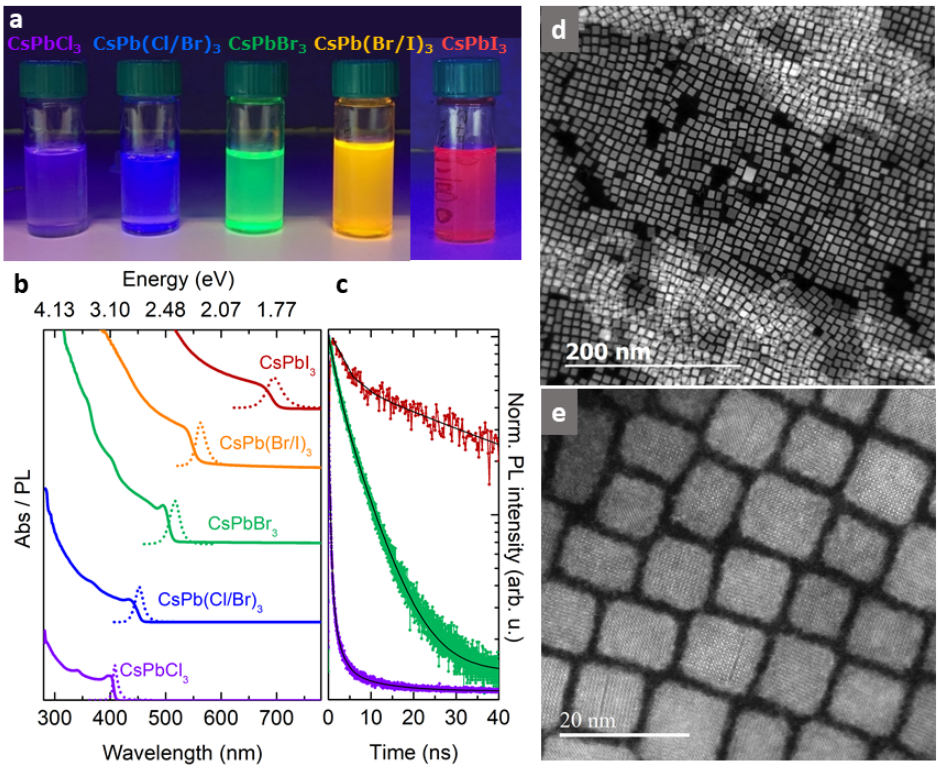

Figure 1.1: General optical characteristics of IP-NCs. (a) Colloidal $CsPbX_3$ (X = Cl, Br, I) exhibit composition tunable band gap energies yielding a variety of emission colors. The photo shows the colloidal solutions' emission under UV lamp illumination (λ_{exc} = 365 nm). (b) Representative PL spectra (dotted lines, λ_{exc} = 430 nm for all but 360 nm for $CsPbCl_3$ NCs) and absorption spectra (solid lines) for the different compositions. (c) Corresponding time-resolved PL decay for the three basic halides, with PL lifetimes between 0.4 - 44 ns. (d) ADF image of freshly drop-casted $CsPbBr_3$ NCs. (e) Atomic resolution ADF image of the same NCs revealing their (nearly) cubic shape and structure.

bulk Si is shown. As can be seen, the optical transition between the lowest and highest possible occupied states in the conduction band minimum and valence band maximum respectively, needs to overcome a difference in $\mathbf{k}$-vector between these respective states. The difference between the valence and conduction band at the Γ-point (i.e. where the direct transition is for Si) is $\sim$3.3 eV which is significantly higher. The recombination of an electron and hole pair across the indirect band gap

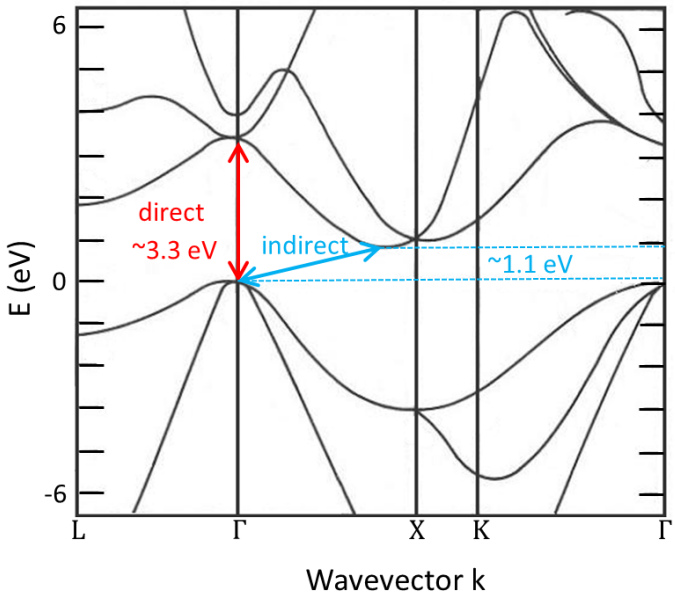

Figure 1.2: The energy dispersion diagram for bulk Si. Due to a mismatch in momentum, the transition from the lowest state in the conduction band to the highest state in the valence band is indirect, which makes it an indirect band gap material. The creation or recombination of an electron and hole across the indirect band gap therefore needs the assistance of a phonon. Figure adapted from Ref. [44].

must be accompanied by (a) phonon(s) in order to preserve momentum, which significantly lowers its probability. This slow radiative transition competes directly with typically readily available non-radiative recombination.

The in the previous paragraph described low probability of radiative recombination for Si, can be partly overcome in nanostructures. If the size of the NC is reduced to the order of the exciton Bohr radius ($\sim$5 nm in case of Si), QC effects (e.g. discretization of the energy levels, opening of the band gap and the so-called *phonon bottleneck* effect) start playing a role - as was also briefly mentioned in section 1.2. Moreover, it follows from Heisenberg's uncertainty relation that the wave function distribution becomes more spread in $\mathbf{k}$-space (as compared to bulk) because the electronic states are strongly localized in real space due to the confinement of the charge carriers. Consequently, the probability for a zero-phonon/no-phonon assisted optical transition is increased i.e. resulting in a higher probability of radiative recombination. Slightly different transitions that occurred at almost similar energies in bulk material, are now confined into a single intense transition in a NC. [45] As such, the radiative lifetime of Si is decreased from milliseconds in bulk material to tens of microseconds in a Si NC.

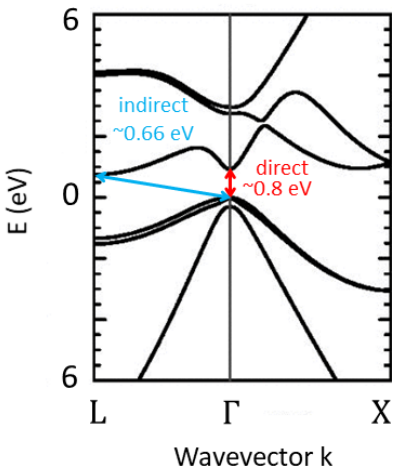

Figure 1.3: The energy dispersion diagram for bulk Ge. Like Si, the top of the valence band is located at the Γ-point, but the bottom of the conduction band is at the L-point. Therefore, Ge is an indirect band gap semiconductor although, the difference between its direct and indirect band gap is only 140 meV. Figure adapted from Ref. [56].

1.4 Germanium

Germanium (Ge) is a semiconductor with an appearance similar to Si, both having a diamond-like crystal structure. Even though it is much less abundant than Si, Ge finds its uses in transistors and integrated circuits, but also in fiber-optics and infrared spectrometers and detectors. Its band structure can be seen in figure 1.3. The top of the valence band is located at the Γ-point and the bottom of the conduction band at the L-point, corresponding to an indirect band gap with an energy of 0.66 eV. The difference between the indirect and direct transitions is only 140 meV, and it has been shown that the crossover occurs from indirect to direct band gap when Ge is submitted to a tensile strain of only 1.9%. [46] As such, Ge can become a direct band gap semiconductor. [47] This invites possibilities of using Ge as an active layer in optoelectronic devices that could be fully compatible with the existing microelectronic Si technology.

Ge has, compared to Si, a larger Bohr radius of ∼18 nm and the optical properties of nanometer sized Ge have been investigated in the past. Several groups report on the visible emission from thin films containing Ge NCs in SiO_2, [48–51] whereas Takeoka *et al.* observed near-infrared emission from Ge NCs dependent on their size [52, 53]. More recently, we have demonstrated that carrier multiplication occurs in Ge NCs in a glassy matrix. [54] This is an impactful result, as a 44% theoretical maximum power conversion efficiency in solar cells, was calculated by A.J. Nozik for semiconductors with band gaps in the range of 0.6 - 1.0 eV, which is exactly within reach of Ge NCs. [55]

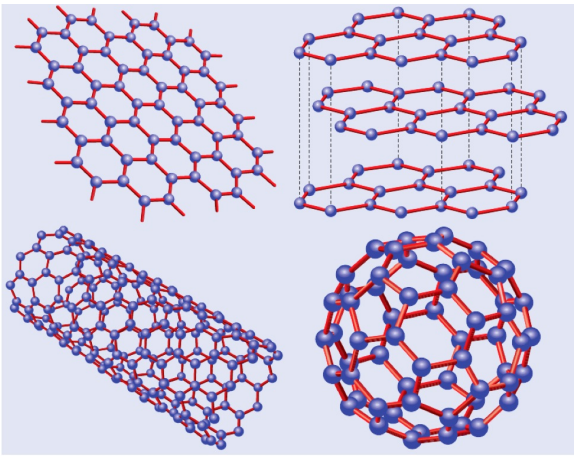

Figure 1.4: Graphene and a few of its allotropes. Top left: graphene; top right: graphite i.e stacked graphene and a basis for GQDs; bottom left: graphene nanotube; bottom right: fullerene. Figure adapted from Ref. [63].

1.5 Graphene

Graphene's unique one-atom-think structure is probably the major reason this material received such enormous interest. Its carbon atoms are packed in a regular hexagonal array, and provides infinite lateral extension, making it a strictly two-dimensional material. Its valence and conduction band just overlap at the Dirac points, making it a zero-band gap semiconductor or semi-metal. Excitons in graphene have an infinite Bohr radius and as a result, QC starts to become effective in graphene fragments of any finite size.

Consequently, graphene NCs have attracted tremendous interest for their unique spin, [57] electronic and optical properties. [58] Potentially, they could be applied in various fields such as optoelectronics, PV, and bio-imaging. They can be prepared through several approaches, by e.g. treatment of various carbon-based materials including graphite or graphene oxide, carbon nanotubes, and carbon fibers. [59–62] Graphene NCs typically comprise of few (mono)layers of graphene sheets, and can have lateral dimensions up to $\sim$100 nm. Past reserach shows that remarkably strong QC and edge effects appear in graphene NCs.

2

Efficient carrier multiplication in $CsPbI_3$ nanocrystals

The process of carrier multiplication in semiconductor NCs counteracts the loss of energy through thermalization of hot carriers created upon high-energy photo-excitation. In this Chapter, efficient carrier multiplication in all-inorganic $CsPbI_3$ NCs, with a quantum yield up to 98%, is discussed. The evidence is obtained using ultrafast transient absorption spectroscopy by comparing the photo-induced bleach as well as the photo-induced absorption dynamics at different excitation energies below and above the threshold energy. Upon excitation with sufficiently high photon energy, an additional fast component appears in the transients due to Auger recombination of multiple excitons. This is the generally accepted characteristic fingerprint of carrier multiplication. Subsequently, we systematically evaluate carrier generation yields at different pump energies, obtaining the complete excitation dependence. Finally, we observed that the onset of carrier multiplication is accompanied by the appearance of a longer build-up of free carrier concentration on a picosecond time scale thus providing an important insight into the physical mechanism responsible for the CM effect.

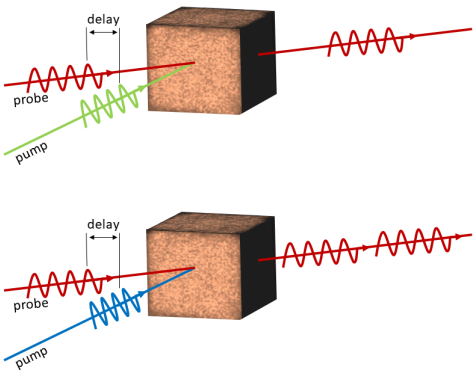

2.1 Introduction

In the process of photoexcitation of a semiconductor, an electron in the conduction band and a hole in the valence band are created, forming an electron-hole (e-h) pair. The photo-generated e-h pair possesses typically an excess energy, equal to the difference between the band gap value of the material and the absorbed photon energy. The hot electron and hole may lose their excess energy by cooling to the band edge by phonon scattering. However, if the excess energy reaches a certain threshold, an interaction between a hot electron (hole) and other valence electrons (holes) can take place instead, such that a second e-h pair is generated. In bulk semiconductors, this phenomenon is known as impact ionization (II) [64] and was first observed in crystalline silicon and germanium. [65] In the case of semiconductor NCs, II is more often referred to as multiple exciton generation or carrier multiplication (CM), and its probability can be enhanced. CM is accompanied by Auger recombination (AR), which is the reverse process of II: [66] an e-h pair can recombine, giving up its energy to another electron or hole, thus increasing its excess energy and creating a hot carrier. Sequential CM and AR can continue until the hot e-h pair has cooled below the CM threshold, e.g., by phonon scattering.

In the last two decades, semiconductor NCs have been widely investigated for their size-tunable properties. As the NC size decreases and approaches the Bohr radius of the particular material, quantum confinement sets in. As such, the nanoparticle dimensionality, and not the e-h Coulomb coupling strength, defines the exciton spatial confinement. Upon confinement, the wave functions of the electron and hole are modified and eventually discrete energy levels replace the continuous energy bands of the bulk material, while the band gap increases. [45] Because of the strong confinement, carrier-carrier Coulomb interactions are enhanced which can give priority to decay via AR, and reversibly, to efficient CM by hot carriers. [67,68] Employing CM for photovoltaic (PV) devices has already proved its benefit and usefulness. [69] In particular, a PV power conversion efficiency up to 44% is expected for cells that make optimal use of CM [55, 70], surpassing the well-known Shockley-Queisser limit of 33%. [43] Indeed, an external photocurrent quantum efficiency (the ratio of photocarriers collected by an external circuit to the number of incident photons) exceeding 100% has been reported. [69] Previously, CM has been demonstrated in many semiconductor (nano)structures, e.g., PbSe, PbS, CdSe, Si, Ge and graphene [54, 69–86], as reviewed by Smith and Binks. [87]

Until now, however, CM has not been reported for perovskites. In case of IP-NCs, CM would be of great fundamental impact on this upcoming material and directly beneficial to its application in novel optoelectronic nanodevices, most notably photodetectors, because the band gaps of the currently available IP-NCs are still too large for practical impact in solar cells. Nevertheless, the research continues vigorously and rapid progress is being made - see, e.g. Ref. [88] for a very recent report on the possible multiple exciton generation in $CsPbBr_3$ upon nonlinear absorption at sub-band energies. That is why CM in IP-NCs is of interest and has been investigated further.

Previous research conducted on IP-NCs, failed to reveal CM: a comparison of PL decay dynamics upon excitation with high ($h\nu > 2\ E_{gap}$) and low ($h\nu < 2\ E_{gap}$) energy photons did not reveal any signatures of CM. [89] Here, we report on the observation of efficient CM in a colloidal dispersion of $CsPbI_3$ NCs, with a band gap energy of 1.78 eV. We explicitly demonstrate the CM

effect using ultrafast transient absorption (TA) spectroscopy in a variety of experimental approaches. By comparing carrier transients at different pump photon energies, we reveal the fingerprint of CM in the form of a fast component induced by AR of multiple e-h pairs appearing in the same NC. The observation is made both for the induced absorption and induced bleach. We confirm the CM effect and evaluate its efficiency by measuring the carrier generation rate as a function of excitation energy. Subsequently, the investigations are reproduced in an independent experimental setup, with somewhat different characteristics, and on newly synthesized materials. In that way, we provide an unambiguous evidence of CM in $CsPbI_3$ NCs.

2.2 Synthesis and microscopic characterization

The $CsPbI_3$ NCs were synthesized by a wet-chemical method, following the slightly modified protocol described in Refs. [5] and [42] (see also the Appendix for detailed information). We used a synthesis temperature of 180 °C in order to steer the production towards NCs with a small band gap energy i.e. larger size. Moreover, large NCs have a larger absorption cross section, and therefore are excited preferentially. The structural characteristics of the NCs is determined using a state-of-the-art low-voltage monochromatic scanning transmission electron microscope with a spatial resolution below 1.6 Å. Figure 2.1a shows the ADF STEM image of the drop-casted NCs with an average size of 11.5 $\pm$ 0.6 nm. A high-resolution ADF image of a 12 nm NC is shown in figure 2.1b. Here, the (nearly) cubic arrangement of the atoms is clearly observed, consistent with the perovskite structure. This is further analyzed by simultaneously performing energy-dispersive X-ray spectroscopy (EDS, figure 2.1c) for elemental identification and core-loss EELS (figure 2.1d). Mainly Cs, Pb and I are detected and the Au signal arises from the reflection of the TEM grid. The Cs:Pb:I ratio, determined from the quantification of the EDS under the L-lines of the corresponding elements, is 1:1:3 with a 10% accuracy, confirming that (mostly) NCs of $CsPbI_3$ have been formed. Extending the range to higher energies, two distinctive peaks at 733 eV and 746 eV are observed, corresponding to $Cs_{M4.5}$, and the broader peak at 700 eV which corresponds to the feature of the $I_{M4.5}$ ionization edge. To determine the band gap of a single NC, imaging and valence-loss EELS collections were performed in parallel, with a high energy resolution. [90–92] In this way, the structural parameters of a single NC were determined, while simultaneously its low-loss EEL spectrum was recorded. A characteristic step appears in the low-loss EEL spectrum, as an electron is excited from the top of the valence band to the conduction band, followed by a steady increase of the signal. This corresponds to the band-to-band absorption, whose magnitude grows as the density of states increases with energy, in analogy with optical absorption. [93] Figure 2.1e shows the low-loss EEL spectrum with the characteristic step, and the simultaneously obtained ADF image of a 12 nm NC - which comes from the edge of the size distribution - and has specifically been chosen because CM is expected to commence for large NCs first. The band gap energy of 1.77 eV is determined by taking the maximum of the first derivative of the spectrum around the absorption onset, as shown by the dotted line.

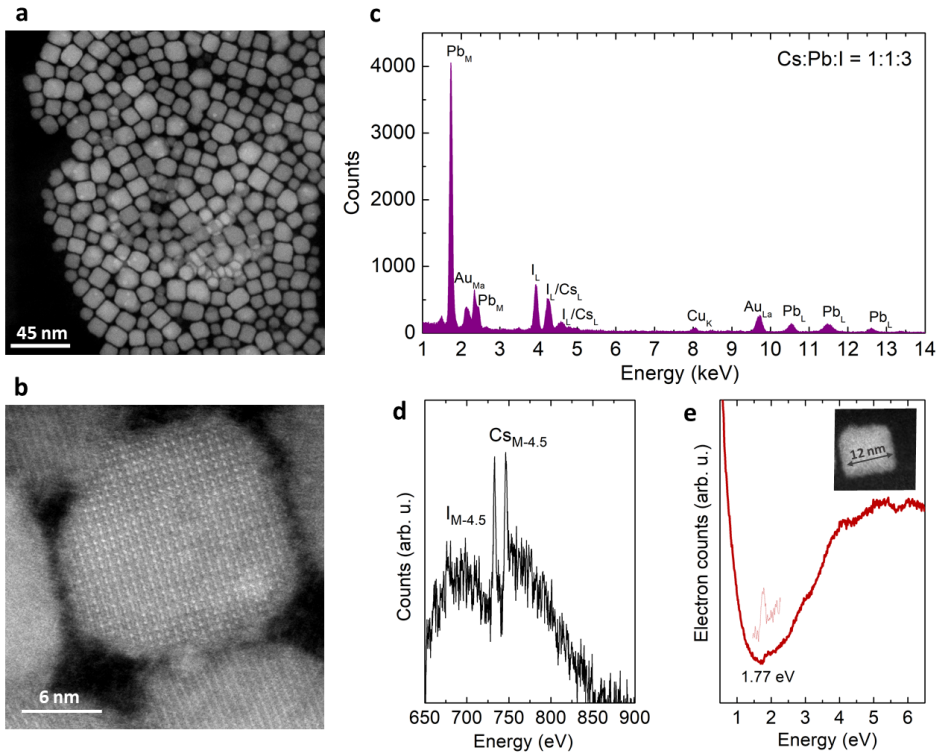

Figure 2.1: Microscopic characterization of the $CsPbI_3$ NCs. (a) ADF image of the freshly drop casted sample. (b) Atomic resolution STEM image of a NC showing clearly their nearly cubic structure (c,d) EDS spectrum of the same sample (c) and core-loss EELS (d) where mainly Cs, Pb and I are detected. The Cs:Pb:I ratio is 1:1:3 $\pm$ 10%, as determined from the quantification of the EDS for the L-lines of the corresponding elements, which suggests (mostly) the perovskite composition. (e) Low-loss EEL spectrum of a large, 12 nm NC, with a band gap energy of 1.77 eV. The dotted line indicates the first derivative of the spectrum around the absorption onset, where its maximum is taken as the NC band gap energy.

2.3 Optical characterization

Figure 2.2 represents the results of ensemble optical spectroscopy measurements. We measured a photoluminescence quantum yield (PL QY) of 42.4$\pm$7% at photo-excitation of energy of 3.1 eV

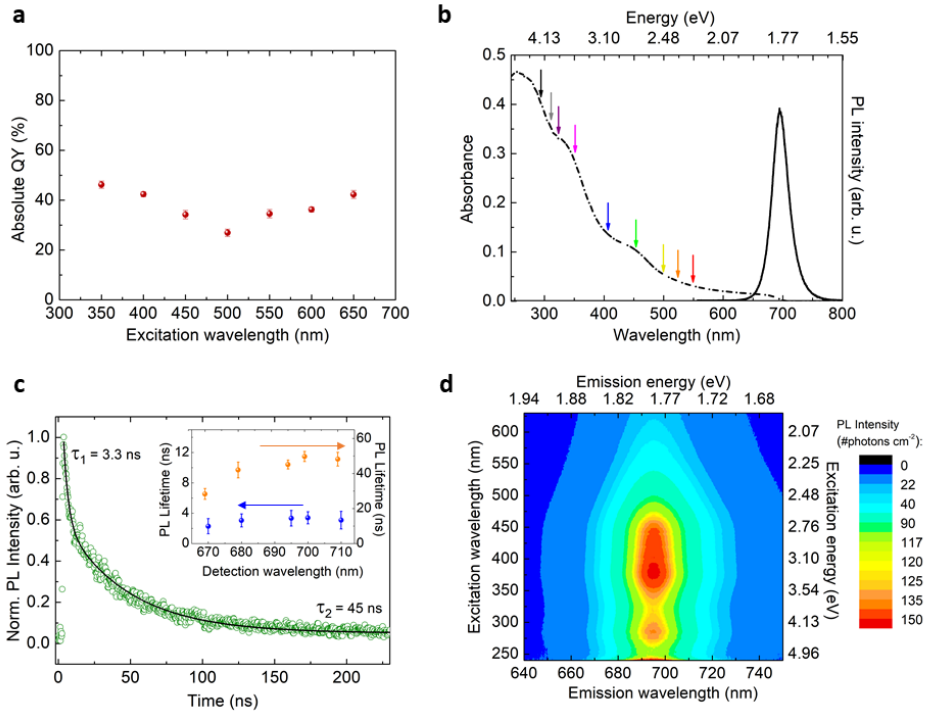

Figure 2.2: Optical characterization. (a) PL QY, the NCs were excited at 3.1 eV (λ_{exc} = 400 nm). (b) Absorbance (dotted) and PL (solid) spectra. The colored arrows indicate the photon energies used in the TA experiment. (c) Time-resolved PL measurement for λ_{det} = 695 nm which was fitted using a bi-exponential function and yielding decay times τ_1 = 3.3 ns and τ_2 = 45 ns. The inset shows the obtained lifetimes for all detection wavelengths. The PL lifetimes with corresponding amplitudes are shown in the inset. (d) 2D contour plot of the PLE, showing the effect of excitation energy on the PL emission and intensity. A PL maximum is observed around <250 nm (>4.96 eV), which could be the first sign of CM. The excitation and emission intensities are corrected for the wavelength dependent components of the setup and spectral sensitivity.

(400 nm, figure 2.2a) which is similar to previously reported values for NCs produced under the employed synthesis conditions. [5,42] Figure 2.2b shows the ensemble optical absorption of the NCs (dotted line) and the PL spectrum (solid line) with the maximum at 1.78 eV (695 nm). The colored

arrows indicate the excitation photon energies that were employed in the TA experiments. The PL lifetimes were measured using a picosecond pulsed diode laser (λ_{exc} = 375 nm) as an excitation source. The normalized decay dynamics for λ_{det} = 695 nm, and extracted lifetimes for the remaining detection wavelengths are shown in figure 2.2c. The transients could be fitted with a bi-exponential function, yielding PL lifetimes of 3.3 and 45 ns with a respective amplitude ratio of 1:2, in a good agreement with previous reports. [42, 89, 94] Figure 2.2d shows the PL excitation (PLE) data where distinctive maxima are observed for excitation energies around 2.8-3.3 eV (440-375 nm), 4.3 eV (290 nm), and 4.96 eV (250 nm). Similar features have been observed before and the maxima at lower energies were attributed to a higher energy state observed in the absorption spectrum. [94] In that case, the PL intensity was significantly reduced for higher excitation energies (>4.6 eV / <270 nm), which was explained by the loss of excess energy through non-radiative recombination. This is clearly not the case in this study: above 4.96 eV (250 nm), we observe a high-intensity emission maximum. We note that, in our experiment, the obtained emission and excitation spectra are corrected for possible wavelength dependent characteristics of the experimental setup. The data is collected as the number of emitted photons per unit area (which remains unchanged throughout the experiment), and in that regard, resembles a PL QY determination. In addition, we recall that in the past for above threshold excitation in Si NCs, an increase of the PL QY was observed which was assigned to CM. [77] As such, the observed increase of the PLE above 4.96 eV, taken together with the NCs absorption spectrum (figure 2.2a), suggests an increase in PL QY which could appear due to CM. [77] Unfortunately, an observation of this phenomenon at still higher excitation energies was not possible due to limitations of the setup.

2.4 Transient absorption spectroscopy

The peculiarity of the PLE spectrum in figure 2.2d motivated the use of TA spectroscopy, which in the past has proved very successful in CM investigation in nanostructures. [54, 72, 73, 95] For direct band gap semiconductors, inter-band photo-induced bleaching (PIB) is often used to study the CM process, while for indirect band gap semiconductors the inter-band absorption is weak, therefore it is easier to monitor the photo-induced absorption (PIA), caused by intra-band transitions of (free) carriers generated by the pump pulse.

In figure 2.3a the pump-probe process is schematically depicted. First, a strong pump pulse (green arrow) provides band-to-band excitation, which in NCs leads to generation of e-h pairs. After photoexcitation, these initially hot e-h pairs relax and bleach the optical absorption at the band edge. A second, weaker pulse (red arrow), probes the carrier concentration as a function of the pump-probe delay time. As a result, the transmittance for photons with energy near the (direct) band gap increases, and yields a negative PIB signal. And reversely, away from the band edges, the transmitted probe light decreases and gives rise to a positive PIA signal. This is schematically depicted in figure 2.3b. The TA signal is defined as the difference of the absorbance or optical density (OD), with and without pump and is obtained as:

$$\Delta OD(t,\lambda) = log_{10}\frac{I_{probe}(\lambda)}{I_{pump+probe}(\lambda)'} \tag{2.1}$$

where $I_{probe}(\lambda)$ and $I_{pump+probe}(\lambda)'$ are the transmitted probe fluences with the pump pulse off and on, respectively. Figures 2.3c and d represent the described pump-probe process with and without CM: if $E_{pump} < 2\ E_{gap}$, only 1 e-h pair is generated which recombines over time. The PIB or PIA signal manifests itself as a single exponential decay. However, if $E_{pump} > 2\ E_{gap}$ and $E_{excess} > E_{gap}$, the excess energy can be used to initialize CM and subsequent AR. The latter gives rise to an additional fast component in the PIB (PIA) signal.

Generally, two approaches are considered to identify CM: (i) the A/B method first applied by Schaller *et al.*, relying on the appearance of a fast component in the transient as the pump energy exceeds the CM threshold, [96] and (ii) the excitation energy dependence of the number of generated carriers (i.e. carrier generation yield), determined by the PIB or PIA amplitude as a function of the absorbed photon fluence. [72, 73, 97, 98] Here, we apply both methods, yielding consistent results. We also consider both the PIB as well as PIA dynamics, yielding results that are in agreement with each other. Since ultrafast spectroscopy setups often have their own characteristics, we repeated our investigations at two different experimental stations, at two laboratories (see Appendix for the experimental details). Our approach (using multiple methods to identify CM and repeating the experiments at two stations) is unique and was followed because of the great experimental difficulty of CM (ultrafast) experiments which are prone to artefacts, as evidenced by the existing literature see, e.g. Ref. [72].

2.5 The fingerprint of carrier multiplication

Figure 2.4 shows the transient PIB measured around its maximum at λ_{probe} = 680 nm (obtained by integrating the signal between 675 - 685 nm). Here, the results for two excitation wavelengths are compared: below and above the CM threshold, at λ_{exc} = 500 nm (1.4 E_{gap}, figure 2.4a) and λ_{exc} = 295 nm (2.4 E_{gap}, figure 2.4b), respectively. While performing our transient PIB measurements, we have maintained the number of absorbed photons per NC at a very low level ($<N_{exc}> << 1$), within the so-called linear regime.

This is confirmed by (i) the fact that the initial amplitude A of the PIB/PIA signal grows linearly with the absorbed photon fluence (orange dots in the insets of figures 2.4a and b), and particularly (ii) by the ratio between the initial amplitude A and the tail amplitude B (A/B) which remains invariant within the investigated absorbed photon fluence range (pink dots). Specifically, from the latter observation, it can be completely excluded that multi-photon absorption occurs. As such, the observed fluence increase in this range yields only a higher number of excited NCs while maintaining $<N_{exc}> << 1$: under these excitation conditions each NC contains at most 1 e-h pair, following absorption of a single photon.

Considering both excitation energies, we note that the behavior of the transient PIB signal is remarkably different: in both cases the dynamics show a tail with a relaxation time which fits the displayed time window (500 ps). However, for the UV excitation, an additional fast component appears. This is commonly taken as a fingerprint of CM, which we will now briefly explain. Here, we follow the reasoning as originally proposed by Schaller *et al.* [96] which has been employed in many studies of CM before [54, 72] - and see also Ref. [83]. A hot carrier can induce CM, if its excess energy is greater than the threshold energy, i.e. at least equal to the NC band gap. A

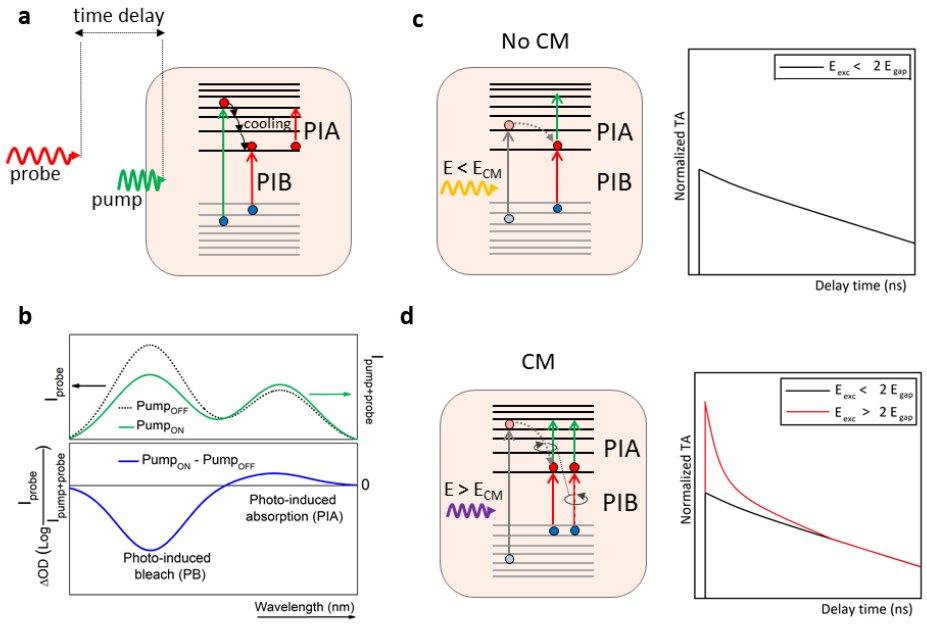

Figure 2.3: Schematic representation of the TA processes with and without CM. (a) An initial pump pulse (green) excited the NCs. Upon the absorption of a high-energy photon, an e-h pair is created. The electron and hole thermalize to their respective band edges in a multi-step phonon emission process. A second pulse (red) probes the carrier concentration as a function of time between the two pulses, giving rise to a PIA and/or PIB signal. (b) Schematic representation of the probe intensity with (green) and without (black, dotted) the pump. The TA signal is defined as the difference between those two (blue).(c) If $E_{pump} < 2\ E_{gap}$ no CM can occur i.e. $E_{excess} < E_{gap}$; and the e-h pair recombines either radiatively or non-radiatively - the PIB (PIA) signal manifests itself in a single exponential decay. (d) If $E_{pump} > 2\ E_{gap}$ the excess energy can be used to excite a second electron across the band gap. Subsequently, the reverse process of AR can occur in competition with cooling via phonon emission. AR gives rise to an additional fast component in the PIB (PIA) signal.

single photo-generated hot e-h pair loses its excess energy by generating an additional e-h pair. This higher exciton multiplicity causes the amplitude increase of the PIB/PIA signal at the short time scale. Subsequently, the multiple excitons localized within the same NC decay through AR. This process typically occurs within 10-100 ps and gives rise to the initial fast component in the measured dynamics. [99] The experimental data shown in figure 2.4 could be fitted with a double and triple exponential function for below and above CM threshold pumping respectively. This yields

τ_1 = ∼89 ps for the fast component for above threshold pumping which agrees with previously reported time constants for the AR process. [89, 99, 100] After the multi-exciton relaxation process, the remaining signal decays through non-radiative and radiative recombination processes, depending on the characteristics of individual NCs, (because the ensemble PL QY $< 100\%$) giving rise to the slow decay. The experimentally found slow decay time constants are τ_2 = ∼190-200 ps and τ_3 = ∼3300 ps, where the latter agrees with the radiative lifetime determined from the time-resolved PL measurements.

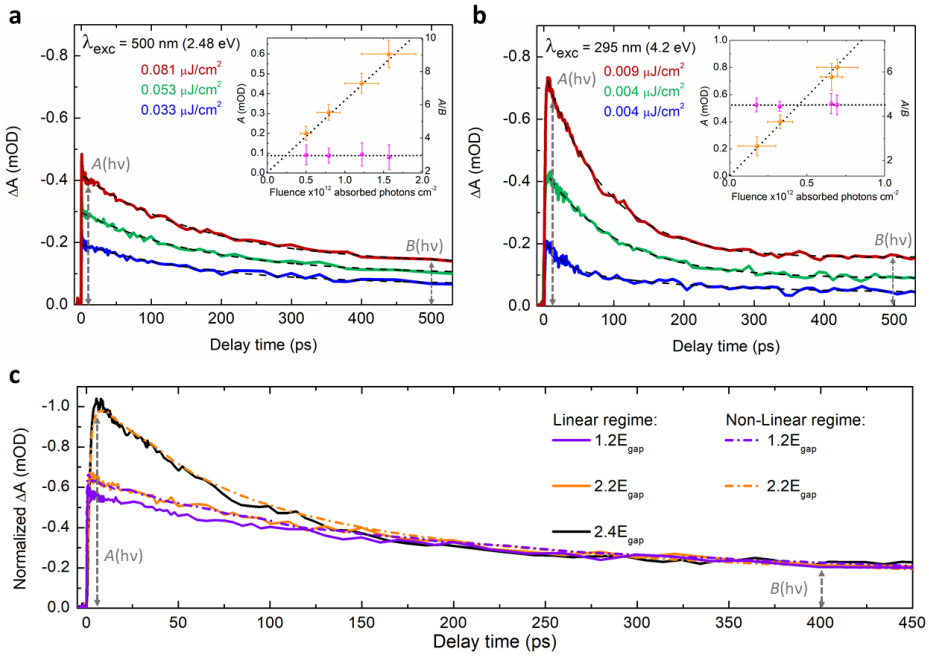

Figure 2.4: TA dynamics measured at probe wavelengths around the PIB maximum (680 nm) by integrating the signal from 675 - 685 nm. (a,b) Dynamics below (a) and above (b) the CM threshold i.e. at pump wavelengths of 500 nm (2.48 eV) and 295 nm (4.2 eV) respectively, for three different pump fluences. The dashed lines represent a single- (a) and double- (b) exponential fit to the data. The appearance of the fast component when pumping at 4.2 eV is the fingerprint of CM. The insets show the initial TA amplitude A and its ratio to the single exciton decay tail A/B, as a function of the absorbed photon fluence, demonstrating the single photon absorption (linear) regime. (c) Linear vs. non-linear regime, showing the decay through AR with pumping outside the linear regime (i.e. by multi-photon absorption) and through CM, yields the same dynamics.

To prove that the initial fast component is indeed due to AR, we show that it can be reproduced by increasing the pump fluence at below-threshold pump photon energy such that the multi-photon

absorption occurs. Figure 2.4c shows the transients for the highest pump fluences in the linear regime (solid lines) which can be reached, far below (1.2 E_{gap}, purple), just above (2.2 E_{gap}, orange), and above (2.4 E_{gap}, black) the CM threshold excitation. The dynamics are normalized to the same B value such that the increase of the fast component can clearly be distinguished. Then, the pump fluence for the below-threshold excitation at 1.2 E_{gap} is increased, until its initial amplitude A matches that of the transient obtained for the above-threshold excitation at 2.2 E_{gap} in the linear regime. And similarly, the pump fluence at 2.2 E_{gap} is increased until it reaches A for exciting at 2.4 E_{gap} in the linear regime (dotted lines). It can be clearly seen that the transients obtained under these two excitation conditions (in- and outside of the linear regime) are practically identical, which confirms that the initial fast component is induced by AR: the decay through AR of multiple e-h pairs induced by multi-photon absorption and by CM has identical characteristics, as could be anticipated.

2.6 Carrier multiplication efficiency

Having obtained the fingerprint of CM, we now study its dependence on the pump fluence and excitation energy. In that case, the initial amplitude A serves as a measure for the number of generated e-h pairs. Following the approach of Beard *et al.*, [101] ΔA is related to the CM QY via:

$$\Delta A = QY \cdot F_{abs} \tag{2.2}$$

where F_{abs} is the absorbed photon fluence. For each excitation wavelength and corresponding pump power, F_{abs} is calculated via:

$$F_{abs} = \frac{P_{pump} \cdot \lambda \cdot OD(\lambda_{pump})}{f} \tag{2.3}$$

where P_{pump} is the pump power at the sample position and corrected for a possible mismatch in pump/probe overlapping area; λ is the excitation wavelength; $OD(\lambda_{pump})$ is the optical density determined from the linear absorption measurement and f is the laser frequency, which is setup specific. As has been demonstrated in figures 2.4a and b, ΔA has a linear function passing through the origin and it follows from equation 2.3 that its slope determines the carrier generation yield. Accordingly, figure 2.5a shows ΔA as a function of F_{abs}. At each pump energy, this value is determined for all pump fluences in the linear regime (as previously explained, the linear regime is mainly confirmed through invariance of the A/B ratio of the decay transients). Without multiple carrier generation i.e. below the CM threshold, this slope should remain constant for different pump energies, which is indeed the case.

In figure 2.5a the red data points correspond to the pump energies $E_{exc} < 2.75$ eV $< 2\ E_{gap}$ and follow the same linear dependence, which subsequently determines the QY = 1 line. From this it follows that the QY = 2 line is determined by the doubling of ΔA at equal fluence. In that way, the slope of the linear function through ΔA for each specific pump energy is a measure for the QY efficiency. Note that in figure 2.5a the slope gradually increases for pump energies above the CM

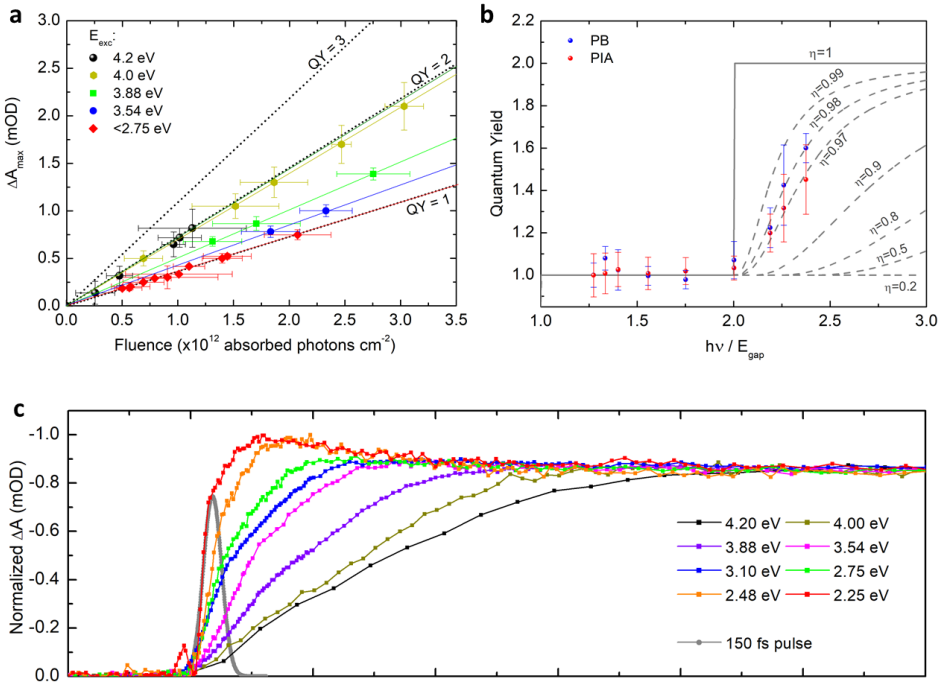

Figure 2.5: CM efficiency and AR. (a) ΔA as a function of the absorbed photon fluence. The solid lines represent a linear fit through the data points. (b) CM efficiency plotted as a function of excitation energy normalized to the band gap energy of the $CsPbI_3$ NCs. The blue and red data points correspond to the yield calculated from the A/B ratios deduced from the PIB and PIA respectively. (c) Initial rise of the PIB signal (normalized) which becomes slower when the NCs are excited with higher photon energies, and CM sets in.

threshold i.e. $E_{exc} \geq 3.54$ eV $\geq 2\ E_{gap}$, rather than jumping to the QY = 2 position (blue and green curves). This is among others a result of the NC size distribution on CM, which commences first for the large NCs, with a smaller band gap energy. We find that at 4.0 - 4.2 eV excitation (2.2 - 2.4 E_{gap}) the ΔA lines are nearly equal to QY = 2 (dark yellow and black). The error bars in the y-direction are determined by the averaging between t = 4 - 8 ps after photo-excitation, to extract ΔA and its corresponding upper and lower limits. In the x-direction, the error is determined by the upper and lower values of the determined pump power in between consecutive measurements.

ΔA in figure 2.5a only takes into account the initial amplitude as a measure for the number of e-h pairs. However, to determine the exact QY value, their multiplicity should be normalized to the B value since our transients do not decay to zero within the available time window. In that way, the experimental CM yield $\varphi(h\nu)$ can be determined from the A/B ratio at a specific energy $E_{exc} > 2$

E_{gap}, scaled to the value corresponding to below CM threshold pumping, via:

$$\varphi(h\nu) = \frac{A(h\nu)/B(h\nu)}{A(1.2E_{gap})/B(1.2E_{gap})} \tag{2.4}$$

Figure 2.5b shows $\varphi(h\nu)$ as a function of the pump energy normalized to the NCs band gap energy of 1.78 eV. In that way, an increase of the QY can be easily monitored and can start from 2 $h\nu/E_{gap}$, which is indeed what we observe. Here, a direct determination of the CM efficiency (η_{CM}) can be made, following the model proposed in Ref. [101]:

$$\mathrm{CM\ QY} = \Big(\frac{h\nu}{\mathrm{E}_{gap}} - 1\Big)\eta_{\mathrm{CM}} \tag{2.5}$$

where $h\nu$ is the incident pump photon energy. The characteristic step-like feature with its threshold energy at 2 E_{gap} is obtained for η_{CM} = 1. Subsequently, as the conversion efficiency decreases, the sharp onset broadens as is indicated by the dotted lines. Here, we obtain a high CM conversion efficiency η_{CM} of $\sim$98% and $\sim$97%, as deduced from the dynamics around the PIB as well as the PIA maxima.

2.7 Photo-bleach rise time

Now we consider the rise time of the PIB transients as a function of excitation energy, which evidences the build-up of the free carrier population (figure 2.5c). Here, an increase appears, even more so when the CM threshold identified from our above discussed measurements is reached i.e. $E_{exc} \geq 2\ E_{gap}$. This delay in rise time is clearly longer than the experimental temporal resolution of the setup ($\leq$150 fs). It can be observed for the PIB as well as the PIA (not shown here), on a similar time scale. Its characteristic time constant is estimated as 1 - 3 ps, depending on the pump energy, in agreement with Ref. [95] One could argue that the increase of the PIB signal build-up at higher excitation energies, could alternatively be explained by the larger excess energy of the photoexcited carriers and, consequently, the longer relaxation time necessary to reach the band edge states probed by the PIB. [102] However, such a possibility is at variance with (i) the observation that the effect is also visible for PIA, which probes all the carriers in the band, and (ii) the rapid increase of the signal rise, for excitation above the CM threshold. We therefore - tentatively - attribute this additional e-h pair generation time to the CM process.

This experimental result provides a unique insight into the physical mechanism of the CM process. While CM has been investigated and modeled theoretically for some time now, no generally accepted model of its physical mechanism exists. In particular, very little is known on the material parameters governing the efficiency and threshold of CM - the most important feature determining the possible impact that CM could have for practical applications. The current observation provides here two important clues: (i) the CM process is not instantaneous: the additional carriers appear clearly after those generated primarily upon photon absorption; and (ii) CM seemingly does not affect the initial increase of the PIB signal (the first 150 fs), which depending on the pump energy, is determined by a combination of carrier generation upon photon absorption and their cooling to

the probed state. [102] The latter is especially insightful: since the experimentally observed cooling time is determined only by relaxation between the lowest states in bands, this implies that (i) the hot carrier losing its energy is not directly transferred to the lowest state, and (ii) the secondary carrier, created by CM, arrives in a state with a considerably longer relaxation time. We recall that such states (in the form of self-trapped excitons) have been investigated in the past for Si NCs [103–105] and have recently been invoked also for IP-NCs. [106]

2.8 Comparison with previous investigations

Finally, we briefly address the possible origin of the different outcome of this study in comparison with the previous investigation. [89] In our opinion, this could be related to small differences in the material preparation. The synthesis of IP-NCs has been reported only in 2015 [5] and while the protocol is not very complicated, a quick literature scan readily reveals that properties of materials prepared by different groups are not identical. In the present case, one specific difference could be the local stoichiometry, especially close to the surface, and a possible formation of insulating inclusions, featuring strong absorption bands in the 3.5 - 4 eV range. This in analogy to the recently identified $CsPbBr_3$/Cs_4PbBr_6 hybrids. [107] One could speculate that strong absorption at energies close to twice the band gap could promote CM. [43] One other important difference of the present study is the application of PIA/PIB rather than ultrafast PL spectroscopy, as used in Ref. [89]. It cannot be excluded that both techniques could probe in different populations of carriers, with PL reflecting exclusively a population of the emitting state.

2.9 Conclusions

In conclusion, we demonstrate efficient CM in $CsPbI_3$ NCs from the transient PIB and PIA dynamics in TA spectroscopy, using a variety of experimental strategies. The occurrence of CM is identified through the observation of an additional fast component in the transient dynamics, recorded for above-threshold pumping, maintaining the experimental conditions at $<N_{exc}> << 1$. CM is further confirmed from the photo-excitation energy dependence of carrier generation yield as a function of pump fluence. CM commences just after the energy conserving threshold of $E_{exc} \geq 2E_{gap}$ of the large NC fraction ($d_{NC} \sim$12 nm with E_{gap} = 1.77 eV) and features a CM QY up to 98%. In addition, coincident with the CM process a longer picosecond build-up of the free carrier concentration for high-energy pumping is observed.

3

Direct observation of band structure modifications in $CsPbBr_3$ nanocrystals

In this Chapter, the variation of the band gap energy of single $CsPbBr_3$ NCs, as a function of size and shape, and upon embedding within an ensemble is investigated, using EELS. In the experiment, the EEL spectrum is directly mapped onto an individual NC, whose dimensions and location are simultaneously measured to the highest precision. In that way, we establish an intimate relation between the NC size and even shape, and its band gap energy on a single object level. We explicitly follow the band gap increase in smaller NCs due to QC and demonstrate that it is predominantly governed by the smallest of the three edges of the cuboidal perovskite NC. Also, the presence of an effective coupling between proximal NCs in an ensemble, leading to their band structure modification is demonstrated. These unique insights are directly relevant to the development of custom-designed quantum structures and solids which will be realized by purposeful assemblage of individually characterized and selected NCs, serving as building blocks.

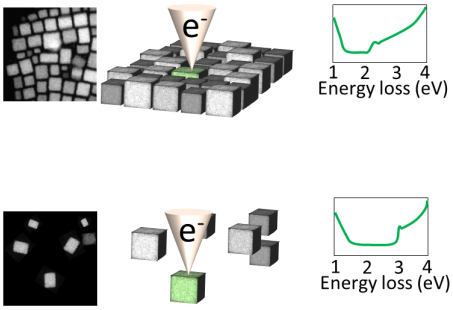

3.1 Introduction

In general, the characterization of nanomaterials is usually conducted on an ensemble of nanoparticles. However, it can be very insightful to do that on a single NC level and also to study the interaction between individual NCs. The correlation between the NC size and the band gap energy is commonly obtained by two separate experiments performed on NC ensembles. For instance, (high-resolution) TEM or dynamic light scattering (DLS) determines the NC size distribution within the ensemble, while optical spectroscopy techniques are used to measure the band gap. Since the properties of NCs in an ensemble are not typically different from those of single NCs, [108] accurate correlation is highly challenging. Although PL spectroscopy measurements on single NCs is readily possible, it can only be carried out upon extreme dilution and even then the absorption has to be determined using an additional experiment. [109] In any case, it is fundamentally restricted by the diffraction limit, as the wavelength of the photon source used to excite a NC is significantly larger than its dimensions. Hence, obtaining information on the structural geometry simultaneously with its optical characteristics for a single NC is challenging and the behavior of excitons in a single NC, that may be subject to the influence of its neighbors, remains elusive.

Replacing the optical excitation source with electrons has been shown as a feasible solution, since the low-loss EELS signal arising from the low-energy excitations i.e. valence electron excitations, is in complete analogy with optical absorption spectroscopy. [110] As such, it provides the possibility to investigate the optical properties on nanometer-sized objects in parallel with their structural parameters. In the past, monochromatic EELS has been used to study CdSe NCs, but the resolution, both in real space and energy-wise, were insufficient in order to yield true microscopic insights. [111] However, recent developments in the low-energy monochromatic transmission electron microscope with advanced aberration correctors, have enabled the combination of electron microscopy with ultrahigh spatial and energy resolutions. [90–92] Using this technique, we study the effects of QC on single $CsPbBr_3$ NCs that are either isolated or in the ensemble. This provides comprehensive information which is not accessible in an ensemble experiment. Our findings have a general character, being relevant to other nanomaterials as well, providing unique insights into the coupling between NCs.

3.2 Synthesis and microscopic characterization

The $CsPbBr_3$ NCs have been synthesized by a wet-chemical method, following the protocol described in Ref. [5]. For details regarding the used matererials and procedure, see the Appendix. The NCs have a (near) cubic perovskite structure and a very high PL quantum yield of 70-80%. Their size can be tuned by controlling the synthesis temperature and isolated NCs and clusters can be easily created by diluting the sample. They are supported on a graphene substrate for investigation by STEM. Figure 3.1a shows two low magnified Z-contrast ADF images, indicating the presence of single NCs as well as their larger clusters and ensembles. An atomic resolution ADF image of a 6 nm $CsPbBr_3$ NC, is presented in Figure 3.1b. Alternating spots in a periodically quadratic manner can be seen, each with a different brightness. Each spot corresponds to an atomic column consisting of different atoms. The intensity of the Z-contrast image is directly related to the atomic number of

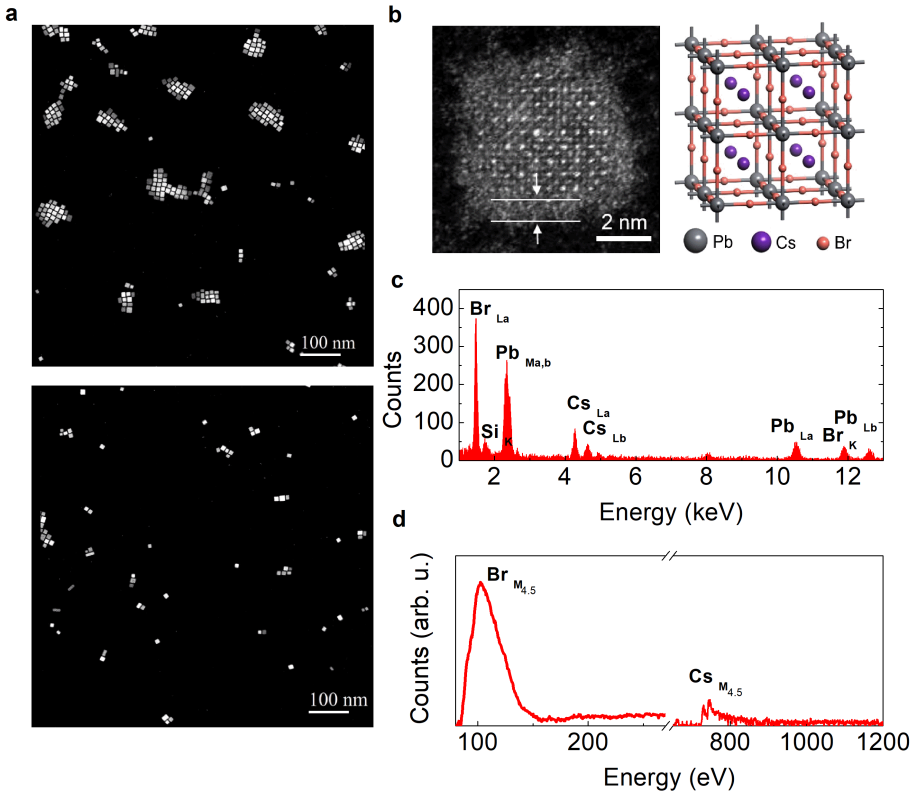

Figure 3.1: Atomic structure and chemical composition of the $CsPbBr_3$ NCs. (a) Low magnified ADF images showing isolated NCs and clusters of NCs that are obtained by diluting the as-prepared sample. (b) Atomic resolution Z-contrast image of an individual cubic $CsPbBr_3$ NC with an edge size of ∼6 nm. The atomic structure model is provided on the right. The white arrows indicate the width of an amorphous layer (∼0.5 nm) surrounding the crystalline core. (c,d) Energy-dispersive X-ray spectrum (c) and core-loss EELS (d) of the same region shown in (b) to determine the elements that are present. The small Si signal in (c) comes from the amorphous part of the substrate.

the imaged species and the number of atoms inside each column, here revealing a cubic structure of $CsPbBr_3$ perovskite projected along the [001] direction. [112] For illustration, a schematic of the perovskite structural model is given to the right. A non-crystalline surface layer (highlighted by the white lines, of ∼5 Å width) around the crystalline core is visible; it is an intrinsic feature of the investigated NCs and is not caused by electron irradiation. This is consistently observed for

all the examined NCs, also for those in an ensemble. This non-crystalline layer can arise due to strain on the surface driven by the high surface energy, or due to the chemical bonding with surface ligands. [113] Figures 3.1c and d show the simultaneously acquired EDS and core-loss EELS of the same NC as shown in Fig. 3.1b, confirming the chemical composition of the NC core, without the presence of any other impurities. The atomic ratio of Cs and Pb is close to 1:1, as determined from the quantification of the EDS on the L-lines of the two elements, again consistent with the $CsPbBr_3$ perovskite composition.

3.3 EELS on single $CsPbBr_3$ NCs

To investigate the correlation between the absorption and the dimensions of a single NC, we performed a systematic study on many individual NCs with different sizes that are either isolated or located within an ensemble. Figures 3.2a and b show ADF images of NCs, isolated and in an ensemble for EELS collection, respectively. For both environments, typical low-loss EEL spectra of NCs with sizes of approximately 6 and 8 nm are depicted in Figure 3.2c. The characteristic onset arising from the band-to-band excitation (as explained in Chapter 2) is easily identified, and enables the unambiguous (single) NC band gap energy determination. As expected, the band gap energy increases with decreasing size, both for isolated and ensemble embedded NCs. Moreover, a clear difference in the step-like absorption onset, and hence the band gap energy, can be seen for an isolated and ensemble embedded NC of similar size, suggesting a NC-NC interaction which influences their energy structure and therefore absorption.

The size dependence of the band gap energy for single and ensemble-embedded NCs, are compared in figure 3.3. The band gap energies of isolated NCs (red circles) and single NCs in an ensemble (blue triangles) have been determined for edge sizes in the range of 5-15 nm. Here, since the boundary between the amorphous and crystalline structure is not sharp, we measured the size of the NCs from the crystalline core, taking the width of the amorphous layer as the uncertainty of the size determination. Surprisingly, we find that small isolated NCs appear to have a higher band gap energy as compared to a NC of the same size in an ensemble. And reversely, a large NC apparently has a lower band gap energy if isolated than when in an ensemble. This result shows that two adjacent NC do not simply ”merge” upon interaction into a single large one, but rather ”average” their band gaps. Statistically, large NCs that are situated in an ensemble are most likely surrounded by equally sized or smaller NCs whereas small NCs are surrounded by larger ones. These somewhat surprising results provide direct evidence of effective coupling between proximal NCs where their band gap and therefore energy structure, is influenced by the neighbors. Similar band structure modification due to NC interaction, such as band gap reduction in InAs NC ensemble, has been reported previously. [114] The band gap ”averaging” effect observed in our experiment indicates the ”collective” dielectric response of the NCs ensemble, presumably through the surface ligands/substrate which couple the NCs in the ensemble. It is important to note, however, that the observation of a clear step at the band gap energy excludes a possibility that the observed NC band gap modification could arise due to small delocalization of the probing electron beam, typical for EELS.

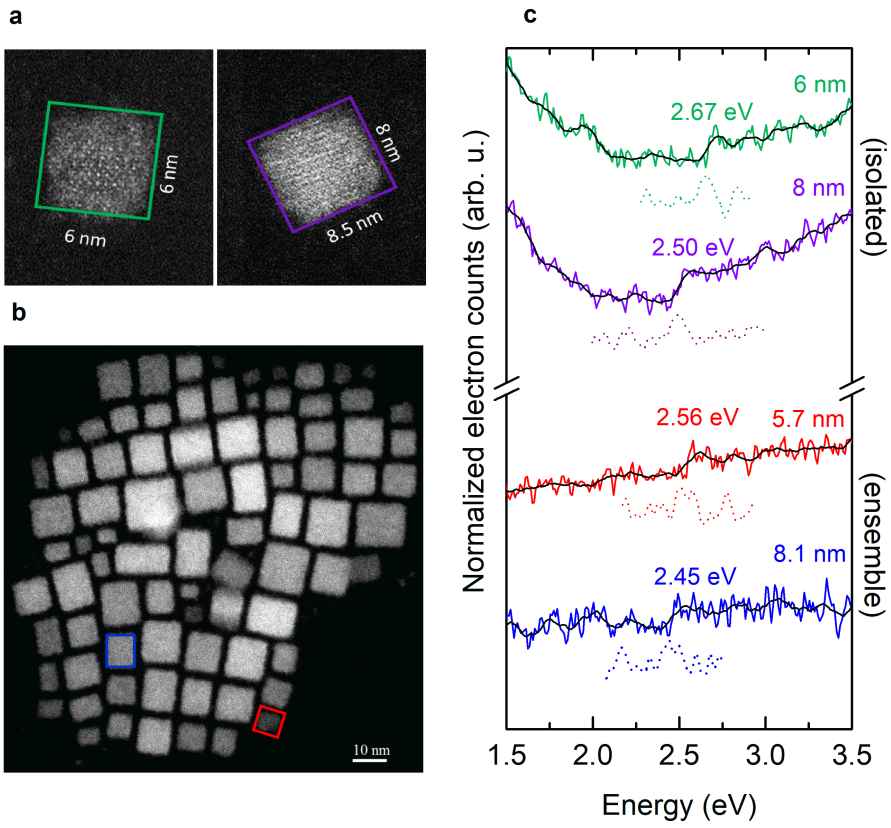

Figure 3.2: Band gap energy of individual near-cubic $CsPbBr_3$ NCs. (a) ADF images showing isolated near-cubic NCs with a size of 6 nm (green) and 8 nm (purple) respectively. (b) ADF image of an ensemble where two NCs with similar sizes as in (a) are indicated (red, blue). (c) The corresponding low-loss EEL spectra of the isolated (top) and in ensemble (bottom) NCs as shown in (a,b). The semi-transparent black solid lines superimposed on the spectra have been obtained by smoothing. The band gap energy is determined from the peak of the first derivative of the spectra appearing at the abrupt onset of absorption, as illustrated by the dashed lines under the spectra for all four NCs. The decaying background in the top two curves, arises from the tail of the ZLP.

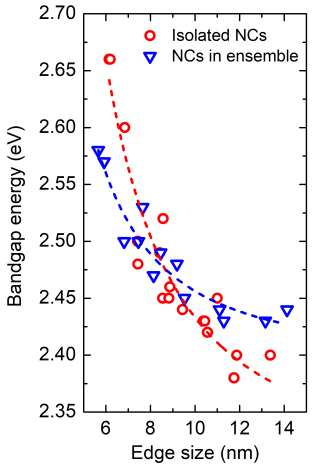

Figure 3.3: Direct comparison of the band gap energy of single $CsPbBr_3$ NCs without (red circles) and with (blue triangles) neighbors. Small isolated NCs appear to have higher band gap energy as compared to a NC in an ensemble with the same size. And reversely, a large NC has lower band gap energy if isolated than present in an ensemble. This indicates that their energy structure is adjusted according to surrounding objects due to an effective coupling between them.

3.4 Different nanoshapes

The characteristics discussed this far are derived from measurements on (nearly) cubic NCs and provide no information on the shape-dependent profile of the band gap energy. In Z-contrast ADF images, the height or thickness of a NC is also proportional to the image intensity (or contrast profile). [115] A brighter intensity indicates larger NC sizes (in the z-direction). As the ADF images provide the surface dimensions (x- and y-direction), the thickness can be qualitatively extracted by integrating the ADF signal along the NC. The dependence of the band gap energy on the shape of a NC can be resolved, as we occasionally found some NCs with a shape other than cubic, as can be seen in figure 3.4a. The three NCs, from left to right, can be considered as a cube, plate, and rod; their corresponding normalized ADF image intensities are given in the panel below. We conclude that the plate- and rod-like NCs differ in thickness with a factor of three and two respectively, as compared to the cubic NC. Figure 3.4b shows their corresponding low-loss EEL spectra. Although the plate- and rod-shaped NCs clearly have a different volume, we observe similar band gap energy. The dependence of the band gap energy on the NC shape is qualitatively shown in figure 3.4c. The red solid dots indicate the band gap energy dependence on the size, for isolated (or individual) cubic NCs. The data has been fitted using the effective mass approximation theory. The green and blue solid dots represent the average edge size as obtained from the ADF image (where only two edges can be distinguished, and are averaged) for the plate- and rod-shaped NCs, respectively. There is a clear discrepancy for the plate and rod with respect to the fit, as the size appears to be too large. However, if the thickness is taken into account, and when we correlate the shortest edge with the band gap energy, the data agrees well with the results of the cubes (open squares). This profoundly indicates that the band gap energy of a NC is determined by its shortest dimension rather than the volume, which also suggests the anisotropic properties of the excitons under confinement. This is further demonstrated in 3.4d, where a nanocube and a nanowire with nearly equal thickness ($\sim$10 nm) are compared. Their EEL spectra reveal nearly equal band gap energies, even though the

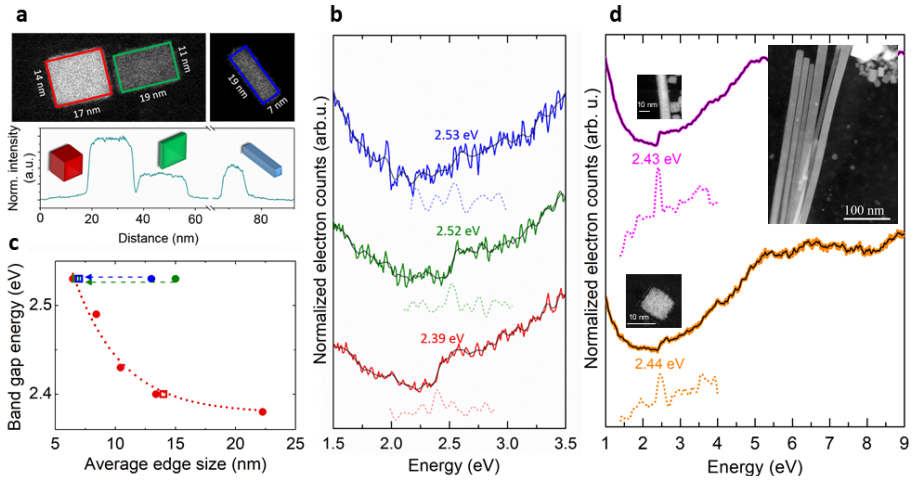

Figure 3.4: STEM and EELS for different nanoshapes of $CsPbBr_3$. (a) ADF images of a nanocube (red), nanoplatelet (green) and a nanorod (blue). The corresponding normalized ADF image intensity is shown in the panel below, from which the nanoparticle thickness is deduced. (b) The corresponding EEL spectra revealing the band gap energy for each nanoparticle. (c) The relation between the band gap energy and average edge size. This is readily established for the nanocubes (red dots), with three identical edges. However, taking into account the two distinguishable dimensions from the ADF image alone, a large discrepancy is observed with respect to the established relation (blue and green solid dots), but not if only the thickness is considered (blue and green squares). From this it is evident that the smallest dimension of a nanoparticle determines its band gap energy and therefore if it is subject to QC. (d) Comparison between a nanocube and a nanowire. Their EEL spectra show that in spite of their different geometry, their band gap energy is almost equal, due to their similar thickness of $\sim$10 nm. The inset (d) shows an ADF image of a nanowire custer showing they can grow up to hundreds of nanometers in size.

nanowire length clearly exceeds the size of the nanocube. The inset of figure 3.4d illustrates that formed nanowires can grow up to several hundreds of nanometers in length.

3.5 Conclusions

Taking advantage of the recent advances in the aberration-corrected monochromatic EELS technique, we were able to determine absorption spectra of single cubic $CsPbBr_3$ perovskite NCs, whose individual dimensions were measured simultaneously. In that way, an intimate correlation between the band gap energy and size and shape of a $CsPbBr_3$ NC has been obtained. We have also demonstrated how properties of individual NCs change due to their mutual interactions in an ensemble, thus paving the way towards purposeful development of larger quantum structures and quantum dot solids with a-la-carte properties.

4

Hybridization of single nanocrystals of Cs_4PbBr_6 and $CsPbBr_3$

While colloidal ensembles of $CsPbBr_3$ NCs can be conveniently prepared by chemical synthesis, it can also yield NCs of Cs_4PbBr_6 and the properties of the two are easily confused. In this Chapter, we investigate in detail the optical characteristics of simultaneously synthesized green-emitting $CsPbBr_3$ and insulating Cs_4PbBr_6 NCs. We demonstrate that the two materials inevitably hybridize forming nanoparticles with a spherical shape. The actual amount of Cs_4PbBr_6 NCs and nanohybrids increases for synthesis at lower temperatures, i.e. the condition typically used for development of perovskite $CsPbBr_3$ NCs with smaller sizes. We use state-of-the-art EELS to study single nanoparticle properties and, combined with structural modeling, we conclusively identify the nanospheres as $CsPbBr_3$/Cs_4PbBr_6 hybrids. We show that the two phases are independent of each other's presence and merge symbiotically. Herein, the optical characteristics of the parent materials are preserved, allowing for an increased absorption in the UV due to Cs_4PbBr_6, accompanied by the distinctive efficient green emission resulting from $CsPbBr_3$.

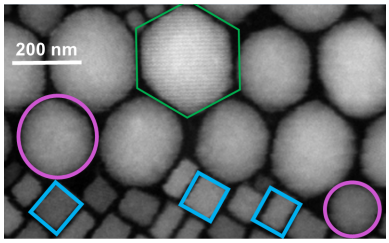

4.1 Introduction

As we have seen in Chapter 3, different IP nanoshapes can form during the synthesis procedure. However, the IP-NCs can also be deliberately synthesized in other shapes than cubes, by making some small modifications of the initial protocol, [5] such as changing the reaction temperature and time, and the ligands length. [116] IP nanorods or nanowires can be obtained by increasing the reaction time, the use of shorter ligand chains and the additions of hydrohalic acids to the solution [117–119] are other possible approaches to be considered. When using solvents of different polarity, the morphologies evolve from NCs to nanoplatelets and further to nanobars; [120] nanoplatelets can also be synthesized by decreasing the reaction temperature. [38] Nanoplatelets have been grown adding acetone to the reaction, [121] and micrometer nanosheets are formed upon mixing short and long ligands. [122]

It is also generally known that preparing pure $CsPbBr_3$, in bulk, thin films, single crystals or nanostructures, is challenging. The phase diagram of the stable CsX-PbX_2 (X=Br, Cl) system shows the existence of two complex ternary compounds, the congruent melting (i.e. maintaining the same atomic composition) compound $CsPbX_3$ and incongruent Cs_4PbX_6. [123] When preparing the $CsPbBr_3$ (from $PbBr_2$), the Cs_4PbBr_6 compound is expected to form as well if there is an excess of Cs, resulting in the CsBr:$PbBr_2$ ratio being no longer exactly 1:1. And reversely, when growing Cs_4PbBr_6 crystals, it is difficult to prevent the formation of $CsPbBr_3$ due to an unavoidable incongruent melting crystal growth process. [124, 125]

Also in the case of IP-NCs, their synthesis is intended to yield pure perovskite nanostructures, but the selectivity of the reaction is not always 100%. Other nanoparticles are obtained within the same reaction, where a common associate outcome is - indeed - the formation of Cs_4PbX_6 NCs, which appear hexagonal. On the other hand, these nanoparticles can also be produced selectively, by adding an excess of Cs^+ to the IP-NCs synthesis protocol. [126] The Cs_4PbBr_6 NCs can be converted into $CsPbBr_3$ NCs while maintaining their size, through addition of $PbBr_2$ [126] or by CsBr extraction. [127] Despite these pronounced differences in composition and crystal structure, there has been quite some confusion in the literature on the emission properties of these two different nanomaterials, with some reports claiming bright green emission from NCs of Cs_4PbBr_6, showing very similar optical properties as $CsPbBr_3$. Our single NC EELS measurements solve this dispute, exclusively demonstrating that there can be no visible emission from pure Cs_4PbBr_6 NCs, which are insulating and have a large band gap energy ($\sim$4 eV). [124–126] As we will see, it is the $CsPbBr_3$-phase in hybridized Cs_4PbBr_6/$CsPbBr_3$ spherical NCs that is responsible for the green emission.

4.2 Synthesis and microscopic characterization

The synthesis (Ref. [5]) was carried out at two different temperatures, 100 °C and 160 °C (see the Appendix for details). It is well-known that the synthesis temperature plays an important role, determining the shape and size of $CsPbX_3$ NCs. For the synthesis at 160 °C we observe mostly cuboid $CsPbBr_3$ NCs with an average size of 8-10 nm, but also some $CsPbBr_3$ nanowires and large nanoplatelets with a high aspect ratio. We measure a PL QY of $\sim$80% for excitation at E_{exc} = 3 eV indicating that the emission efficiency is not greatly affected. Additionally, larger nanoparticles (10

- 20 nm) with a spherical shape, as well as appearing hexagonal, are formed next to the nanocubes (figure 4.1a) in the same sample.

Cs_4PbX_6 has a trigonal crystal structure at room temperature. [123, 128] The Cs^+ chains in Cs_4PbX_6 crystals, projected into the [0 0 1] plane, arrange in a hexagonal orientation. [129] Therefore, in HR-TEM images, the Cs_4PbBr_6 NCs will appear as hexagons (as of now referred to as nanohexagons) whereas the nanocubes are $CsPbBr_3$ NCs. Lowering the synthesis temperature to 100 °C leads to the predominant formation of nanohexagons, while the nanocubes are in minority - Figure 4.1b. This indicates that the production of either nanocubes or nanohexagons is synthesis temperature-controlled and is not governed by the amount of reactants (all other conditions are kept equal). It also demonstrates that the chemical reaction does not completely yield the desired product, which in this case are $CsPbBr_3$ NCs. The co-formation of different shaped $CsPbBr_3$ nanoparticles and Cs_4PbBr_6 NCs has been observed for any sample produced in the temperature range between 100 - 200 °C.

To confirm the elemental composition of the nanostructures in both samples, EDS is performed. Figure 4.1c shows the corresponding spectra, where mostly Cs, Pb and Br are detected. The Au peak originates from the TEM grid. The ratio between Cs and Pb is determined at 4:1 for the 100 °C sample, corresponding to Cs_4PbBr_6. For the 160 °C sample this is 1.2:1 (where one would expect 1:1) indicating the presence of excess Cs, which is due to Cs_4PbBr_6 NCs that were formed instead of $CsPbBr_3$ NCs. The coexistence of both compounds has been reported before, in bulk and thin films as well as in nanometer sized aggregates dispersed in a crystal lattice. [124, 130] To confirm that they coexist in the sample synthesized at 100 °C, X-ray diffraction (XRD) was performed. The corresponding XRD pattern is shown in figure 4.1d, with the peaks associated to Cs_4PbBr_6 and $CsPbBr_3$ denoted by a and b, respectively, indicating the presence of both phases. An additional broad peak is observed at 20° which arises due to the background noise appearing for a thin sample layer. This is demonstrated by the top red curve, which corresponds to the same measurement performed on a thinner sample.

4.3 Identifying a pure Cs_4PbBr_6 nanohexagon

A detailed structural analysis is performed on a Cs_4PbBr_6 NC, to identify its crystal symmetry. By taking a Fast Fourier Transform (FFT) of a selected region in an atomic resolution image, the lattice periodicity, i.e. the diffractogram, of a crystalline structure is revealed. Figure 4.2a shows an atomic resolution STEM image of a single Cs_4PbBr_6 NC. The lattice periodicity can be clearly seen. Although the individual atoms are not resolved due to the slight deviation from its zone axis, the lattice information can still be identified from the diffraction pattern (figures 4.2b and c). Two diffraction spots are indicated which are identified as the [-4 1 1] and [-2 1 0] planes with an intersection angle of 19.5°, corresponding to a lattice distance of 3.33 Å and 7.06 Å, respectively. Using the experimentally obtained zone axis, the modeled atomic arrangement (figure 4.2d) is shown to agree well with the experimental data: the rows of Cs atoms can be clearly seen in figure 4.2a, identifying a pure Cs_4PbBr_6 NC.

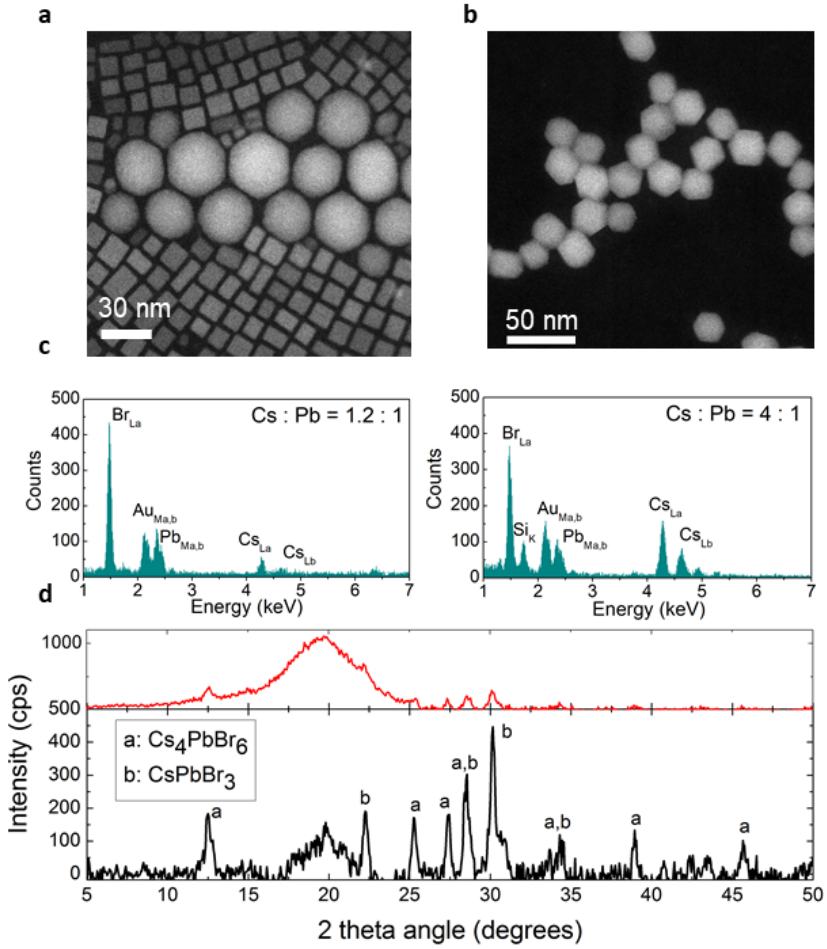

Figure 4.1: Cs_4PbBr_6 and $CsPbBr_3$ NCs and their chemical and structural characterization. (a,b) ADF images of the samples prepared at 160 °C (a) and 100 °C (b). (c) EDS spectra of the samples from (a) and (b). (d) X-ray diffraction pattern of the sample prepared at 100 °C, drop-casted on a quartz substrate. The peaks related to the Cs_4PbBr_6 and $CsPbBr_3$ structures are denoted as "a" and "b" respectively. The broad peak around 20° is due to background noise, which is only amplified as the sample layer becomes thinner, as represented by the exemplary spectrum shown on top (red curve).

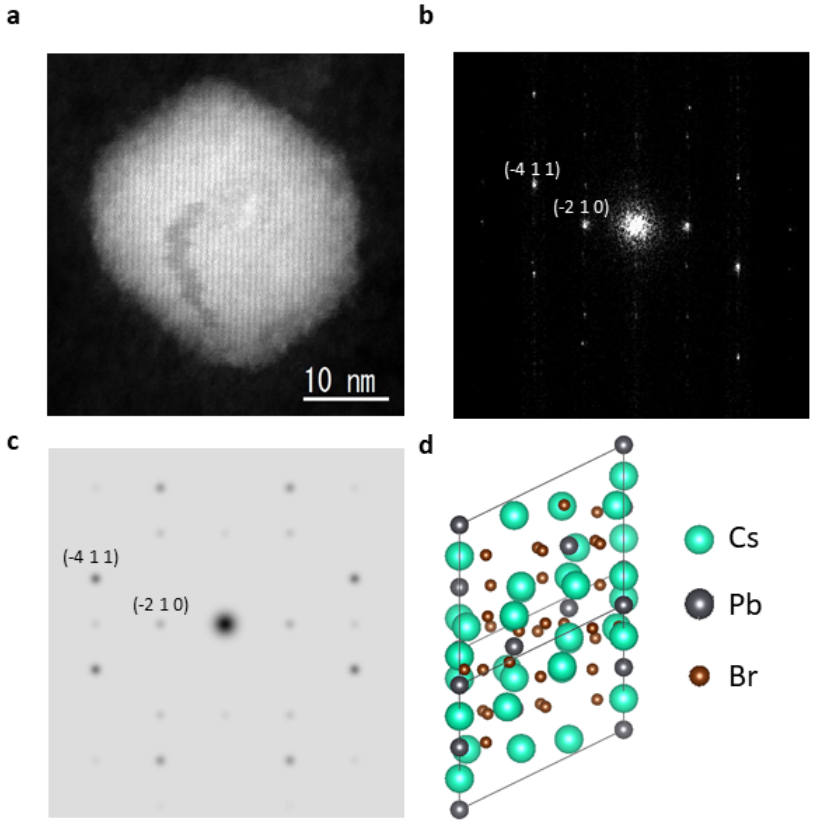

Figure 4.2: Identification of a pure Cs_4PbBr_6 NC. (a) Atomic resolution STEM image of a nanohexagon. (b,c) Diffraction pattern of (a) obtained by taking a Fast Fourier Transform of the shown region. Two diffraction spots in this zone axis are identified to be the [-4 1 1] and [-2 1 0] planes, with an intersection angle of 19.5°, which corresponds to a lattice distance of 3.33 Å and 7.06 Å, respectively. (d) Modeled atomic arrangement using the experimentally determined zone axis, which agrees with the Cs_4PbBr_6 structure.

4.4 EELS on single Cs_4PbBr_6 and $CsPbBr_3$ NCs

To distinguish between the Cs_4PbBr_6 and $CsPbBr_3$ phases and their different electronic structure, single NCs of both compounds are investigated by low-loss EELS. Figure 4.3a shows the EEL spectra for the probed nanoparticles (solid lines) with the first derivative shown underneath (dotted lines) and its maximum which determines the band gap energy. We find a value of 2.45 eV for the $CsPbBr_3$ nanocube (red). In contrast, for the Cs_4PbBr_6 NC, no characteristic step is revealed. This

is expected since Cs_4PbBr_6 is an insulator with a large and indirect band gap, hence the lack of an excitonic feature. Two distinctive absorption peaks at 4 and 5.5 eV are observed which are absent for the nanocube. More interesting is the nanosphere, for which its EEL spectrum shows characteristics of both phases: an excitonic line as well as the two absorption bands in the UV (figure 4.3b, green spectrum). Upon analysis of its crystal symmetry and structure, we confirm that the nanosphere is formed by hybridization of the Cs_4PbBr_6 and $CsPbBr_3$ phase. This is further demonstrated by combining the experimentally obtained EEL spectra of the nanocube and the nanohexagon, hence obtaining a simulated spectrum (orange trace in figure 4.3b) which is similar to the experimentally measured one. The preservation of the onset in the band structure and the characteristic absorption peaks in the UV indicate phase segregation inside a single NC i.e., the two phases are independent of each others presence but grow together into a single NC. This means that the spherical NCs represent indeed an intermediate state between the Cs_4PbBr_6 and $CsPbBr_3$ phases.

4.5 Optical characteristics

The identified band structures of the investigated single nanoparticles are compared with the optical characteristics of an ensemble. Figure 4.4 shows the PL (solid lines) and normalized absorption (dotted lines) spectra of the samples synthesized at 100 °C (top) and 160 °C (bottom), excited at E_{exc} = 2.88 eV. The narrow PL bands centered around 2.43 eV and 2.53 eV for the two investigated (as prepared) samples agree with $CsPbBr_3$ NC emission, consistent with larger and smaller NC sizes for higher and lower synthesis temperatures, respectively. An additional PL peak at 2.4 eV is observed for sample synthesized at 100 °C, when diluted. This arises from disintegration and clustering of the NCs, as ligands are removed upon dilution due to their dynamic bonding on the NCs surface, [113] which causes the PL to redshift towards the $CsPbBr_3$ bulk value (2.33 eV). We do not observe emission from the Cs_4PbBr_6 NCs in the range from 3 - 4 eV which was recorded for E_{exc} = 4.13 eV (above the absorption band of Cs_4PbBr_6). In fact, we observe no significant change in the PL spectra when excited at 2.88 eV and 4.13 eV as they are almost identical. Therefore, we conclude that the visible emission at 2.4 - 2.55 eV originates solely from the $CsPbBr_3$ phase. We do observe a small redshift with decreasing excitation energy, which is explained by reabsorption and/or a residual energy transfer upon selective excitation of the NC ensemble, as a transfer always proceeds from small to large NCs. [131] All the PL bands ranging between 2.4 - 2.55 eV, show a small Stokes shift from their corresponding absorption spectra that exhibit a clear excitonic peak at the respective onset, as is typically observed for $CsPbBr_3$ NCs. In addition, a distinct absorption peak at $\sim$3.8 eV is observed for the sample containing mostly Cs_4PbBr_6 NCs, in agreement with our result from EELS and with those reported for Cs_4PbBr_6 NCs, large single crystals and thin films. [124–126, 132]

4.6 Discussion

Despite these pronounced differences in composition and crystal structure, there has been quite some confusion in the literature on the emission properties of these two different nanomaterials, with some reports claiming bright green emission from nanohexagons of Cs_4PbBr_6, showing very similar

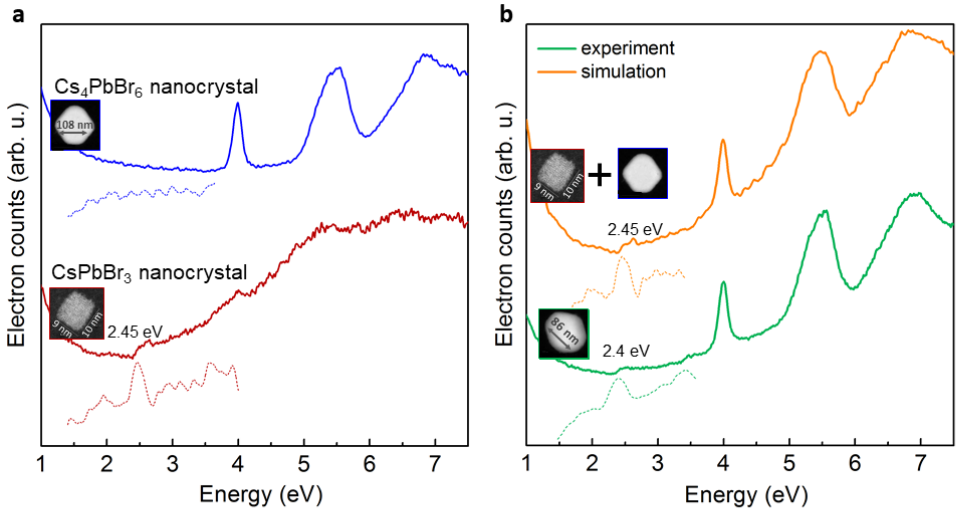

Figure 4.3: Energy band gap and structure. (a) Valence-loss EEL spectra representing the absorption of a $CsPbBr_3$ nanocube (red) and a Cs_4PbBr_6 NC (blue), appearing in the same sample (160 °C). The band gap energy of the nanocube (2.45 eV) is determined from the peak of the first derivative of the EEL spectrum, that appears due to the abrupt onset in absorption (indicated by the dotted lines). No such onset is observed for the Cs_4PbBr_6 NC, which is an insulator with a large band gap energy of 4 eV. (b) Valence-loss EEL spectrum of a spherical NC (green) observed in the same sample, formed upon hybridization of a nanocube and a nanohexagon. The hybrid has, as expected, a band gap energy similar to that of the nanocube. The orange spectrum represents the simulated EEL spectrum, obtained from adding the experimentally measured spectra of a nanohexagon and a nanocube, as shown in (a).

optical properties as $CsPbBr_3$. Since the spherical NCs in our STEM measurements often appear as slightly cubic and/or as hexagons with rounded corners, their optical ensemble characteristics could be erroneously attributed to (pure) $CsPbBr_3$ or Cs_4PbBr_6 NCs. Recent studies on the synthesis of single crystals, assign the ∼520 nm (2.38 eV) and the ∼550 nm (2.25 eV) emission bands to Cs_4PbBr_6 and $CsPbBr_3$ respectively, [133, 134]. Though it is also reported that confined $CsPbBr_3$ quantum dots could contribute. [135, 136] On the other hand, M. Nikl *et al*. [124] also studied the emission characteristics of Cs_4PbBr_6 crystals and thin films, and show absorption features at 520 nm and the same green emission around 545 nm, attributing it to the $CsPbBr_3$-like phase being present in the bulk Cs_4PbBr_6 sample. The optical properties of both $CsPbX_3$ and Cs_4PbX_6 crystals are often explained as being related to transitions between states of the Pb^{2+} ions (which form regular octahedra that define the perovskite structure). Cs_4PbBr_6 itself is said to have absorption peaks

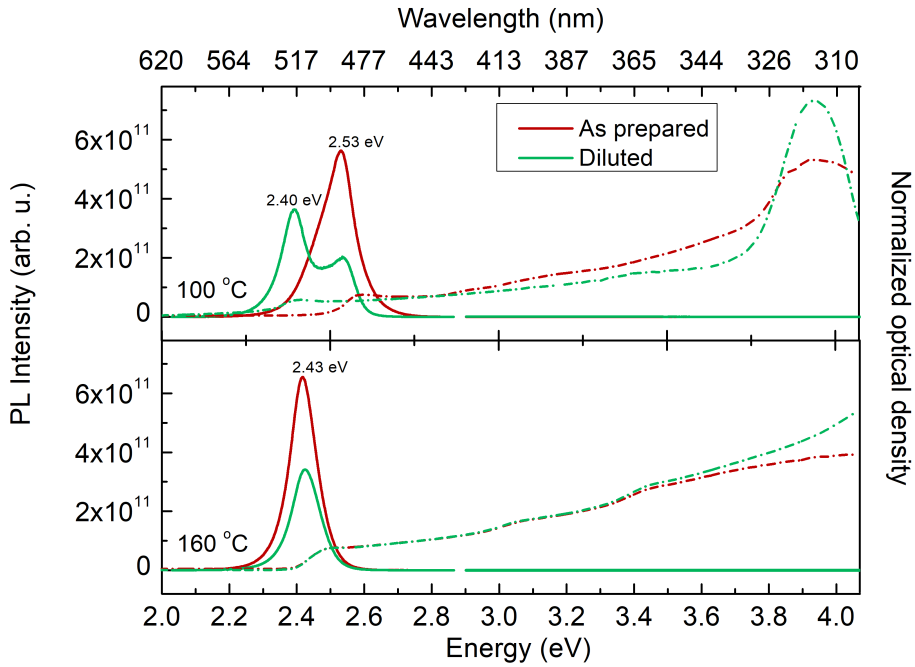

Figure 4.4: PL (solid lines) and absorption (dotted lines) spectra of the samples synthesized at 100 °C (top panel) and 160 °C (bottom panel) with different concentrations, excited at E_{exc} = 2.88 eV. The PL peaks at 2.45 eV and 2.53 eV correspond to $CsPbBr_3$ NC emission, for small and large NC sizes respectively, which agree with the high and lower synthesis temperature. For the (diluted) samples synthesized at 100 °C, an additional PL peak around 2.4 eV is observed, which appears after disintegration and clustering of the $CsPbBr_3$ NCs due to removal of the ligands upon dilution, causing the PL to redshift towards the $CsPbBr_3$ bulk value. For the 100 °C sample, a clear absorption peak is observed around 3.8 eV. No emission from the Cs_4PbBr_6 NCs is observed in the UV region around 3 - 4 eV (for E_{exc} = 4.13 eV).

at 220 nm (5.6 eV) and 310 nm (4 eV). These observations, specifically with respect to the green emission, are to some extent in contrast with each other. Preparing pure Cs_4PbBr_6 or $CsPbBr_3$ NCs in ensembles proves challenging, as the co-formation of the two phases (i) requires extra-care during synthesis, and (ii) can easily escape detection due to the large band gap of Cs_4PbBr_6. Hence, ensemble characterization cannot fully distinguish between their optical and at the same time structural properties.

A clear distinction, on the other hand, is fully accomplished by single particle EELS. We observe that the energy structure of a single pure Cs_4PbBr_6 NC has large band gap, featuring no absorption in the visible/near UV region ($\sim$2 - 3.5 eV). This excludes the possibility of emission in that energy range, conclusively solving this dispute. Distinct absorption bands are observed at 4 and 5.5 eV

- in full agreement with the work of M. Nikl *et al*. It is the $CsPbBr_3$-phase within the hybridized Cs_4PbBr_6/$CsPbBr_3$ spherical NCs that is responsible for the visible PL, as an excitonic feature is clearly identified in its EEL spectrum. Furthermore, even if the ensemble is excited below the 4 eV band gap of Cs_4PbBr_6, the green emission is still observed. Already an impurity of just 2% of the semiconductor $CsPbBr_3$ in the insulator Cs_4PbBr_6 yields strong PL in the visible. [126] The fact that these two phases can apparently easily co-exist, can also be advantageous. Because the insulator Cs_4PbBr_6 is air-stable and robust, it has previously served as a protective matrix for $CsPbBr_3$ NCs, forming an optically active and high-performance $CsPbBr_3$@Cs_4PbBr_6 composite. [137, 138]

4.7 Conclusion

We have analyzed a single pure Cs_4PbBr_6 NC and demonstrated that it can only absorb in the UV. We have identified and characterized $CsPbBr_3$/Cs_4PbBr_6 hybridized spherical NCs which preserve the optical characteristics of both parent materials: they show a strong green emission at 2.45 eV as well as 4 and 5.5 eV absorption bands in the UV, which are resulting from the $CsPbBr_3$ and Cs_4PbBr_6 phases, respectively. In particular, our method demonstrates the advantage of particle-by-particle EELS analysis over macroscopic optical ensemble measurements, which is critical if a specimen features a composition of different nanoparticles. The nanospheres together with $CsPbBr_3$ nanocubes and Cs_4PbBr_6 nanohexagons are appearing simultaneously during the commonly used colloidal synthesis of all-inorganic perovskite NCs. Lowering the synthesis temperature steers the reaction towards the formation of mostly Cs_4PbBr_6 NCs.

5

Extraordinary interfacial stitching between single $CsPbBr_3$ perovskite nanocrystals

In this Chapter, spontaneous merging of drop-casted $CsPbBr_3$ NCs is discussed. This process is promoted by humidity and mild temperature treatments while arrested by electron beam irradiation. We investigate the aggregation between individual NCs at the atomic level and show that the merging process preserves the elemental composition and electronic structure of the $CsPbBr_3$ NCs, and takes place between NCs of different sizes and orientations. In particular, we reveal seamless stitching for aligned NCs, similar as reported in the past for graphene flakes. Since the crystallographic alignment occurs naturally in drop-casted layers of $CsPbX_3$ NCs, our findings constitute the essential first step towards the development of large-area nanosheets with band gap energies predesigned by the NC choice - a possible gateway to large-scale photovoltaic applications of inorganic perovskites.

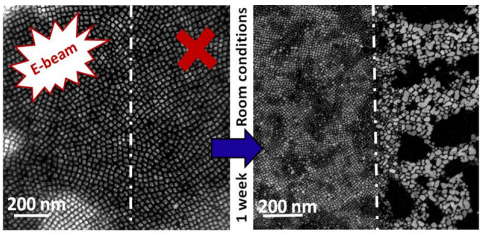

5.1 Introduction

The sintering of single IP-NCs into larger crystals has been previously reported as a consequence of the material instability induced by temperature treatments and/or exposure to polar solvents. [139, 140] However, this IP-NCs degradation feature can be turned into an advantage if individual IP-NCs are treated as building blocks of larger structures. Indeed, due to their (near) cubic shape and narrow size distribution, [5] they are ideally suited to form close-packed layers and structures, being an excellent candidate for the design and development of quantum solids. [141] The solvent polarity and a strictly controlled drying process are important factors for the formation of ordered structures of high quality. For instance, the interaction between the alkyl surface ligands and hexane drives the creation of polymeric nanostrands and subsequent organization of the IP-NCs into 1D chains. [142] $CsPbX_3$ NCs purified in toluene arrange themselves in square geometries when drop-casted, while they can create cubic micrometric lattices under conditions of the controlled evaporation of the solvent and the ligands-solvent ratio. [143, 144] In both configurations, IP-NCs maintain their properties, showing a small PL red-shift due to coupling of neighboring NCs and the change of the overall dielectric constant. [131, 145] Furthermore, it has been reported that the addition of ethanol promotes the aggregation of IP-NCs through surface ligands destabilization. [146]

Besides self-assembly, the fusion of single IP-NCs is a very interesting process to develop high quality thin films. Here, we reveal the spontaneous seamless stitching of drop-casted $CsPbBr_3$ NCs; the merging is promoted by humidity and can be accelerated by mild temperature treatments, whereas it can be arrested by electron beam irradiation. [147] Due to their cubic shape and a narrow size distribution, IP-NCs are ideally suited to form close-packed layers and/or multilayer structures. In addition, we also demonstrate that closely packed proximal IP-NCs merge together forming larger structures and long nanowires.

5.2 Optical and microscopic characteristics

A fresh sample, drop-casted on an amorphous carbon/ graphene grid, is shown in figure 5.1a. The $CsPbBr_3$ NCs, synthesized at 160 °C, have a size distribution of 8.1 ± 1.2 nm. The NCs arrange themselves in ordered square geometries, in some analogy to the honeycomb superlattices of PbSe NCs. [148] Despite being clearly separated by surface ligand layers, neighboring IP-NCs effectively couple modifying each others energy structure. [93] When stored at room conditions, the NCs layer spontaneously aggregates, with individual IP-NCs merging into larger structures (figure 5.1b). Eventually, after a sufficiently long time, a semi-continuous layer of rather poor homogeneity is formed (figure 5.1c). In case of a NC layer of low density, isolated nanoplatelets appear. When the storage time is increased to 6 months (figure 5.1d), the NCs can arrange in very long nanowires (aspect ratios of $\sim$100 and higher) although individual NCs are still visible. To grow a large homogenous film of merged NCs, other parameters (humidity, temperature, etc.) should be considered as we will reveal in this study. We have observed this aggregation process in layers of IP-NCs of different size and chemical composition. It is important to note that upon merging, the chemical composition is maintained (confirmed by EDS), which implies that no chemical reactions are involved and that larger IP nanostructures are created. At the same time, we observe that the merging of individual IP-NCs

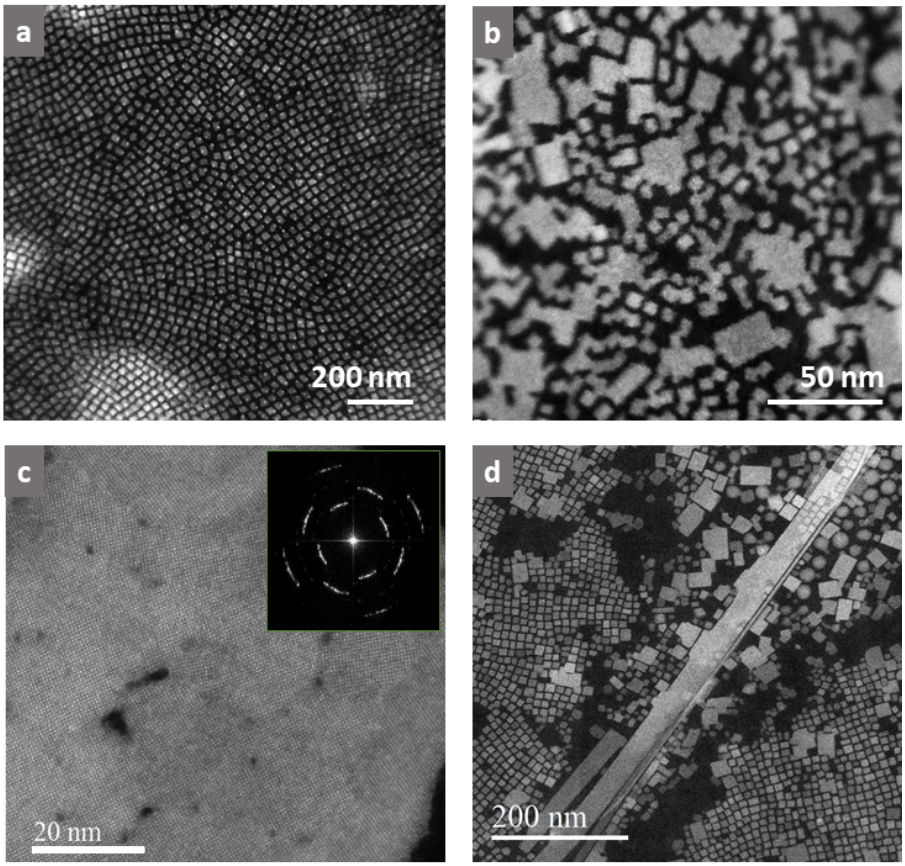

Figure 5.1: ADF-STEM images of drop-casted $CsPbBr_3$ NCs on an amorphous carbon/graphene grid. (a) A fresh drop-casted sample. (b) The same sample after being stored at room conditions for a week. (c) Another region of merged NCs; the inset shows the fast Fourier transformation (FFT) pattern, demonstrating the misorientation from different small domains. (d) Sample stored at room conditions for 6 months.

modifies the optical properties of a layer, red-shifting its PL spectrum and absorption edge (figure 5.2a). We evaluated this effect using a drop-casted layer of $CsPbBr_3$ NCs on a quartz substrate. We studied the merging process through monitoring the PL QY of the drop-casted layer and how it is affected by exposure to light and air. The sample stored for one week in the dark at inert gas atmosphere, exhibited a negligible change in the PL QY, while the sample stored in air while being constantly illuminated showed a major QY decrease, by a factor of 6 (5.2b).

To study the conductivity of the merged layer, we drop-casted IP-NCs on interdigitated elec-

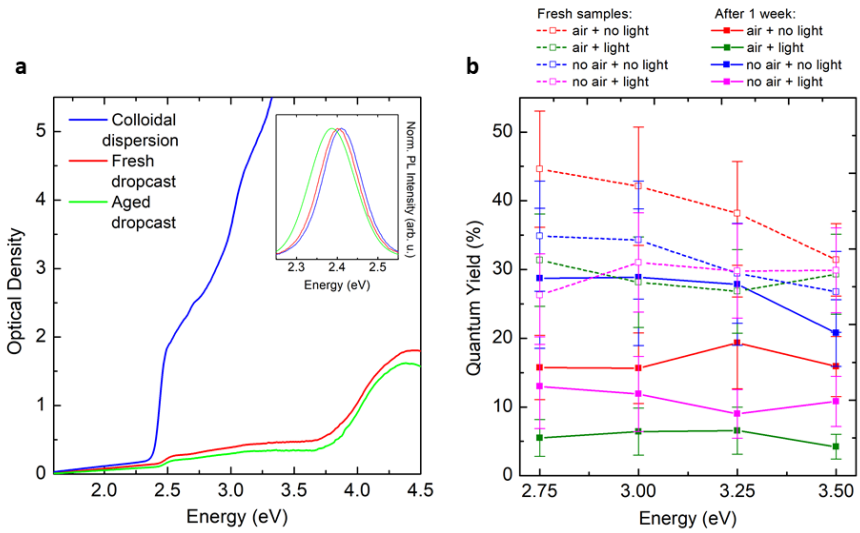

Figure 5.2: (a) Absorption and photoluminescence spectra (inset) of $CsPbBr_3$ NCs in toluene (blue), drop-casted on a quartz substrate (red), and the same sample after being stored at room conditions for 1 week (green). (b) PL QY measured on drop-casted $CsPbBr_3$ samples subjected to different conditions during one week.

trodes (5 m width) and measured current-voltage characteristics after 1 hour, 1 day, and 9 days of storage in air (for the results, see the supporting information in Ref. [147]). We note that while the freshly drop-casted film is conductive, the NCs aggregation increases its resistivity, as the merging of individual IP-NCs into larger clusters leads to the formation of voids, which disrupt the percolative pathways across the 5 μm distance between the electrodes. This problem can be addressed by adding successive layers of NCs to fill in those voids.

5.3 Before and after merging

In order to understand the merging process of IP-NCs in some detail, we performed experiments on a microscopic level. We start the investigation by comparing the EEL spectra of freshly drop-casted (figure 5.3a) and merged (figure 5.3b) IP-NCs. First, the EELS of an ensemble is compared, before vs after merging. As such, the accumulated EELS signal is measured in an area of choice i.e., averaging different points of the layer, and represents the sum of the (averaged) absorption by neighboring NCs. Comparing the two spectra (figure 5.3c), the band gap energy slightly red-shifts ($\sim$60 meV) upon merging (E_{fresh} = 2.45 eV, E_{merged} = 2.39 eV) approaching the bulk value (E_{bulk} = 2.33 eV). [149] We note that the aggregated IP film still exhibits a small QC induced by its nanometer-range thickness.

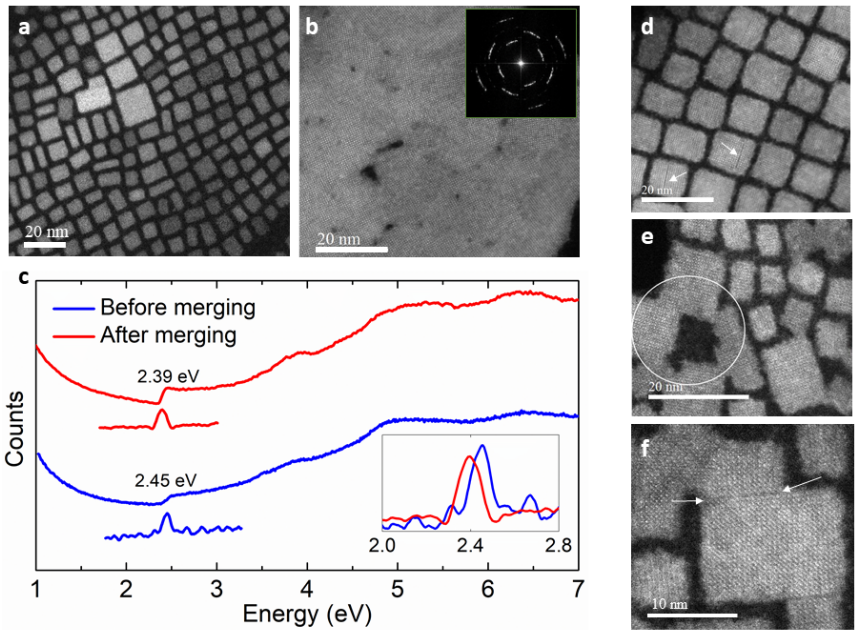

Figure 5.3: Comparison of the absorption of a fresh drop-casted sample and a one-week old region of the film, investigated by EELS. (a) ADF-STEM image of the fresh drop-casted $CsPbBr_3$ NCs. (b) Another region of the same sample which remained unexposed to the electron beam, and has been stored for 1 week at room conditions. It can be seen that here the NCs have merged. (c) Local low-loss EEL spectra averaged over the regions shown in panels (a) and (b) represented by the blue and red spectrum, respectively. The band gap energy values extracted from its first derivative are 2.45 eV and 2.39 eV respectively. (d) Line defects are found in some NCs, identified with arrows. (e) Connected NCs share the same orientation, in this case along (0 0 1) direction. (f) The boundaries at the connections are clearly visualized.

Subsequently, we zoom-in to reveal more details of the merging between individual IP-NCs. Figure 5.3d shows a high-resolution ADF-STEM image of a densely deposited layer of freshly drop-casted NCs. For some NCs line defects can be distinguished, as indicated by the arrows; these could be related to the NC growth process. The merging process is very evident when we inspect the film which was stored for a week. Figures 5.3e and f show that the aggregation process connects NCs of the same size, but also of a different orientation and that the size of joining NCs does not seem to play a role. A more careful inspection of the images reveals that the new structures appear to be of high crystallinity, without borders between the merging NCs (figure 5.3e), while for some connecting NCs clear boundaries are present (figure 5.3f).

The ultimate illustration of the aggregation process is provided by imaging on a single NC level.

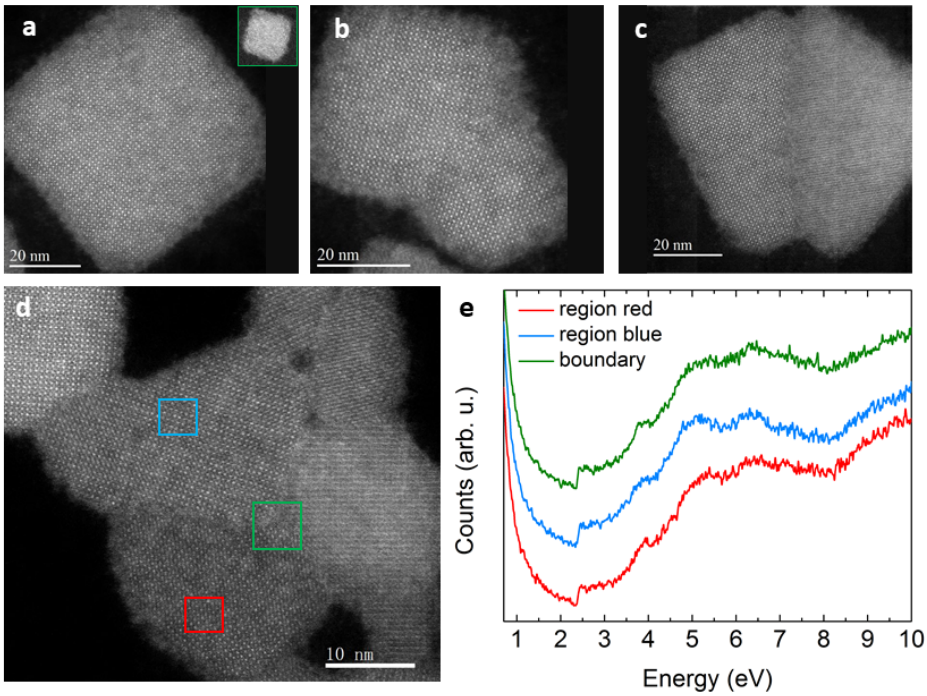

Figure 5.4: High resolution ADF-STEM images of single and merged IP-NCs and EELS scan across the boundaries between merged NCs. (a) Large $CsPbBr_3$ NC, which originates from the merging of smaller NCs. A 6 nm individual small NC is shown in the inset for comparison. (b) The NCs have merged with the same crystal orientation but different tilting angle. (c) Two NCs of a similar size have merged, but with a different zone axis. (d) ADF image of merged $CsPbBr_3$ NCs with visible boundaries, and (e) their corresponding EEL spectra. There is no noticeable difference in absorption behavior and band gap energy, where the boundary of merged NCs (green) and a smooth part of the film (blue and red) are compared.

Figure 5.4a shows a large IP-NC, with the edge exceeding 50 nm. For reference, also a 6 nm edge size NC from the originally drop-casted layer is shown as inset. We conclude that in this case the merge is ideal, creating an apparently monocrystalline structure throughout the cluster. A similar seamless stitching has been reported before for graphene flakes, where the mutual orientation of the individual flakes was crucial. [150] Here, the necessary alignment of individual IP-NCs with respect to each other is conveniently facilitated by spontaneous formation of the square superlattice in the drop-casted layer (as shown in e.g. figure 5.3a). Figure 5.4 also illustrates that, as noticed already before, merging of individual NCs can also occur in other configurations, with a tilted angle (figures

5.4b and d) or with a different zone axis (figure 5.4c). Therefore, we conclude that the stitching can occur between all neighboring NCs, independently of their size and orientation. This random stitching could be advantageous as it means that all neighboring NCs will fuse, creating a continuous thin perovskite film. A non-crystalline surface layer, which we identify with the stabilizing ligands, can be observed surrounding the newly formed structures. This implies that the ligands do not disappear upon merging but merely relocate, increasing the amount of hydrocarbon chains at the edge of the larger assemblies. We conclude that the growth of clusters - and also the subsequent development of large structures, such as long nanowires and extensive semi-continuous thin films of IP-NCs - proceeds by sequential merging of individual NCs and not by e.g. Oswald ripening, as the NCs merge together and not dissolve and redeposit (or recrystallize) into larger crystals.

The formation of perfectly uniform and crystalline large structures is possible by the seamless stitching, as illustrated in figure 5.4a. In general, the merged IP-NCs film can be viewed as a large plate with numerous smaller and larger (mono)crystalline domains formed by aggregation, with grain boundaries containing multiple structural imperfections (figure 5.3 d-f). Using EELS, we can now investigate the effect of these grain-boundary-related defects on the band structure of the film. To achieve that, we select a particular imperfectly merged cluster (with clear boundaries between connecting NCs) and monitor the EEL spectrum as we scan the electron beam between individual grains, across the interface. The experiment shows that the absorption spectra obtained by the locally conducted EELS are practically identical over the whole investigated trajectory within the IP cluster. This is illustrated in figures 5.4d and e, which compare three different spectra taken in the middle of the two adjacent grains and at their interface; a very close similarity is evident. Moreover, we notice that the EELS measurements of the merged film yield spectra practically unaltered from those of individual IP-NCs which we have shown previously (Chapter 3). A particularly striking feature is that the interface apparently does not introduce significant (detectable) defects in the band gap nor disturbs the band structure close to the band edges. This implies that even the obviously imperfect boundary arising upon layer formation does not yield defects and confirms the apparent defect tolerance of these materials. We conclude that the spontaneous orderly aggregation of IP-NCs offers a unique opportunity to create nanosheets (nanometer thick IP layers exhibiting QC related effects) whose characteristics can be predefined (tuned) by the properties of the used IP-NCs.

We now turn our attention to the practical aspects of the merging process itself. In general, the self-assembly of NCs drop-casted or spin-coated on a substrate from colloidal solution is governed by interactions between the NCs themselves and with the substrate, solution/substrate interface, drying kinetics (solvent- and temperature-dependent), among others. [151] The contact between colloidal semiconductor NCs themselves is facilitated by the Van der Waals forces, which are weak and can easily be overcome by steric repulsions using stabilizing ligands. Nevertheless, the highly dynamic behavior of the ligands on the IP-NCs surface (the binding is not strong and they can move and be easily lost, mainly during the purification process) as well as the ionic character of the IP-NCs' bonding, renders this material to disintegrate in polar solvents. [113] These characteristics are important for manipulation and, eventually, for controlling the assemblage of IP-NCs. In the following section, we discuss how electron beam irradiation, humidity, and thermal annealing at different temperatures affects the merging.

5.4 Electron beam induced transformations and degradation of IP-NCs

Electron irradiation can affect the ligands that are present at the surface of the deposited IP-NCs, leading to the formation of intermolecular C=C bonds between them, and also between the ligands and the carbonaceous grid; in both cases the IP-NCs stability would be enhanced. [17] This is indeed confirmed in our experiments: figure 5.5a shows an image of drop-casted IP-NC stored for 1 week at room conditions; the left part has been exposed to an electron beam directly after deposition, while the right hand side not. As can be seen, the NC aggregation has taken place only in the non-irradiated part of the sample, thus illustrating the stabilizing action of the electron beam. Typically, aggregation processes are strongly temperature-dependent, and this is also the case for the IP-NC layers, with their merging being accelerated by mild-temperature treatments due to the removal of surface ligands. [139]

On the macroscopic level this is evidenced by the fact that IP-NCs films on quartz treated at mild temperatures show a decrease of the emission intensity and PL QY due to defect formation (figure 5.2b), in agreement with previous reports. [139, 152] On the microscopic level, this is represented by figure 5.5b, which shows the behavior of electron-irradiated and non-irradiated regions of a low concentration IP-NCs layer, but now annealed at 90 °C for 1 hour. While the NCs in the electron irradiated region remain isolated, the merging process in the untreated part of the sample is clearly enhanced. When the initial NC density is high, the same treatment results in a complete fusion of individual NCs into a semi-continuous film (5.5c). For the development of high quality layers, however, the annealing temperature will need to be optimized, as high-temperature treatments destroy the IP-NCs. In figure 5.5d a small cluster of 14 NCs is imaged directly after drop-casting; an amorphous layer of ligands is clearly visible on the surfaces of individual NCs. The electron irradiation stabilizes the ligands, as discussed before, arresting the possible merging. Figure 5.5e shows the same cluster after being heated at 260 °C for 1h: the IP-NCs have been completely destroyed with a small metallic nanoparticle being formed from the IP-NCs debris, while the residual shell of ligands remains, now surrounding the empty spaces.

It is also well-known that if IP-NCs come in contact with polar solvents (such as water), they dissolve and are destroyed. On the other hand, past research has shown that ethanol can actually promote the growth of IP-NCs through surface ligands destabilization. In that way, it can induce partial dissolution and subsequent recrystallization of NCs - the effect can therefore serve as ”healing” of the film. [146, 153] Therefore, we have investigated the influence of water vapor on the NCs merging, and compared two samples stored for 1 week in dry (relative humidity RH = 20%) and high-humidity atmosphere (RH = 60%). The results (figure 5.5f and g) clearly show that the water vapor accelerates the NCs fusion process. However, more detailed investigations are required to determine the optimum RH level for the merging process, similarly as for the thermal treatment.

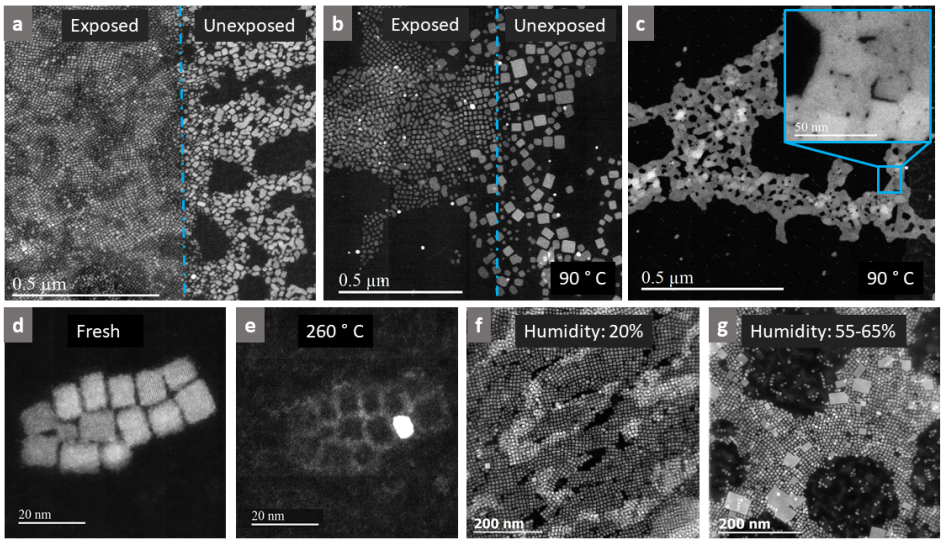

Figure 5.5: Influence of electron beam irradiation, annealing temperature and humidity on the IP-NCs merging. (a) High density IP-NCs layer which was stored in vacuum 1 week, being partially irradiated with electrons just after deposition. In the irradiated part, the merging is arrested. (b) Lower IP-NCs density layer annealed at 90 °C for 1h being partially irradiated with electrons just after deposition. (c) The IP-NCs annealed at 90 °C for 1h without electron irradiation. The inset shows a zoom-in of a part of the sample. (d) ADF-STEM image of an isolated cluster, containing 14 $CsPbBr_3$ NCs. (e) The same cluster after 1h annealing treatment at 260 °C. The bright dot is due to a residual metallic nanoparticle shell and ligands. (f-g) ADF-STEM image of drop-casted $CsPbBr_3$ NCs stored for 1 week in vacuum with RH = 20% (f) and in a humidifier RH = 60% (g).

5.5 Conclusions

The colloidal IP-NCs drop-casted on a substrate form spontaneously a semi-homogeneous thin film. A thorough microscopic investigation by STEM and EELS reveals that the layer formation proceeds by merging of individual NCs. We show that the fusion is accelerated by mild temperature annealing in a humid atmosphere. Surface ligands play an active role in the aggregation process, which is arrested or totally prevented, by their stabilization upon electron irradiation. Most importantly, on the atomic level, we find that the merging process does not introduce apparent defects in the band gap or at the band edges, and even near-perfect seamless stitching between aligned NCs is possible. Since crystallographic alignment naturally arises in drop-casted dense layers of IP-NCs, this implies that in future this process could be explored for the formation of thin IP films of superior quality. Our results demonstrate the fundamental growth conditions for the development of these sheets; future research must show whether its growth can be extended to cover large areas.

6

Energy transfer between $CsPbBr_3$ perovskite nanocrystals

In this Chapter, energy transfer between proximal $CsPbBr_3$ NCs is demonstrated and discussed. Using (time-resolved) optical characterization of purposefully prepared batches of NCs with different sizes, we identify the energy transfer which can be driven by the concentration gradient of excited NCs as well as by the band gap energy difference. The latter process moves the energy from smaller to larger NCs and opens a possibility of directional streaming of the excitation energy in these materials. The observed energy transfer is enabled in the colloids by proximity of individual NCs due to clustering.

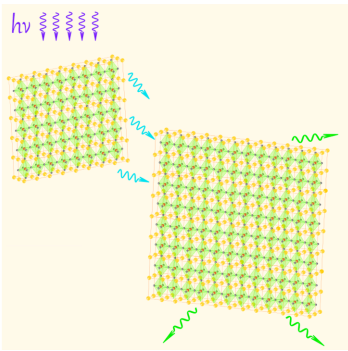

6.1 Introduction

An efficient energy and/or carrier exchange between proximal NCs provides a huge application potential, because it enables long-range transfer of electronic energy. In photovoltaic cells, an exciton generated upon photon absorption needs to be either separated into an electron and a hole pair and the free carriers are transported towards the respective electrodes (semiconductor cells) or moved towards an interface and be split there (polymer cells). In any case, the energy transport can be enhanced through efficient transfer and is no longer limited by the diffusion length of the charges. There are three possible mechanisms [154] responsible for exciton transfer: cascade energy transfer (involving the emission and subsequent reabsorption of a photon), Dexter transfer (involving electron exchange interactions) and Förster Resonance Energy Transfer (FRET), mediated by Coulomb interactions between a donor and an acceptor. Here, we explore the energy transfer (ET) between NCs, from a donor to an acceptor with a lower band gap energy. ET between direct band gap semiconductor NCs is typically described by dipole-dipole interaction and FRET, [155] which depends on the spectral overlap of donor emission and acceptor absorption, and the donor-acceptor Coulomb coupling, determined by the distance between them. ET in closed-packed quantum dot solids of direct band gap semiconductors (CdSe, CdTe, PbS, InP etc.) has been demonstrated in the past by means of changes in the PL spectra and lifetimes. [156, 157] Also, the energy exchange between NCs of silicon, has been conclusively established. [158] In hybrid perovskite based solar cells, energy exchange has recently been observed between perovskite films and layers of organic electron and hole acceptors. [159] Accordingly, also exciton transfer between perovskite NCs could be expected but has not yet been observed. To the contrary, a recent study on perovskite NC films revealed no evidence of ET. While this negative result was tentatively explained by the large sizes of the investigated materials, further research is needed. [6]

6.2 Synthesis and optical characterization

$CsPbBr_3$ NCs were prepared at two different synthesis temperatures of 160 °C and 200 °C. Figure 6.1 shows the optical characterization and TEM images for the materials used in this study (samples A and B). The PL bands (figure 6.1a) centered at 2.43 eV and 2.36 eV for samples A and B with full widths at half-maximum of 0.1 and 0.089 eV, respectively, show a small Stokes shift from their corresponding absorption spectra that exhibit a clear excitonic peak at the onset. The inset shows the samples under UV illumination indicating that they are similarly bright to the eye; a minor difference in color can hardly be noticed. We have determined PL quantum yields of 90% and 30% for samples A and B respectively. The TEM images with their corresponding histograms (figures 6.1b-e) confirm the formation of (mostly) cubic NCs with an average edge size of 8.4 $\pm$ 1.4 nm and 18.3$\pm$ 2.8 nm for samples A and B, respectively. We note that synthesis at a higher temperature (sample B) leads to a larger size distribution of the NCs and an occasional shape deformation. A similar PL linewidth of both samples (figure 6.1a) in spite of the significantly broader size distribution of sample B (figures 6.1c and e) is the first indication of a possible excitation flow into a smaller sub-ensemble of emitters.

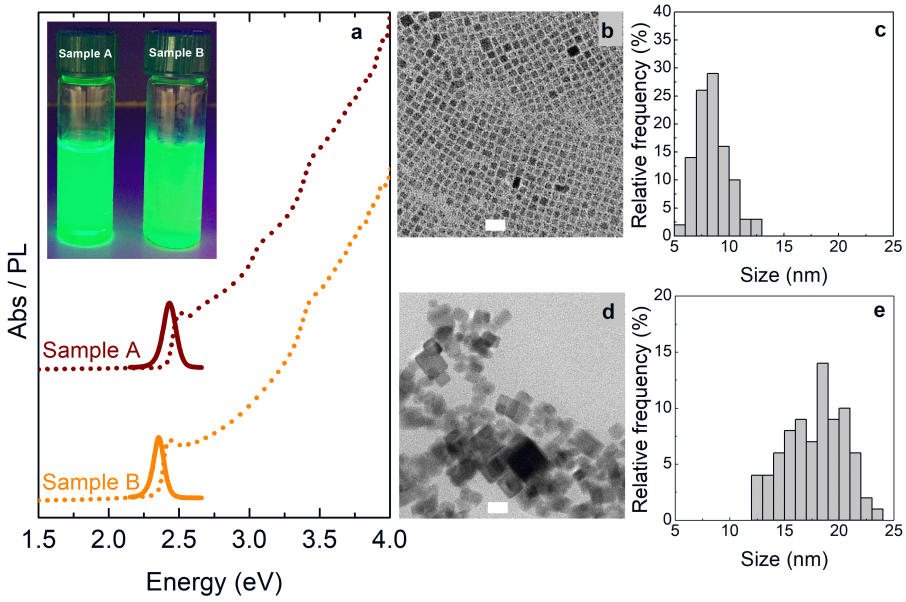

Figure 6.1: Sample characterization. (a) Absorption and photoluminescence spectra of samples A and B. The inset shows the samples under UV illumination (λ_{exc}=365 nm). TEM images with the corresponding histograms of both samples indicating cubic NCs with an edge size of 8.4 $\pm$ 1.4 nm (b,c) and 18.3 $\pm$ 2.8 nm (d,e).

6.3 Energy transfer

In case that the energy transfer takes place, one can expect that the ensemble emission spectrum will be reduced on the high-energy side, and part of this intensity loss will reappear at a lower energy, since transfer only occurs from smaller to larger NCs. Such a spectral deformation can be induced by reabsorption of higher energy photons or by direct (photon-less) ET between adjacent NCs; in either case, the measured PL band will be red-shifted and will not have the usual Gaussian distribution of photon energies (resulting from the Gaussian distribution of NC sizes). Since the optical characteristics of the investigated samples are known, the PL spectrum can be easily corrected for reabsorption using the Beer-Lambert law: [160, 161]

$$\log_{10} \frac{I^0(\lambda)}{I(\lambda)} = OD \tag{6.1}$$

where $I^0(\lambda)$ is the reabsorption-free emission, $I(\lambda)$ is the measured emission and OD is the optical density determined from the steady-state absorption. Figure 6.2 shows the PL spectrum

of sample A as measured (black, dotted) and corrected for reabsorption (black); as can be seen, the corrected PL spectrum shifts to the blue but remains asymmetric. On the other hand, being strongly distance-dependent, FRET can be fully eliminated by sufficient dilution. Indeed, we have observed that with increasing dilution the PL spectrum continues to blue-shift until it stabilized upon reaching a sufficiently low NC concentration - see the gray spectrum in figure 6.2a. We note that upon sufficient dilution, the PL spectrum attains the Gaussian shape, as expected. We conclude that the gray spectrum represents the "true" PL of sample A, free from any effects of ET. The fact that it is not identical to the one corrected for reabsorption (black), indicates an additional process takes place yielding this discrepancy, and suggests the presence of ET. In case of molecules, when the donor can be selectively excited, the ET can be directly monitored by investigating the PL dynamics, [156] by the time-dependent rise of the acceptor emission. In case of ET between NCs, it is not possible to excite the donor without simultaneous excitation of the acceptor. However, the lengthening of the PL lifetime as a result of multiple ET events taking place prior to radiative recombination, should appear. We note that in principle the lengthening of the PL lifetime can also appear due to a change in the dielectric constant of the sample as the NC density increases. However, due to the low volume fraction (of the order of 10^{-6}) of the colloids investigated in this study, this effect can be neglected. [113] Figure 6.2b shows the time-resolved PL signal at 2.38 eV for sample A before and after dilution, i.e., with the highest and the lowest NC density. As can be seen, the PL lifetime increases with NC density. This is readily explained by a higher probability of ET as the NCs are closer together, with the multiple ET events lengthening the lifetime. The increase of the lifetime is most significant on the low-energy side, since the transfer takes place from smaller (donors) to larger (acceptors) NCs. To further investigate the possible PL dynamic change by ET, we measured the time-resolved PL signal at different detection energies. This is shown in figures 6.2c and 6.2d for samples A and B, respectively. As can be seen, they both show a gradual increase of the PL lifetime towards lower energies, consistent with ET towards larger NCs.

A measure for the ET can be made by comparing the emission of the as-prepared (ET takes place) and diluted (no ET takes place) samples (corrected for reabsorption). This is done by fitting both spectra using a number of Gaussian subcomponents centered at arbitrary chosen energies (figures 6.3a and b). Upon ET, part of the emission on the high-energy side will decrease and subsequently reappear on the low-energy side. In this way, the area under each respective Gaussian (with the same peak energy) can be compared, providing a measure for the (maximum) amount of transferred excitons. In addition, the PL spectrum of the as-prepared sample could be fitted with a single Gaussian distribution where there remains a large discrepancy on the low-energy side. The difference in integrated area under both curves is a measure for the minimum amount of excitons that are transferred and is shown in figure 6.3c. We find a maximum increase of 50% at 2.4 eV induces by the red-shift, and a minimum decrease of 95% as a result of the energy transfer from the donor to the acceptor.

In order to prove the presence of ET in the investigated material, we performed a dedicated experiment. For that purpose we mixed samples A and B at different ratios (A:B volume ratio equal to 4:1, 1:1, and 1:4), and subsequently recorded the PL spectra and decay dynamics of the mixed colloids. In order to preliminarily reduce the effects of reabsorption, samples A and B have been diluted prior to mixing such that the correction for reabsorption does not induce a considerable

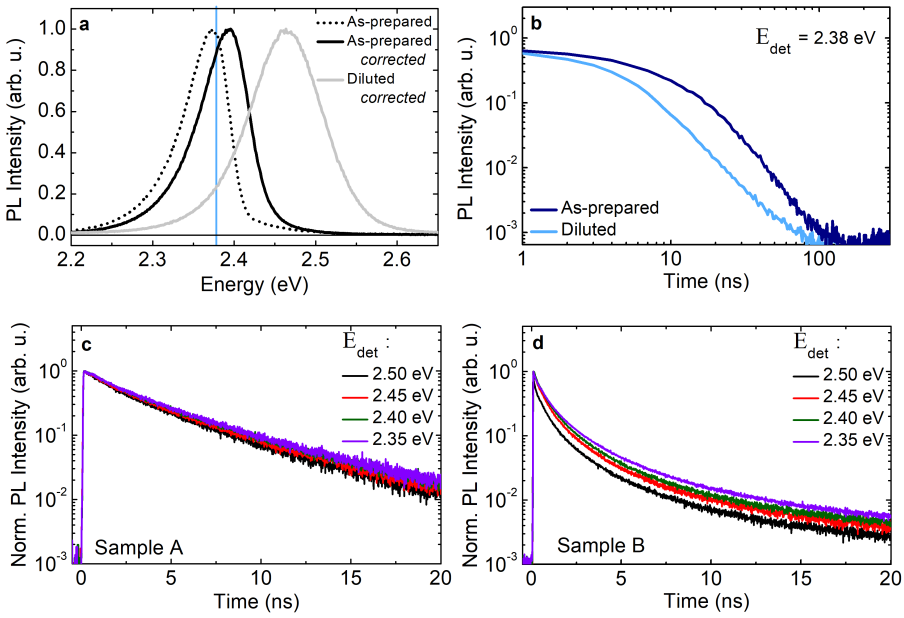

Figure 6.2: PL and time-resolved PL data. (a) The normalized PL spectrum for as-prepared (black) and sufficiently diluted (grey) colloid, corrected for reabsorption. Plotted in the same graph is the uncorrected spectrum of the as- prepared sample, to demonstrate the effect of reabsorption on the emission. The solid line indicates where the time-resolved signal depicted in panel (b) has been collected. (b) The PL decay detected at 2.38 eV for the respective samples, showing an increase of the lifetime with increasing NC concentration. (c, d) The normalized time-resolved PL signal recorded at different detection energies for samples A and B, showing a decrease of the lifetime at higher detection energies, i.e., for smaller NCs functioning as energy donors.

change of the spectrum. We note that ET can still take place since upon even further dilution, a considerable blue-shift of the PL spectrum was observed, as ET can be eliminated by reducing the concentration (as previously explained in figure 6.2a). Nonetheless, all PL spectra are corrected for a possible remaining reabsorption. Figure 6.3d shows the PL spectra of the samples A and B, and their different mixtures. We clearly observe a shift of the PL spectrum, with the maximum changing continuously from that of the small NCs (sample A) to that of the larger ones (sample B). Furthermore, for the 1:1 and 1:4 mixing ratios (blue and green spectra), a shoulder appears, being consistent with the two different sizes present in the sample. Figure 6.3e shows the time-resolved PL signal for samples A and B and the 1:1 mix (brown, orange, blue), detected at 2.39 eV. Included in the same graph is the simulated decay trace of the 1:1 mixed sample. This is obtained by summing the two experimentally obtained PL decay signals of samples A and B and subsequent dividing by two. It can be clearly seen that the simulated and the experimentally obtained PL decays are not

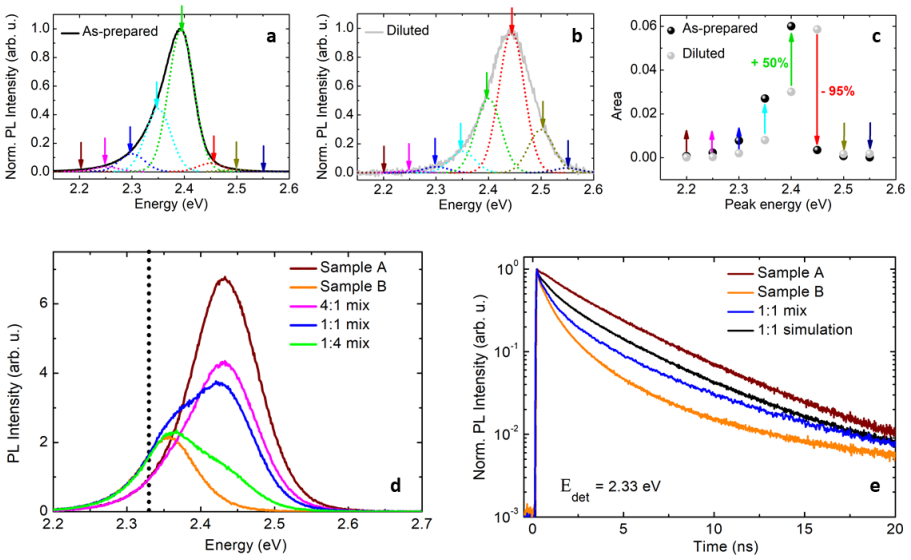

Figure 6.3: (a,b) PL spectra (corrected for reabsorption) of sample A as-prepared (black) and diluted (grey). The spectra are fitted using a number of Gaussian subcomponents (dotted lines) with the same peak energy for both samples (indicated by the colored arrows). (c) The integrated area under the for the in (a) and (b) shown Gaussians, as a function of the energy. The arrows indicate the in- and decrease in area. As such, we find a maximum increase of 50% at 2.4 eV (due to the red-shift) and a decrease of 95% at 2.45 eV (due to the energy transfer). (d) PL spectra (corrected for reabsorption) of samples A (brown) and B (orange), and of the mixed compositions with A:B ratios of 4:1 (pink), 1:1 (blue) and 1:4 (green). For the mixed samples, the PL peak moves gradually from A to B accompanied by an intensity decrease. (e) The normalized time-resolved PL signals recorded at 2.33 eV for samples A and B and the 1:1 mix. Included is the simulated decay, as determined from adding the signals from samples A and B according to their mixing ratio.

identical. This indicates that an additional transfer processes is enabled upon mixing. The ET can be further analyzed by comparing the experimentally measured PL spectra of the mixed samples with simulations. The latter are obtained, similarly as shown in figure 6.3e for the PL decay dynamics, from adding the measured PL spectra of samples A and B according to the mixing ratios. Figure 6.4 shows the PL spectra of sample A and B and the 1:1 mixed colloid (solid lines). The dotted lines indicate the simulated spectra using nominal (figure 6.4a) and scaled (figure 6.4b) 1:1 composition. A considerable ET from the donors to the acceptors has to be assumed in order to fit the experimental data: the contribution of the large NCs to the emission had to be enhanced by a factor of 1.6. This is the result of donors transferring their energy instead of emitting. For the 4:1 and 1:4 mixed colloidal suspensions, similar discrepancies between the experimentally measured and simulated PL spectra are observed.

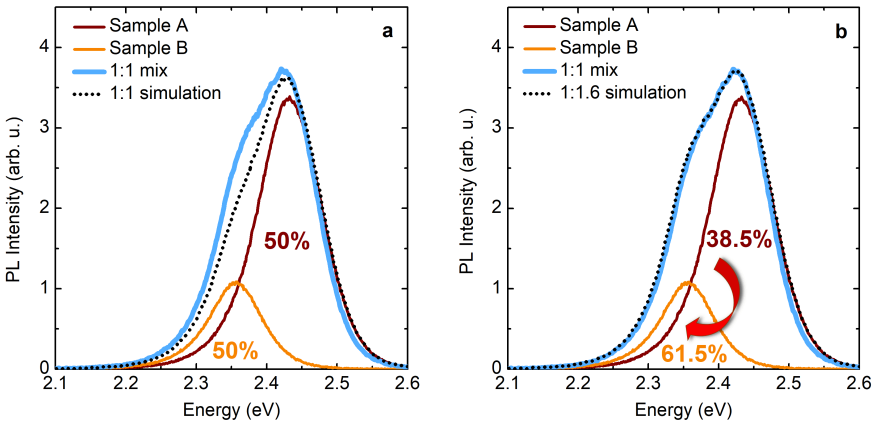

Figure 6.4: Energy transfer. (a) PL spectra of sample A and B and the 1:1 mixed colloid. The dotted lines represent the simulated PL spectra of the mixed sample using nominal (a) and scaled (b) composition. As can be seen, in order to correctly reproduce the experimentally recorded PL spectrum a considerable energy transfer from small NCs (sample A) to large NCs (sample B) has to be assumed. All PL spectra have been corrected for reabsorption.

The spectral and temporal changes as shown in figures 6.3 and 6.4, cannot be modeled and predicted correctly using equal contributions of the donors and acceptors and indicates the presence of ET: figure 6.4b shows a considerable transfer from the donor to the acceptor. For completeness, we note that an alternative explanation of spectral modification by ligand exchange between NCs of samples A and B upon mixing, [113] can be disregarded since, as discussed, evidence of ET has also been obtained for both samples separately, before mixing. However, the dynamic interaction of the ligands with the NC surface can be responsible for clustering of the NCs with time, which, in term, enables the ET. In the past investigations, ET between semiconductor NCs has mostly been observed in close-packed solids and seldom in dispersed colloids. [156,158,162] In order to further investigate the ET in colloidal dispersions reported here, the NCs aggregation is examined. The TEM results revealed the presence of NC clusters (figure 6.5a). Although we have seen in Chapter 5 that these NCs self-assemble upon drop-casting, it is consistent with the observations of precipitated - and not merged - NCs and it also explains the spectral modifications upon time. An enhancement of ET as the colloids are allowed to settle for a few hours after mixing is observed (figure 6.5b and c). Upon clustering, the contribution of the acceptors emission to the PL spectrum significantly increases. This indicates ET between NCs, but could alternatively be explained by the sintering and formation of bigger, more bulk-like pieces of material. However, in that case, the PL maximum would red-shift to the bulk emission value ($\sim$2.33 eV), which is not observed.

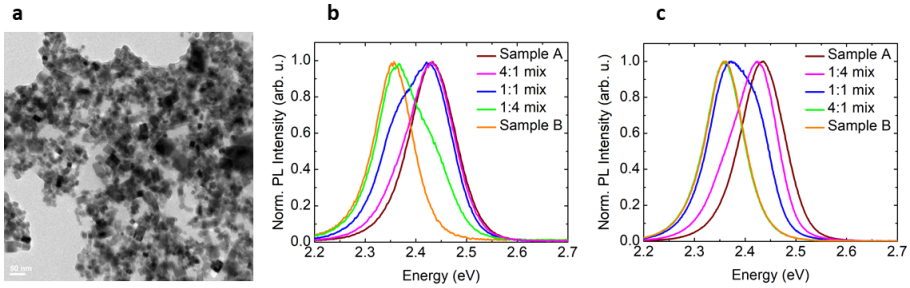

Figure 6.5: TEM image of the mixed sample with A:B ratio of 1:4. Clearly, aggregation of NCs can be seen bringing them in direct contact with each other. No observations are associated with the drop-casting on the TEM grid, as concluded from previous studies. (b,c) Normalized PL spectrum of samples A, B and the mixed compositions recorded directly after mixing (b) and five days after mixing (c). For all mixed samples the PL has red-shifted upon time, indicating clustering. The emission of the 4:1 mixed sample is now similar to that of the large NCs.

6.4 Conclusions

We have established the presence of effective ET between inorganic perovskite $CsPbBr_3$ NCs in colloidal state, driven by concentration and energy gradients. The ET has been identified by mixing NCs of different sizes which demonstrates the transfer process proceeding from small to large NCs. It is enabled through the aggregation and clustering of NCs, which brings them in close contact with each other.

7

Color-stable water-dispersed cesium lead halide perovskite nanocrystals

It is well-known that the incompatibility of IP-NCs with polar solvents and the composition homogenization driven by a fast anion-exchange, are important drawbacks. In this Chapter, we demonstrate a successful encapsulation of colloidal IP-NCs in lipid solid structures made of stearic acid. The product is water-stable for a period longer than three weeks and anion-exchange is fully arrested when mixing NCs of different halide composition. This development boosts the potential of the IP-NCs for various applications, such as ink-printing and bio-imaging, among others.

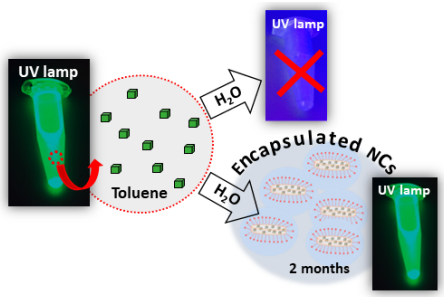

7.1 Introduction

Despite the attractive features that the IP-NCs exhibit, e.g. tunable emission with high PL QYs and narrow emission bands, they also have some important limitations. Their incompatibility with moisture, air instability, the presence of the toxic element lead and thermal decomposition are few of these limitations. [27] In this Chapter, we focus our research on two main drawbacks: (i) their incompatibility with polar solvents, and (ii) fast anion-exchange when IP-NCs of different halide composition are mixed. Colloidal IP-NCs lose the structural integrity in the presence of polar solvents due to their inherent ionic structure and the dynamic stabilization of the surface ligands (oleylammonium bromide, oleylammonium oleate and oleylamine) which involves fast desorption. [113] There have been recent efforts to enhance their stability in air using a new surface passivation technique, which helps to slow down the NCs degradation against atmospheric moisture. [163] Also, using branch-structured capping ligands has been reported to improve their stability in polar solvents. [164] X-ray lithography has been used on NCs films to form intermolecular bonds between the organic surface ligands achieving, however, only a few days stabilization of the film immersed in Milli-Q water or buffer saline. [17] Besides, the encapsulation of NCs by micelles formation of lipid molecules has been widely studied. [165, 166] Water-resistant $CsPbX_3$ NCs have been obtained so far only by robust non-porous coatings, such as silica spheres and polyhedral oligomeric silsesquioxane synthesized using water-free processes. [167, 168]

With a view on optoelectronic applications, it is necessary that NCs of different composition maintain their own emission characteristics when mixed. However, this is currently impossible as a fast anion-exchange (10 - 20 minutes) takes place, leading to composition homogenization. [18] For instance, mixing $CsPbBr_3$ and $CsPbI_3$ NCs at room temperature will yield $CsPb(Br/I)_3$ NCs, and the resulting PL emission will be centered in between those of the initial materials. This color instability renders IP-NCs not suitable for many imaging applications where the presence of different colors is required in order to cover the whole spectral range visible to the human eye. To overcome these limitations, we establish the encapsulation of colloidal cesium lead halide IP-NCs within solid lipid nanoparticles (SLNs). [169, 170] SLNs are made of lipids - which are solid at room temperature - and stabilized by emulsifiers in water. They are commonly used as drug carrier systems since they offer advantages lilke high drug payload, increased drug stability, controlled drug release, nontoxicity, feasibility of sterilization and lyophilization, and the possibility of large scale production. In addition, SLNs have already been used for the encapsulation of colloidal Si NCs and Au nanoparticles for fluorescence cell labeling purposes. [171, 172] We demonstrate that the colloidal encapsulation of IP-NCs by SLNs renders them water-stable and arrest composition homogenization for at least three weeks.

7.2 Synthesis, microscopic and optical characterization

The IP-NCs were synthesized as described in Ref. [5] (see also the Appendix). The absorption and emission of these IP-NCs can be tuned along the visible range by changing the halide composition, producing blue/purple-, green- and red-emitting NCs (X = Cl, Br, and $Br_{0.2}I_{0.8}$, respectively, see figure 7.1a) with high PL QYs (QY_{Cl} = 52%, QY_{Br} = 85%, QY_{BrI} = 33%). The product has a

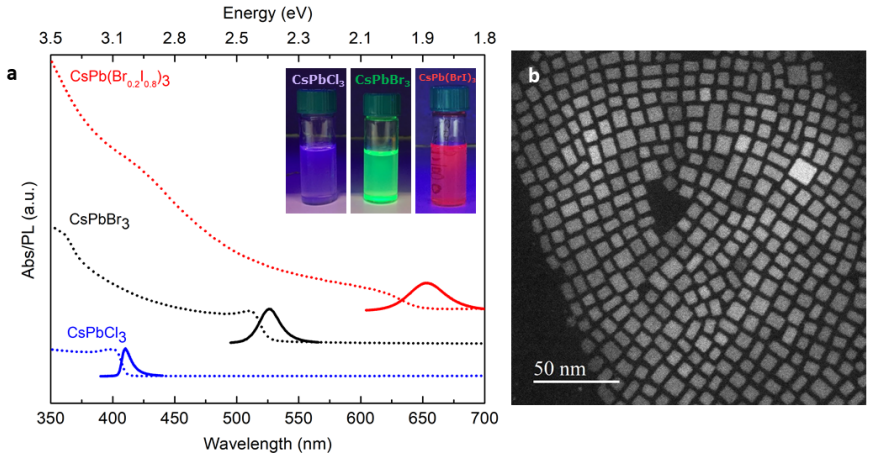

Figure 7.1: Optical and microscopic properties of the IP-NCs. (a) Absorption and PL spectra of three different halide composition perovskites $CsPbX_3$ (X = Cl, Br, $Br_{0.2}I_{0.8}$) in toluene, the inset shows the corresponding emission colors under UV lamp irradiation (λ_{exc}=365 nm). (b) TEM image of $CsPbBr_3$ NCs drop-casted on a copper grid.

cubic morphology as can be seen from the TEM image shown in figure 7.1b, and the NC size can be tuned from 4 to 15 nm by the reaction temperature (140 - 200 °C). The PL lifetimes are of the order of ns, in agreement with previous reports. [5]

SLNs loaded with IP-NCs were prepared by sonication-assisted melt homogenization, as schematically shown in figure 7.2. As a lipid matrix we chose stearic acid, a saturated C18 fatty acid, since it is commonly used as a drug carrier because of its melting point of 69.6 °C, which is higher than the human body temperature. [173] As emulsifier, we used the surfactant Poloxamer 188 (a non-ionic triblock copolymer) without a co-surfactant. Briefly, the stearic acid was melted in a toluene solution of NCs, and the mixture was transferred to the emulsifier water solution. Then, the two-phase suspension was sonicated in a cold water-bath to create an emulsion and to solidify the stearic acid. After toluene evaporation and sample centrifugation, the final product redispersed in Milli-Q water which shows an opaque white color while the characteristic emission of the IP-NCs was observed under UV lamp illumination.

The SLNs with IP-NCs were visualized by STEM and HR-TEM showing a platelet-like shape. The first fabrication attempt resulted in lipid structures of heterogeneous size, ranging from several nm to 5 μm (figure 7.3a). By subsequent adjustments and improvements of the SLNs synthesis (reducing the amount of lipid and decreasing the temperature of the sonication bath), we managed to reduce the platelets size and improve their size distribution. The solid lipid platelets randomly dispersed on the STEM grid are oriented parallel to the observation plane, with an average size of 700 $\pm$ 240 nm (figure 7.3b). In addition, some rod-shape particles can also be seen in figure 7.3b. As we have seen in Chapter 3, other nanoshapes appeared as a subproduct in the NCs synthesis

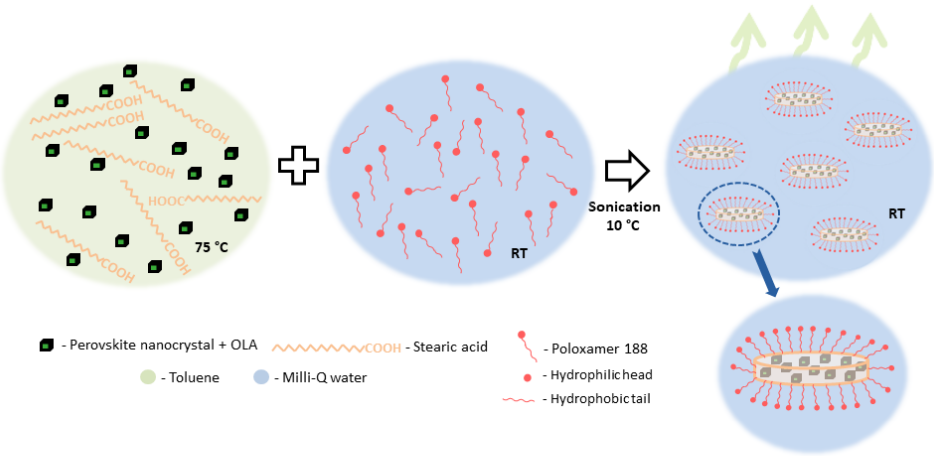

Figure 7.2: Procedure of the encapsulation of $CsPbBr_3$ IP-NCs in a solid lipid matrix of stearic acid by sonication-assisted melt homogenization.

and can be purposefully synthesized by adjusting the reaction time and temperature. If we apply HR-TEM imaging on a layered solid lipid platelet, we can see the IP-NCs embedded in the matrix (figures 7.3c and d). We observe a decrease of the size of the NCs after the encapsulation process, from 7.2 $\pm$ 1.4 nm to 3.8 $\pm$ 0.7 nm for the green emitting sample (fresh NCs figure 7.1b and after encapsulation figure 7.3d) and their cubic morphology changes somewhat with rounded corners. During the encapsulation process, unfortunately, the IP-NCs suffer from being in brief contact with the water - which explains the observed change of the average size and morphology.

7.3 Water-solubility

We compare the water-stability of free-standing and encapsulated IP-NCs by recording the PL intensity as a function of time (figures 7.4a and b). Colloidal NCs in contact with Milli-Q water disintegrate within few minutes (5 - 15 min) and their PL vanishes. In particular, the disintegration of $CsPbCl_3$ NCs (λ_{em} = 420 nm) transforms the available ions into blue emitting CsCl (λ_{em} = 380 nm) with broader emission than the initial material. On the other hand, $CsPbBr_3$ and $CsPbBr_{0.2}I_{0.8}$ encapsulated NCs dispersed in Milli-Q water still emit light after three weeks. The encapsulation of $CsPbCl_3$ was not successful as these NCs disintegrated before the lipid capsules were made. At the same time, a decrease of the NCs PL intensity over time is observed, most pronounced for $CsPbBr_3$, being related with the precipitation of agglomerates. SLNs may form larger structures by the phenomena known as gelation which can be stimulated by different conditions, such as insufficient stabilization, removal of the emulsifier from the particle surface by dilution, or intense contact between the SLN due to high concentration or contact with other surfaces. According to our obser-

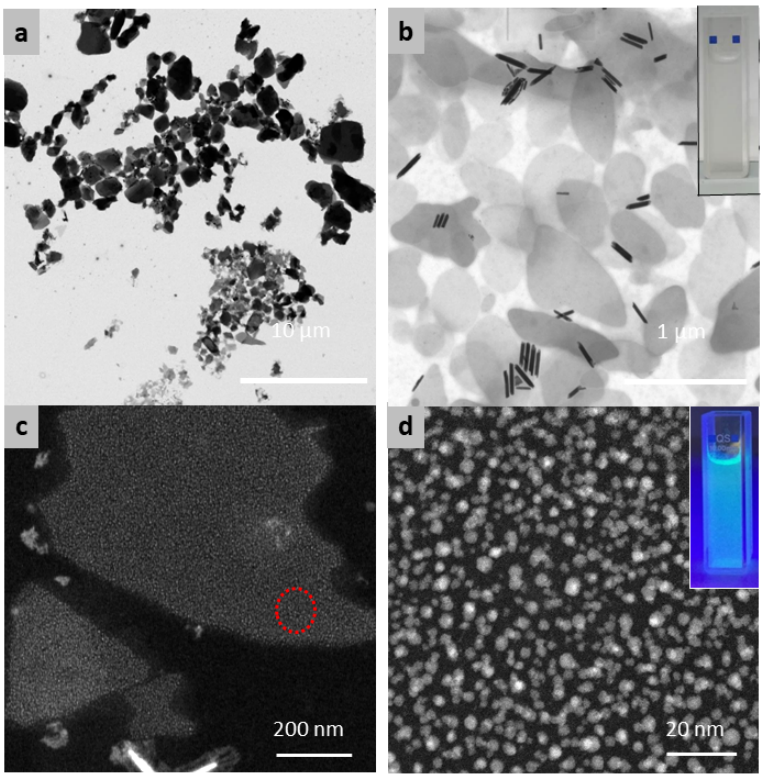

Figure 7.3: Microscopic characterization. (a) STEM image of a heterogeneous sample of stearic acid SLN with $CsPbBr_3$ NCs inside. (b) STEM image of $CsPbBr_3$ NCs embedded in platelet-like shape structures with average size 700 $\pm$ 240 nm (N = 150), some fibers can also be observed; the inset shows the sample illuminated with room light. (c) HR-TEM image of the IP-NCs embedded in lipid platelets. (d) HR-TEM zoom-in image of a lipid structure (red circle of image c) where the IP-NCs are visualized inside the matrix; the inset shows the emission of the sample under UV lamp (λ_{exc} = 365 nm) illumination.

vations, storage time and exposure to an excitation source during PL experiments induces the SLNs to agglomerate and subsequently precipitate.

After the encapsulation process, the PL maximum of ensemble spectra blue-shifts for both, $CsPbBr_3$ and $CsPbBr_{0.2}I_{0.8}$ NCs, with respect to the PL spectra of the initial NCs dispersed in toluene (figures 7.4c and d and their insets). This PL blue-shift can be explained by the earlier-mentioned size reduction of the NCs due to surface degradation during the encapsulation process. Besides the change in NCs size, a mechanical compression induced by the capsules could also contribute to enhance the observed PL blue-shift. The PL lifetime of the encapsulated IP-NCs remains

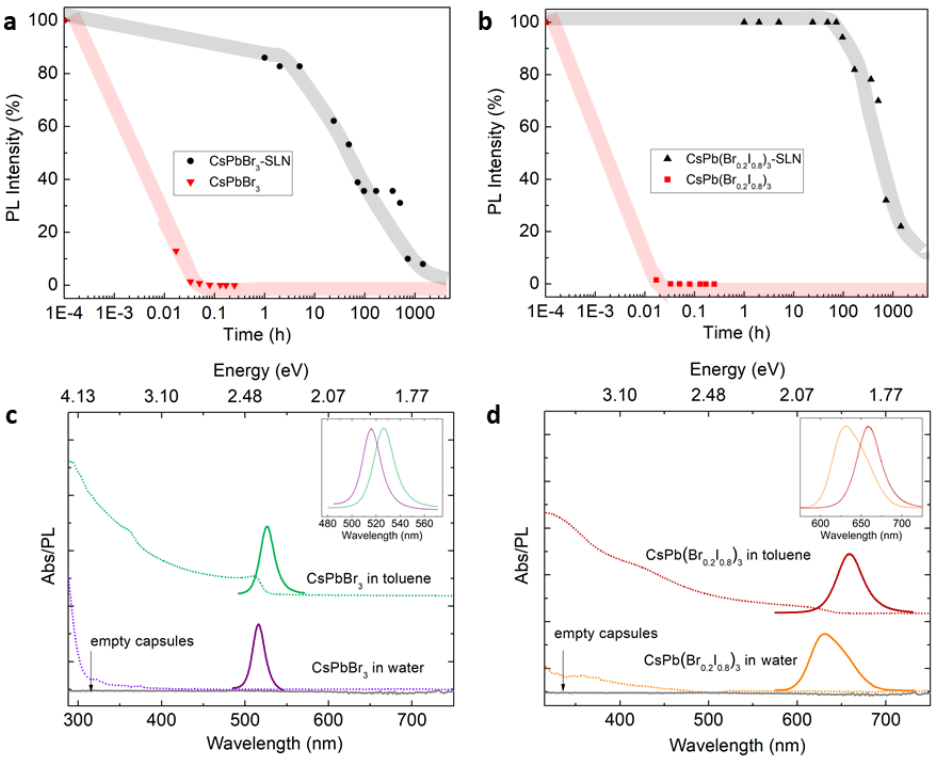

Figure 7.4: PL intensity as a function of time of free-standing (red) and encapsulated (black) $CsPbBr_3$ (a) and $CsPbBr_{0.2}I_{0.8}$ (b) NCs dispersed in Milli-Q water. The PL intensity is normalized (100%) to the value in toluene before the NCs came in contact with Milli-Q water (red) and compared with the emission intensity belonging to freshly prepared but encapsulated IP-NCs (black). (c,d) PL (solid lines) and absorption (broken lines) of colloidal $CsPbBr_3$ NCs (c) before and after encapsulation (in toluene *vs.* water) as well as for $CsPbBr_{0.2}I_{0.8}$ NCs (d). The absorption spectra of the solid lipid platelets without NCs is also shown in both graphs (empty capsules). The insets show the comparison between the PL spectra, to better observe the blue-shift as a result from the encapsulation process.

in the order of ns, while the PL QY decreases after the encapsulation process (QY_{Br-SLN} = 13%, $QY_{BrI-SLN}$ = 9%). The change in PL QY suggests NCs degradation during the encapsulation process, as we have perceived from the HR-TEM images (figure 7.3d). It is worth noting, however, that the lipid matrix itself, without IP-NCs, does not absorb light in the studied region (see the empty capsule absorption spectra in figures 7.4c and d).

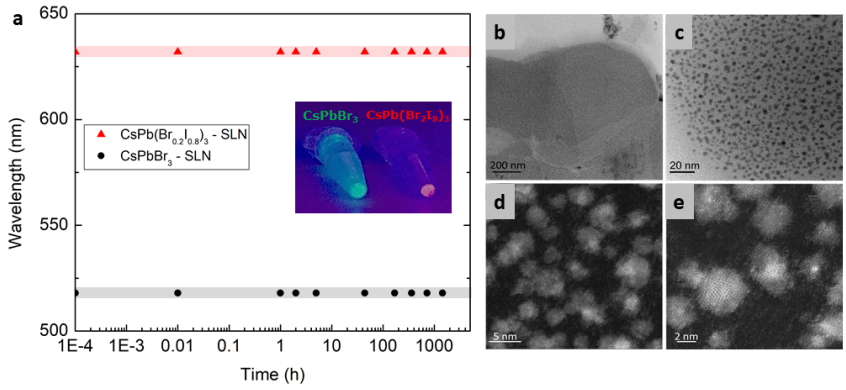

Figure 7.5: Color stability and preservation of the IP-NCs with time. (a) Maximum peak position as a function of time of the corresponding IP-NCs PL emission after mixing encapsulated $CsPbBr_3$ (black) and $CsPbBr_{0.2}I_{0.8}$ (red) in Milli-Q water. The inset shows the emission color of the two samples under UV lamp illumination (λ_{exc} =365 nm).(b,c) Additional STEM images taken five months after the encapsulation process which shows the capsules and the NCs embedded therein are intact and have not degraded. (d,e) TEM images of the NCs in the capsules.

7.4 Color stability

To investigate the effect of encapsulation on anion-exchange and hence the color stability, the two different types of IP-NCs embedded in SLNs were mixed in Milli-Q water, and their PL was recorded as a function of time. As can be concluded from figure 7.5a, the maximum of the emission peak of each sample ($CsPbBr_3$ - 518 nm, and $CsPbBr_{0.2}I_{0.8}$ - 632 nm) remains in the same position even after two months. This implies that composition homogenization does not take place, with the process of anion-exchange being fully arrested. Even though the PL intensity diminishes with time, the capsules and the IP-NCs themselves are preserved. This is shown in figures 7.5b-d by additional STEM (b,c) and TEM (d,e) images taken five months after the encapsulation process. The achievement of emission- and color-stable IP-NCs enables new uses of this material. The sizes of the SLNs are sufficiently small to allow water-based ink-printing for optoelectronics or anti-counterfeiting applications, as nozzle diameters are typically of a few tens of micrometers. [174] For bio-imaging purposes, further efforts should be carried out to decrease the sizes of the platelet lipid structures. To induce cellular response, a nanomaterial should be smaller than 100 nm, although each material has its own effective size range, depending on the bio-application. [175] One way to further reduce the SLN size, could be by changing the surfactant type and the initial NCs concentration.

7.5 Conclusions

Long-term emission and color stability have been demonstrated for colloidal IP-NCs dispersed in Milli-Q water. These properties have been achieved by encapsulation of IP-NCs within SLNs of stearic acid. In that way, an easy-to-handle material, with a non-toxic carrier and free from organic solvents, has been obtained. With that, the potential applications of all-inorganic cesium lead halide IP-NCs are greatly increased; in particular, the preparation of water-based inks for jet-printing appears feasible.

8

Photon recycling in $CsPbBr_3$ nanocrystals

In this Chapter, photon recycling in $CsPbBr_3$ NCs is investigated. For this purpose, we make use of optical spectroscopy and investigate the spectral changes upon increasing the NC-NC distance (i.e. changing the colloid concentration) and changing the distance between excitation spot and emission window. Our experimental results are compared with the calculated prediction of emission intensity decay and red-shift, using the Beer-Lambert law. We observe a clear discrepancy between the experiment and the calculation, which we interpret as arising due to the presence of photon recycling in the NCs. In addition, we study the change of the PL lifetime as well as the absolute PL QY, by varying the concentration of NCs. We find a decrease of the PL lifetime by approximately a factor 4 and a decrease of ∼50% in the PL QY as the concentration increases ∼200 times. These results show that the excitation distribution in the colloid is no longer limited by the photon diffusion length, but can occur over longer distances through multiple reabsorption and re-emission events.

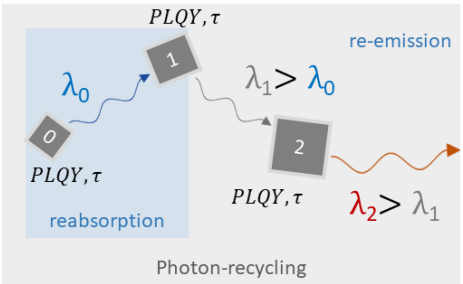

8.1 Introduction

Perovskite semiconductors have gained a major research impetus since 2009, when they were first applied in photovoltaic (PV) devices processed from solution inks. [176] With very recently reaching a conversion efficiency of 21.2%, these (hybrid) perovskite based PV materials are now directly competing with the mainstream multi-crystalline silicon cells. [177, 178] Since they can be conveniently deposited on a substrate by e.g. spin-coating and drop-casting forming thin layers, as we have seen in Chapter 5, they are also very suitable for large scale applications. Due to the recent demonstration of a non-degrading solar cell based on a thin layer with superior electrical properties containing $CsPbI_3$ NCs, they became a new candidate for the next generation of highly efficient PV. [15]

Recently, the phenomenon of "photon recycling" has been demonstrated in a $MAPbI_3$ prototype perovskite solar cell. [179] Photon recycling is the occurrence of subsequent reabsorption and re-emission events in a material. The authors of Ref. [179] observed light emission $\geqslant$50 μm away from the excitation spot. This is a much larger than distance that can be achieved by carrier diffusion in this material, and appears due to efficient photon recycling. The necessary requirements are: high radiative and low non-radiative recombination rates, a spectral overlap between absorption and PL and a high PL QY, which are met in IP-NCs. Due to their beneficial optical characteristics and improved stability, the IP-NCs are an excellent replacement for the hybrid perovskite materials bringing the phenomenon of photon recycling to the next level. Moreover, it can be expected that photon recycling effect will be enhanced in IP-NC ensembles due to the increased absorption cross-section. Interestingly, in this case the related excitation transfer will be "directed", from smaller towards larger NCs.

8.2 Synthesis and experimental setup

We have chosen to study photon recycling in $CsPbBr_3$ NCs because these are characterized by the highest PL QY of the three halide compositions (a necessary requirement for photon recycling). The NCs were synthesized following the protocol described in Ref. [5]. Figure 8.1a shows the NCs under UV lamp illumination, demonstrating a bright green PL. The corresponding ADF-STEM image is shown in figure 8.1b. A PL QY of 90% has been measured at an excitation wavelength of λ_{exc} = 430 nm. Figure 8.1c shows a clear overlap between the PL maximum and the absorption onset, which indicates that reabsorption and re-emission are feasible in this system.

As we have seen in Chapter 6, the PL spectrum of the NCs red-shifts as the concentration is increased. This is a result of reabsorption which becomes more probable and/or an energy transfer. We will first study the red-shift while varying two parameters: (i) the IP-NCs concentration and (ii) the distance d between the excitation spot and the PL collection spot. In the latter case, the maximum distance between excitation and collection is fixed. This is schematically shown in figure 8.2. The excitation light is guided through a pinhole to reduce the excitation spot diameter to 0.5 mm. As such, d can be varied between 0.5 - 9.5 mm, by moving the cuvette (10 mm width) in the y-direction. Photons (emitted by the NCs) propagating through the material can be scattered out of the cuvette, or be reabsorbed and re-emitted isotropically. We measured the emission at a 90° angle,

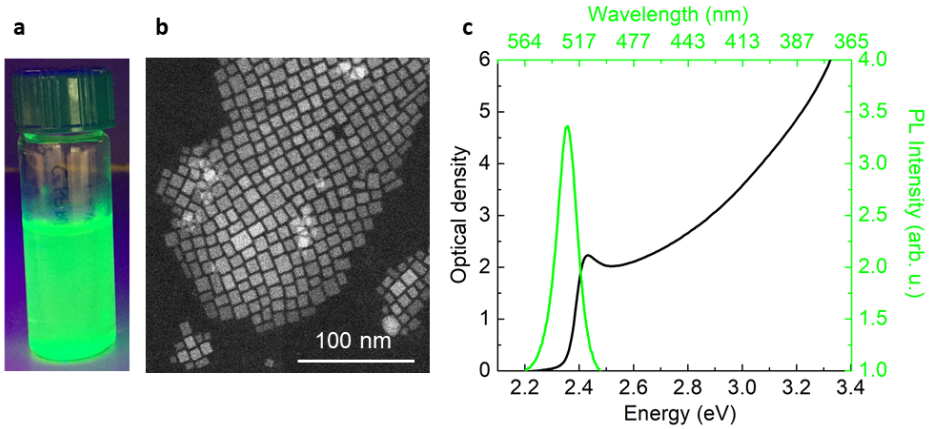

Figure 8.1: Optical characterization. (a) The sample illuminated by a UV lamp (λ_{exc} = 365 nm). (b) STEM image of fresh drop-casted $CsPbBr_3$ NCs, revealing an average size of 10.2 $\pm$ 1.8 nm. (c) PL (green) and optical density (black) showing the overlap between the PL maximum and the absorption onset.

being guided through a set of lenses onto the fiber coupler. In this configuration, we have detected no significant loss of PL intensity upon varying d. In this work, we used a diluted sample such that no reabsorption takes place, and compared the PL spectra for minimal and maximum d and found them to be identical within the experimental error.

We can expect that effective reabsorption within the NC ensemble will induce a red spectral shift in the measured PL, whose magnitude should increase with the NC concentration as well as with increasing d. The latter, because more re-emission events can take place, as the photons will have to propagate over a larger distance through the sample. At the same time, the PL spectrum will become asymmetric as the recycling proceeds from small to large NCs, like we have seen for ET - see Chapter 6.

8.3 Results: photon recycling

Our results are summarized in figure 8.3. To clearly monitor the spectral shift and their (asymmetric) shape, all PL spectra are normalized (we will study the decay in intensity of the PL in the next paragraph). Panels a-c show the emission for different concentrations of the colloids, ranging from 'as-prepared' up to 200 times diluted. For a small d (1 mm, panel a), we observe merely a minor red-shift upon increasing concentration. The red-shift becomes more pronounced, however, if d is increased to 5 mm (panel b). Both features, red-shift and spectral asymmetry, are clearly observed for d = 9 mm (panel c). To demonstrate that the observed spectral features are due to photon recycling, the experimental results are compared with the Beer-Lambert prediction, as shown in

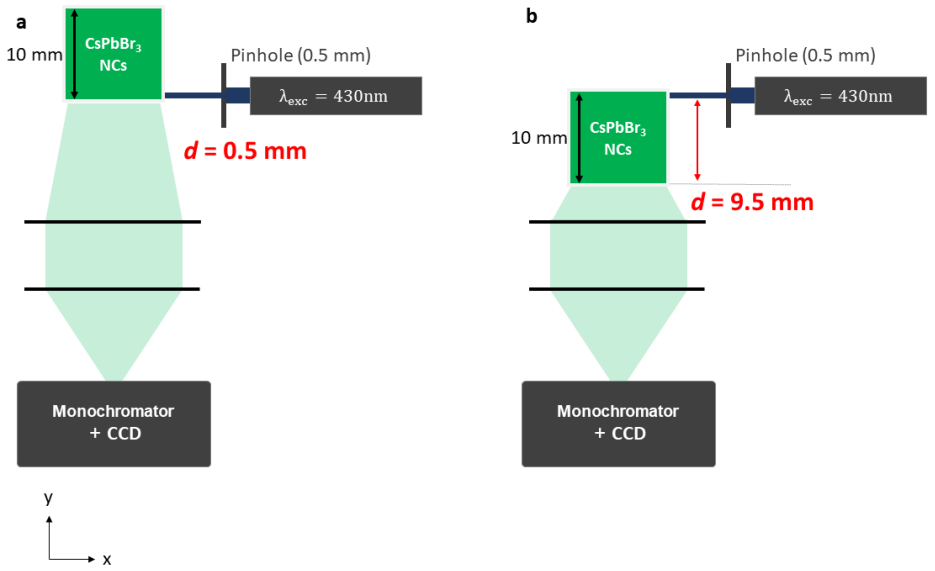

Figure 8.2: Schematics of the experimental setup. The cuvette is excited while maintaining a 90° angle between excitation (λ_{exc} = 430 nm) and collection (by the CCD) to avoid detecting the excitation pulse directly. The cuvette is mounted on a movable stage, such that the distance d i.e. the distance between excitation and emission window, can be varied between 0.5 mm (a) and 9.5 mm (b) by moving the cuvette in the y-direction. The maximum distance between excitation and collection is fixed.

panel d. This prediction is calculated using the intrinsic PL spectrum i.e., free from reabsorption (as measured for a very diluted colloid) and applying the Beer-Lambert law (as we have seen in Chapter 6) but rearranged (see the Appendix for details) to indicate the decay in spectral photon population, away from the excitation spot, which changes with distance d:

$$I^0(\lambda) = \frac{I(\lambda)}{e^{-\alpha(\lambda)d}} \tag{8.1}$$

where $I^0(\lambda)$ is the reabsorption-free spectrum, $I(\lambda)$ is the experimentally detected emission and $\alpha(\lambda)$ is the absorption coefficient. We can clearly see a considerable discrepancy between the experimentally obtained spectral red-shift and asymmetry (induced by varying d), and the Beer-Lambert prediction. This indicates that only taking into account reabsorption is not sufficient to describe the experimentally observed features and that additional processes, i.e. re-emission, have to be considered to explain the differences - which evidences the presence of photon recycling. In addition, we note that the described features, related to photon recycling, are absent in the most diluted sample (red spectrum) which yields the intrinsic PL spectrum, as was anticipated.

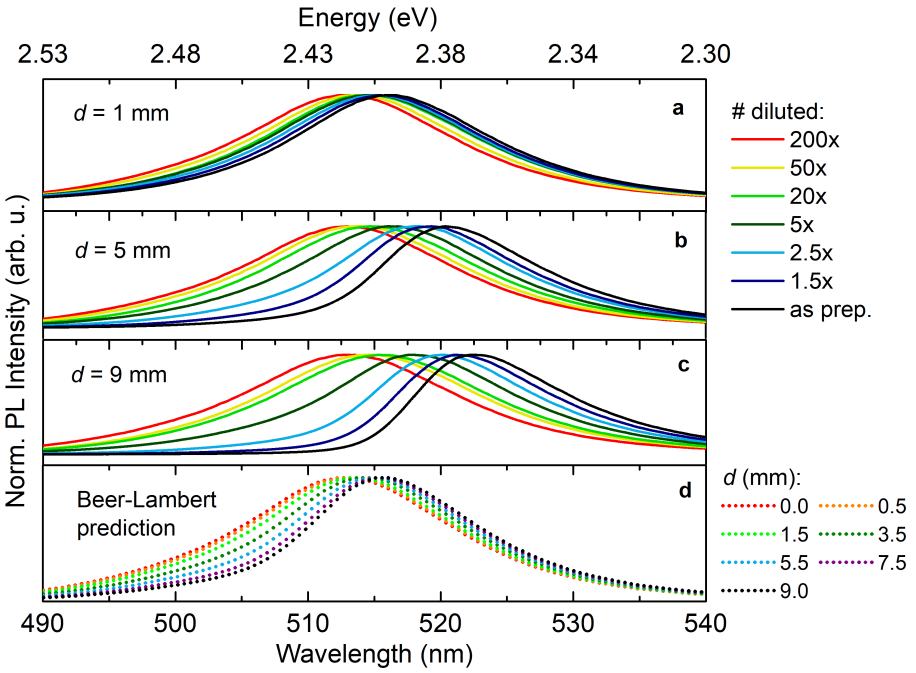

Figure 8.3: The spectral changes induced by photon recycling. (a-c) Normalized PL spectra, varying d between 1 - 9 mm. (d) The Beer-Lambert prediction (normalized) where a discrepancy between the experimentally obtained spectra and the calculated prediction is clearly observed. This indicates that taking merely reabsorption into account does not explain the observed red-shift and spectral changes. Note that experimental results for d = 0 mm represent the intrinsic, i.e., reabsorption-free PL spectrum.

8.4 Photoluminescence intensity decay

To study the photon recycling in more detail, we will now focus on one specific sample (1 times diluted) and compare the decay of the PL intensity as a function of d with the Beer-Lambert prediction. This is shown in figure 8.4a, where the measured and calculated spectra are given in the upper and lower panel respectively. It can be clearly seen, that the experimental decay is substantially slower than the prediction from the Beer-Lambert law.

To illustrate the difference in detail, figure 8.4b shows the PL intensity decay at three specific energies (2.38, 2.4 and 2.42 eV) comparing the experiment (solid lines) and the calculation (dotted lines) and demonstrating a clear difference between the two. In addition, figure 8.4c shows the integrated PL intensity for each value of the distance d, with the orange circles and pink stars corresponding to the experiment and the Beer-Lambert prediction, respectively: the decay of the former is clearly slower. These results shows that only taking into account reabsorption does not

explain the observed slower decay, and suggests the presence of photon recycling. We note that the Beer-Lambert prediction does not take into account any scattering effects, which would additionally decrease the predicted decay rate (slightly). Furthermore, the PL maximum red-shift is summarized in figure 8.4d, where the triangles represent the experiment and the squares the calculation. Here, we see an enhanced red-shift for the experimentally obtained PL maxima as compared to the calculation, which again suggests the presence of photon recycling.

Finally, we study how the PL lifetime changes as the concentration of the NCs solution is varied. Figure 8.4e shows the results for different dilutions of the colloid. The transients could be fitted with a double exponential function, where only t_1 - exhibiting an amplitude of a factor 10 larger than t_2 - is shown in figure 8.4e. As the NCs concentration increases, i.e. the NC-NC distance decreases, the lifetime becomes longer by approximately a factor 4. This result is in agreement with our previous observations, and consistent with the presence of photon recycling. In addition, we have determined the PL QY as a function of the NCs concentration. We have repeatedly observed a 50% drop of the absolute QY comparing the as-prepared colloid with the one diluted up to 200 times, which is expected if photon recycling takes place. Each time a NC (re-)emits a photon, it does so with its intrinsic QY. Therefore, with each recycling event, the observed PL QY decreases.

Furthermore we are currently working on a theoretical model to simulate and reproduce our experiments. The purpose is to demonstrate that the most important observable spectral changes - i.e., the spectral red-shift, the PL QY and the time-resolved PL - are indeed due to photon recycling and not to, e.g., solely reabsorption and scattering effects. At this moment, our simulation cannot incorporate the size distribution of the NCs; the available computational resources are not sufficient to process the large amount of data our model currently requires. However, reducing the calculation-time by taking into account a single NC size and assuming the system is in equilibrium, we reproduced a spectral red-shift upon increasing d. Subsequently, the PL QY can be extracted as the 'photon rate' at a specific energy - still depending on d - and is directly coupled to the intrinsic PL lifetime of the NC. This showed that the photon rate, i.e., PL QY decreases (resulting in the increase of the PL lifetime) if photon recycling is enabled. In future, we will be working towards reducing the complexity of the calculation to fully reproduce and confirm our experimental findings.

8.5 Conclusions

We have investigated photon recycling in $CsPbBr_3$ NCs using various optical spectroscopy measurements. A dedicated experiment, where the distance d between the excitation and PL collection spot is varied, revealed a clear discrepancy between the experimentally observed PL spectra and the Beer-Lambert prediction. We observed (i) a slower decay of the PL intensity and (ii) a more pronounced red-shift of PL spectra, with increasing distance d for the experimentally obtained data as compared to the calculation, and (iii) a more pronounced red-shift and spectral asymmetry upon increasing the NCs concentration. These discrepancies between the experiment and the Beer-Lambert calculation indicate that taking into account solely the reabsorption of the emitted photons it is not sufficient. This suggests that the participation of additional processes, and specifically re-emission, have to be considered in order to explain the experimental findings and evidences the occurrence of photon recycling. The important role of photon recycling is further corroborated by our observation

of a significant increase of the PL lifetime as the NC-NC distance becomes shorter as well as a 50% decrease of the PL QY.

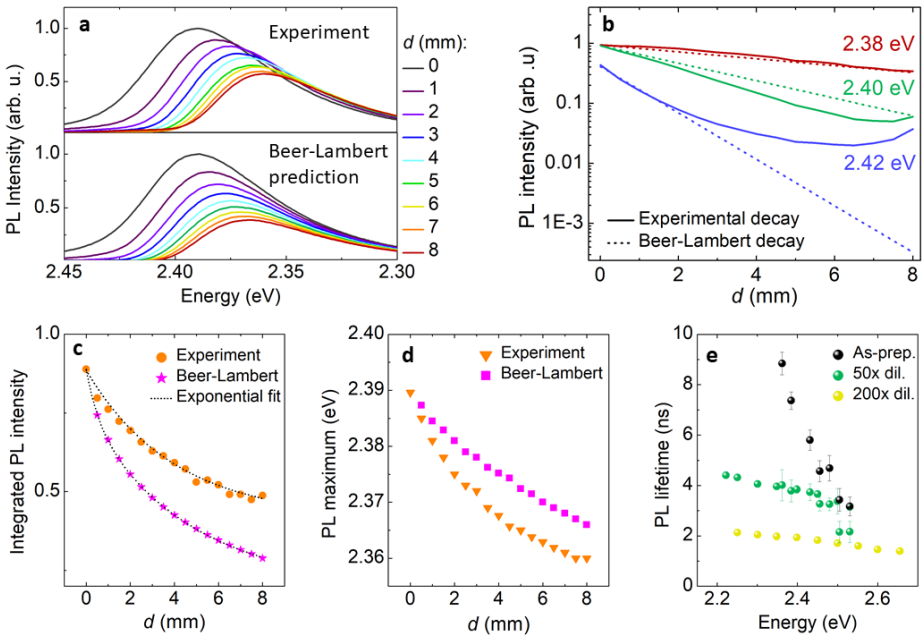

Figure 8.4: Results of the (time-resolved) PL experiments. (a) Comparison between the experimentally obtained PL spectra (top panel) and the Beer-Lambert calculation (botom panel), a clear discrepancy is observed. (b) The decay in PL intensity as a function of d at 2.38 eV (red), 2.40 eV (green and 2.42 eV (blue)) where the solid and dotted lines represent the experiment and the calculation, respectively. The difference between the experimental (circles) and predicted (stars) decay can be clearly observed. (c) The integrated PL intensity for all spectra as shown in (a) for each value of d. The predicted decay is much faster. Both curves have been fitted with a single exponential function (dotted lines). (d) The PL maxima obtained from the measured (triangles) and calculated (squares) spectra as shown in (a). A more pronounced red-shift is observed in the experiment. (e) PL lifetimes (E_{exc} = 2.6 eV, 470 nm), becoming slower as the concentration of the NCs in increases. All results shown here, especially the discrepancy between the Beer-Lambert prediction and the experiment, evidence photon recycling.

9

Outlook: Application perspective on all-inorganic perovskite nanocrystals

The attractive optical properties of IP-NCs identify them as a very interesting, novel photoelectric material. They have great potential for a wide variety of optoelectronic and photonic applications, such as in light emitting devices, for full-color full-size and micro-displays, photodetectors, solar cells, and lasers - cw as well as pulse operated. In this Chapter, some of the possible applications which recently have been explored are reviewed and summarized.

9.1 QLEDs

The very narrow and fully tunable emission bands render IP NCs very suitable for development of a new generation of quantum light emitting diodes (QLEDs), both mono-color and white light. Here, one important advantage is the possibility to realize narrow emission in red, not available with the commonly used (RE-based) phosphors. This allows for superior color rendering and higher efficiency, also for light-based medical treatment purposes. To this end, it is worth pointing out that the unique possibility of "double" color tuning of IP-NCs by size and composition, allows achieving ultra-narrow emission bands by resorting to large NCs. In that way, the size dependence of the emission wavelength is mitigated [16] and the effects of line-width broadening due to the (unavoidable for NCs) size distribution is arrested. For QLED applications, IP-NCs need to be stabilized against ion exchange which can be achieved by embedding, typically in polymers. Also alternative possibilities - such as exposure to X-rays - are being successfully explored. [180] Further, it has been shown that sufficient resistance to moisture and also the increased thermal stability of IP NCs - features typically required for phosphors in light-emitting applications - can be achieved by appropriate coating (e.g. with alkyl phosphate for $CsPbBr_3$ NCs). [181] In the meantime, also the first devices have been successfully demonstrated, featuring appreciable external quantum efficiencies, in excess of 6%. [182] A particularly bright and narrow band emitting device has been obtained by additional treatment of the layer of $CsPbBr_3$ NCs with CsBr. [183] Remarkably, this procedure not only increased the emissivity (by nearly two orders of magnitude) but improved also the stability of the device, which exhibited no degradation for at least 15 hrs under a continuous driving current. The latter has been assigned to the reduced resistance of the film, and the consequent lower joule heating during operation.

9.2 Lasing

Also IP-NCs-based lasers have been demonstrated. Indeed, stimulated emission and lasing from IP-NCs have been reported and postulated to originate from a bi-exciton state, promoted by its relatively large binding energy, of 50 meV. [184] Low-threshold amplified spontaneous emission and lasing from the layers of IP-NCs have been observed under optical pumping for all the halides and their mixtures, in the form of random lasing in films and from coatings in silica micro-spheres serving as the whispering gallery mode cavities. [185] Recently, also a prototype of a hybrid vertical cavity surface emitting laser, featuring a $CsPbBr_3$ thin film and a cavity formed by two distributed Bragg reflectors, has been demonstrated. [186] This device was characterized by an ultralow lasing threshold (<0.4 $\mu J/cm^2$) and a superior operation stability, thus confirming the potential of IP-NCs for the development of highly reliable lasers for femtosecond pulse as well as quasi-continuous-wave (nanosecond) operation.

9.3 Photovoltaics

Another important field where IP-NCs are expected to exert a large impact, is that of PV. This has been directly confirmed by the first demonstration of a working device with an active layer of

$CsPbI_3$ NCs. [42] It has been shown that thin films of IP-NCs feature sufficient thermal and temporal stability as required for PV devices, yielding $\sim$10% conversion efficiency. These could find application in single junction solar cells and also for the top cell in tandem devices. [40,187] By subsequent advances in surface chemistry, based on A-site cation halide salt treatment, the conductivity of $CsPbI_3$ NC layers could be improved, increasing the efficiency to the record level of 13.43%. [15] A somewhat different but also very interesting recent development in solar applications of IP-NCs, has been connected to the event of successful doping of IP-NCs. Doped IP-NCs could be used for light harvesting and conversion in solar concentrators (transition metal doping) [14] and also for light down- and up-conversion layers (rare-earth doping). [188] Finally, it should be mentioned that also electronic applications of IP-NCs are being explored, and a prototype flexible non-volatile memory device with resistive switching has been reported recently. [13]

10

Comparison of the optical properties of graphene and alkyl-terminated Si and Ge nanocrystals

Group IV semiconductor NCs serve as an alternative to commonly used direct band gap materials containing toxic and/or rare elements. In this Chapter, we investigate optical properties of butyl-terminated Si and Ge NCs and compare them to those of graphene NCs, finding them remarkably similar. We study their time-resolved PL emission as well as the PL excitation and linear absorption spectra. We contemplate that their emission characteristics indicate a (semi-)resonant activation of the emitting channel; the PL excitation shows characteristics similar to those of a molecule. The optical density is consistent with band-to-band absorption processes originating from core-related states. Hence, these observations strongly indicate a different microscopic origin for absorption and radiative recombination.

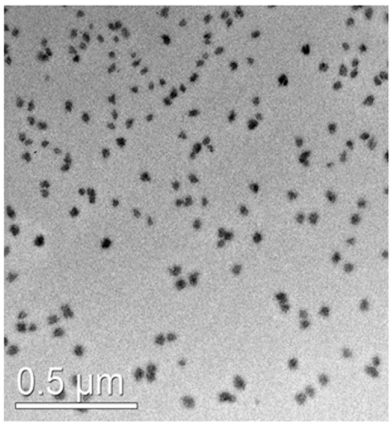

10.1 Introduction

Group IV semiconductors (i.e. Si, Ge and C) are characterized by large abundance, chemical and structural stability and low toxicity. However, their optical properties are inferior to those of II-VI and III-V semiconductor NCs (e.g. CdSe, CdTe, PbSe and InAs). Even though Si NCs have been reported to exhibit high PL QYs, [189] their external quantum efficiency (EQE, i.e. the ratio between the number of incident photons and the collected photocarriers) is often not sufficient for implementation in optical devices [190]. It is possible to enhance the optical activity of Si NCs by passivating the surface with e.g. oxygen, hydrogen or carbon. [191, 192] In particular, capping the surface with aliphatic carbon chains has been reported to have a dramatic effect on the optical properties of group IV semiconductor NCs. For example, 1-octadecene capped Ge NCs show tunable PL in the infrared region with a QY of 8% [193] where the typical values for bare Ge NCs are generally around 1%. Furthermore, tunable PL in the visible region with lifetimes of the order of nanoseconds has been reported for free-standing alkyl-terminated Si NCs, [194–196] which differs greatly from the infrared emission with μs lifetimes typically observed for oxygen passivated Si NCs. In addition, carbon dots and graphene NCs became interesting due to their high PL QYs, large absorptivity, fast radiative decay and tunable visible PL. [197] Shen *et al.* reported a PL efficiency of 28% for graphene NCs synthesized from graphene oxide sheets, showing emission in blue-green. [198] Another approach was followed by Gu *et al.* who synthesized graphene NCs using glucose as precursor material, and showed strong green PL with a QY of 44.3%. [199] Another and easy way to tune the graphene NCs band gap is through doping. A high PL QY of 49.8% is reported by Kharangarh *et al.* for nitrogen doped graphene NCs with blue-green emission. [200] Furthermore, it has been reported that band gap of graphene NCs is modified by changing the surface chemistry (and NC size) which determines their optical properties. [201] Although much research focused on explaining the origin of the PL and absorption mechanism in alkyl-terminated Si and Ge NCs [202] and in graphene NCs [203] comparative studies on these materials are lacking. In this study, we investigate the optical properties of butyl-terminated Si (C-Si) and Ge NCs (C-Ge) and compare them to those of graphene NCs.

10.2 Synthesis and optical characterization

The C-Si and C-Ge NCs were synthesized via a wet-chemical method [195, 196, 204] adapted from Yang *et al.* (see the Appendix for detailed information). [205] Briefly; magnesium silicide (Mg_2Si) was oxidized with bromine (Br_2) in refluxing n-octane for 60 hours. Bromo-octanes which form as a major side product are removed by efficient evaporation and fresh n-octane is added to the reaction. Formed bromine-terminated Si-NCs were subsequently passivated using n-butyllithium, replacing the bromine and resulting in n-butyl-terminated Si NCs. To prepare butyl-terminated Ge NCs, Mg_2Ge was used instead of Mg_2Si while the same method and materials were handled as described for preparing the butyl-terminated Si NCs. Even though several steps are performed to remove any unreacted bromine from the samples, our energy dispersive X-ray (EDX) analysis reveals residuals of Br nanoparticles. Other than Br, no evidence of any remaining side product(s) such as an excess of C or Mg was observed. According to Fourier Transform Infrared Spectroscopy

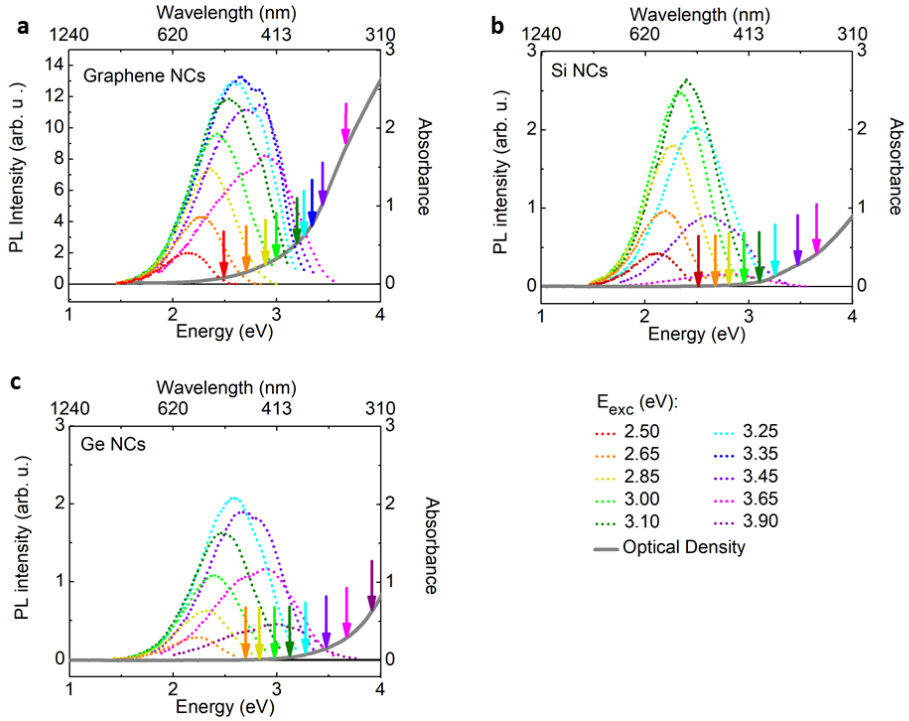

Figure 10.1: Photoluminescence excitation and optical density. Tunable PL emission (left axis) obtained for different excitation energies ranging between 2.5 - 3.9 eV for (a) Graphene NCs and butyl-terminated (b) Si and (c) Ge NCs. In all graphs, the optical density is indicated by the gray solid line (right axis). The colored arrows indicate the different position of excitation energy.

(FTIR) analysis performed on n-butyl-terminated Si nanoparticles prepared in n-octane, [206] CH_2 and CH_3 groups are also present on their surface protecting the Si core against oxidation because the Si-O bond is weak in comparison. Furthermore, brominated octyl species have been observed on the surface of these C-Si NCs as a consequence of the reaction solvent bromination. [204]

The graphene NCs were prepared by the oxidative cleavage of graphene oxides (GOs) to introduce hydroxyl groups in the dots. Ultrasonication (sono-oxidation) is used to prepare the graphene NCs from GOs. After filtration, the graphene NCs solutions were purified (see also the Appendix for further details). The graphene NCs have a size distribution of a few tens of nanometers and according to XPS the graphene NCs are functionalized with hydroxyl, graphitic carbon, oxygenated carbon, and carboxylic acid groups. [60] All NCs used in this study were dispersed in UV-grade ethanol.

The NCs have been optically characterized and their absorbance and PL spectra at different excitation energies are compared in figure 10.1. The arrows indicate the actual excitation energy along

the absorption spectrum, in the same color as the corresponding emission spectra. All samples show tunable, visible, blue-green PL, where the PL intensity is increasing and decreasing with excitation energy. The optical density is steadily increasing with energy and does not exhibit an excitonic line at the onset, as expected for indirect band gap semiconductor NCs. In order to investigate the (radiative) recombination characteristics, the time-resolved PL signal was recorded for all three samples, using an excitation energy of 3.5 eV. The PL lifetimes are in the nanosecond range, as shown in figure 10.2a, and comparable (5-6 ns, black and blue respectively) for the graphene and C-Ge NCs, and 3-3.5 ns for the C-Si NCs. In the same graph, the normalized PL spectra are included (dotted lines) for the same excitation energy of 3.5 eV. It is remarkable how similar the PL spectra for the different NCs are, the maxima being at roughly the same position. Time-resolved PL transients detected at 2.8 eV for the three types of NCs investigated here, are shown in figure 10.2b. The inset remarks the similarity between the C-Ge and graphene NCs. The total decay had to be fitted with a contribution of three exponents in the range of, respectively, ps, ns and tens of ns. In all cases the nanosecond component dominates (i.e. its amplitude is at least a factor 100 larger than that of the other two). Finally, figure 10.2c shows the absolute PL QY as a function of excitation energy, for all three samples (same colors as Figure. 2). A QY of 5.5% is measured for the graphene and C-Si NCs, where a lower value of 1% was measured for C-Ge NCs, in accordance with values reported in literature. [48, 207, 208] The QY dependence on excitation energy shows in all three cases a maximum, for the graphene and C-Si NCs around 2.8-3 eV and for the C-Ge NCs around 3.2 eV.

10.3 Discussion

The observed optical properties of all three NC materials are very similar. Their optical density shows a gradual increase with excitation energy, as is expected for an ensemble of (indirect band gap) NCs. This suggests that band-to-band absorption by core-related states is responsible (the increment is governed by the increase in the density of states further away from the band edges). For the graphene NCs, the onset in absorption takes place at lower energies, indicating a smaller band gap. In contrast, the PLE characteristics indicate the presence of a variety/ensemble of emitters that are excited resonantly, giving rise to the increasing and decreasing trend of the PL intensity (with increasing excitation energy) as is typically observed for molecules. In our materials, this can be described by the presence of surface moieties introducing localized states on the NC surface. A surface passivating molecule can, in general, have a boosting or quenching effect on the PL of a NC, depending on the position of the surface states with respect to the NC band gap. This has been observed for CdTe and CdSe NCs capped with thiol groups [209] and can be explained by the position of the top of the valence band of the NC with respect to the HOMO/LUMO energy levels of the molecule. If the HOMO (LUMO) level is placed above (below) the top (bottom) of the valence (conduction) band of the NC, this can cause trapping of a hole (electron) upon excitation of an electron-hole pair. The segregation of one carrier species on localized states on the surface of a NC will decrease the electron-hole wave functions overlap, resulting in a strongly reduced radiative efficiency. As the band gap energy of the NC increases with decreasing size, the efficiency of carrier trapping on the surface may increase, therefore decreasing the NC PL intensity. This is clearly in contrast with what is expected for a NC ensemble, where the NC is the only emitter. In that case, the

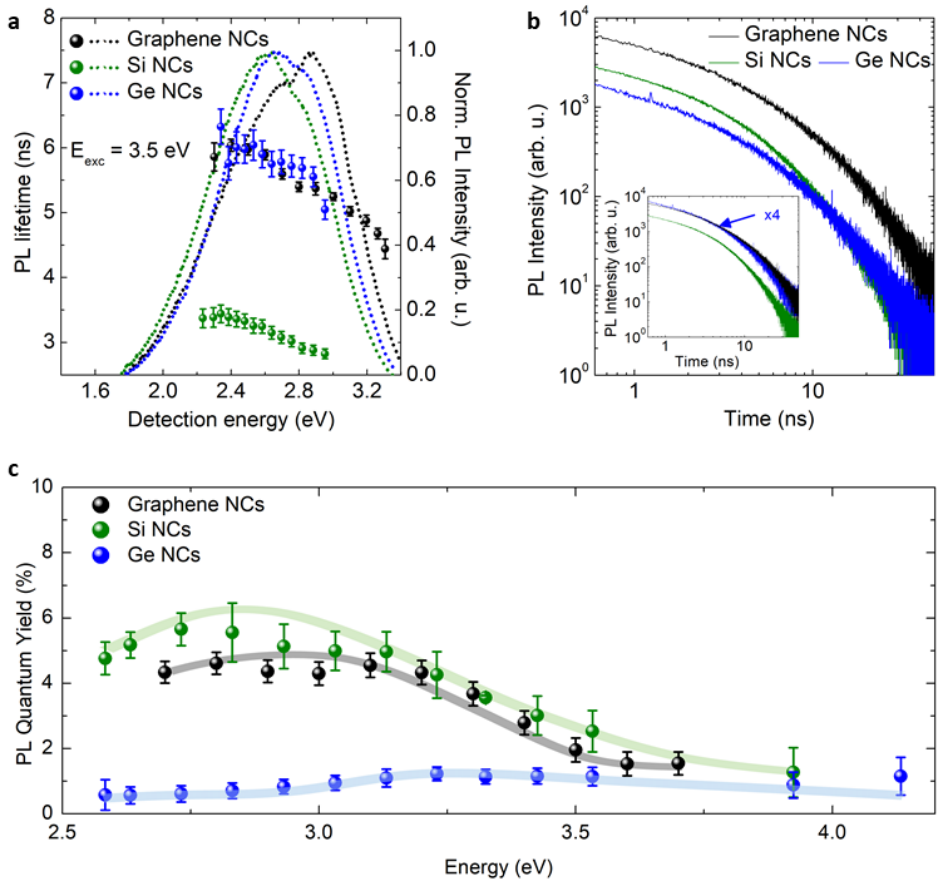

Figure 10.2: (a) The nanosecond PL lifetimes for the graphene NCs (black) and C-Si (green) and C-Ge (blue) NCs, as a function of detection energy (2.2 - 3.3 eV). The excitation energy is 3.5 eV. As expected, due to QC, a decreasing trend of the PL lifetime is observed for increasing detection energy for all three samples. The normalized PL spectra for the same excitation energy (3.5 eV) are indicated by the dotted lines (same colors). (b) Time-resolved PL signal at E_{det}=2.8 eV. The inset shows the transient of the C-Ge NCs multiplied by 4, to illustrate the similarity in decay with the graphene NCs. (c) The absolute PL QY as a function of energy for the graphene (black), C-Si (green) and C-Ge (blue) NCs. A QY of $\sim$5.5% is observed for the graphene and the C-Si NCs, but that of the C-Ge NCs is much lower ($\sim$1%). All data points follow the same increasing and decreasing trend with excitation energy. The error bars represent the statistical error caused by fluctuations of the lamp intensity used as an excitation source.

resulting PLE should follow an ongoing increase in PL intensity upon increasing excitation energy.

The optical density behaves as is expected for a NC ensemble with a size distribution, whereas the PL and PLE do not, indicating that the origin of the two processes differ at the microscopic level. Another feature that should be noted, is the appearance of a double-peak in the PL spectra at high (3.45 - 3.9 eV) excitation energies for the graphene and C-Ge NCs. In graphene NCs, the origin of a double-peak in the PLE is explained by the presence of conjugated π-domains, where the - (HOMO-LUMO) and - transitions give rise to the distinctive PL peaks. [203] As for the PL decay characteristics, all the NC materials investigated here show a similar behavior, featuring nanosecond lifetimes, which are too short to originate from the core-related (excitonic) emission, as generally observed and expected for indirect band gap semiconductor NCs. This is, however, consistent with the observations for the PLE and can therefore be related to the surface states.

We find that the absolute QY of all the NC materials is quite low ($<6\%$). This is explained by the presence of a strong non-radiative recombination channel and/or energy transfer, which is favored over radiative recombination, and therefore, quenching the PL QY. [131, 158] The presence of non-radiative channels influences the (mono)exponential decay such that it becomes multi- or non-exponential, in agreement with our observations for the time-resolved PL. It is striking that we find evidence of the presence of Br nanoparticles in the C-Si and C-Ge NC samples. However, Br nanoparticles are not optically active. Moreover, the observed excitation dependent PL emission, agrees very well with that of alkyl terminated Si NCs, [194–196] and the measured optical density is the characteristic of indirect band gap semiconductor particles. Therefore, this leads us to conclude that the observed emission and absorption spectra originate most probably from the C-Si and C-Ge NCs.

10.4 Conclusions

For all three types of NCs, the observed characteristics of the PL/PLE are strikingly similar, which indicates that the microscopic origin of radiative recombination for C-Si, C-Ge and graphene NCs is likely to be similar. The emission characteristics indicate (semi-)resonant activation of the emitting channel, since the PL resembles emission characteristics of a molecule. The absorption characteristics are identical in all three materials, and can be related to band-to-band absorption processes in the NC core. Based on these observations, we postulate that the presence of carbon moieties on the surface are responsible for the similar PL mechanism observed in all three materials.

References

[1] H. Huang, M.I. Bodnarchuk, S.V. Kershaw, M.V. Kovalenko, and A.L. Rogach. Lead halide perovskite nanocrystals in the research spotlight: Stability and defect tolerance. *ACS Energy Lett.*, 2:2071–2083, 2017.

[2] T.C. Sum and N. Mathews. Advancements in perovskite solar cells: photophysics behind the photovoltaics. *Energy Environ. Sci*, 7:2518–2534, 2014.

[3] S.D. Stranks, P.K. Nayak, W. Zhang, T. Stergiopoulos, and H.J. Snaith. Formation of thin films of organic-inorganic perovskites for high-efficiency solar cells. *Angew. Chem. Int. Ed.*, 54:3240–3248, 2015.

[4] W. Nie, H. Tsai, R. Asadpour, J.C. Blancon, A. Neukirch, G. Gupta, J.J. Crochet, M. Chhowalla, S. Tretiak, M.A. Alam, H.L., and Wang. High-efficiency solution-processed perovskite solar cells with millimeter-scale grains. *Science*, 347:522–525, 2015.

[5] L. Protesescu, S. Yakunin, M.I. Bodnarchuk, F. Kriegm, R. Caputo, C.H. Hendon, R.X. Yang, A. Walsh, and M.V. Kovalenko. Nanocrystals of cesium lead halide perovskites ($CsPbX_3$, X = Cl, Br, and I): Novel optoelectronic materials showing bright emission with wide color gamut. *Nano Lett.*, 15:3692–3696, 2015.

[6] A. Swarnkar, R. Chulliyil, V.K. Ravi, M. Irfanullah, A. Chowdhury, and A. Nag. Colloidal $CsPbBr_3$ perovskite nanocrystals: luminescence beyond traditional quantum dots. *Angewandte Chemie*, 127:15644–15648, 2015.

[7] Q.A. Akkerman, V. D´Innocenzo, S. Accornero, A. Scarpellini, A. Petrozza, M. Prato, and L. Manna. Tuning the optical properties of cesium lead halide perovskite nanocrystals by anion exchange reactions. *J. Am. Chem. Soc.*, 137:10276–10281, 2015.

[8] J. Bisquert. The swift surge of perovskite photovoltaics. *J. Phys. Chem. Lett.*, 4:2597–2598, 2013.

[9] S. Kazim, M.K. Nazeeruddin, M. Grätzel, and S. Ahmad. Perovskite as light harvester: A game changer in photovoltaics. *Angew. Chem. Int. Ed.*, 53:2812–2824, 2014.

[10] M.A. Green, A. Ho-Baillie, and H.J. Snaith. The emergence of perovskite solar cells. *Nat. Photon.*, 8, 2014.

[11] M. Grätzel. The light and shade of perovskite solar cells. *Nat. Mater.*, 13:838, 2014.

[12] N-G. Park. Organometal perovskite light absorbers toward a 20% efficiency low-cost solid-state mesoscopic solar cell. *J. Phys. Chem. Lett.*, 4:2423–2429, 2013.

[13] D. Liu, Q. Lin, Z. Zang, M. Wang, P. Wangyang, X. Tang, M. Zhou, and W. Hu. Flexible all-inorganic perovskite $CsPbBr_3$ nonvolatile memory device. *ACS Appl. Mater. Int.*, 9:6171–6176, 2017.

[14] F. Meinardi, Q.A. Akkerman, F. Bruni, S. Park, M. Mauri, Z. Dang, L. Manna, and S. Brovelli. Doped halide perovskite nanocrystals for reabsorption-free luminescent solar concentrators. *ACS Energy Lett.*, 2:2368–2377, 2017.

[15] E.M. Sanehira, A.R. Marshall, J.A. Christians, S.P. Harvey, P.N. Ciesielski, L.M. Wheeler, P. Schulz, L.Y. Lin, M.C. Beard, and J.M. Luther. Enhanced mobility $CsPbI_3$ quantum dot arrays for record-efficiency, high-voltage photovoltaic cells. *Sci. Adv.*, 3:4204–4210, 2017.

[16] Y.H. Kim, C. Wolf, Y.T. Kim, H. Cho, W. Kwon, S. Do, A. Sadhanala, C.G. Park, S.W. Rhee, S.H. Im, and R.H. Friend. Highly efficient light-emitting diodes of colloidal metal-halide perovskite nanocrystals beyond quantum size. *ACS Nano*, 11:6586–6593, 2017.

[17] F. Palazon, Q.A. Akkerman, M. Prato, and L. Manna. X-ray lithography on perovskite nanocrystals films: From patterning with anion-exchange reactions to enhanced stability in air and water. *ACS Nano*, 10:1224–1230, 2016.

[18] G. Nedelcu, L. Protesescu, S. Yakunin, M.I. Bodnarchuk, M.J. Grotevent, and M.V. Kovalenko. Fast anion-exchange in highly luminescent nanocrystals of cesium lead halide perovskites ($CsPbBr_3$, X = Cl, Br, I). *Nano Lett.*, 15:5635–5640, 2015.

[19] Y. Wang, X. Li, X. Zhao, L. Xiao, H. Zeng, and H. Sun. Nonlinear absorption and low-threshold multi-photon pumped stimulated emission from all-inorganic perovskite nanocrystals. *Nano Lett.*, 16:448–453, 2016.

[20] S. Sun, D. Yuan, Y. Xu, A. Wang, and Z. Deng. Ligand-mediated synthesis of shape-controlled cesium lead halide perovskite nanocrystals via reprecipitation process at room temperature. *ACS Nano*, 10(3):3648–3657, 2016.

[21] X. Chen, L. Peng, K. Huang, Z. Shi, R. Xie, and W W. Yang. Non-injection gram-scale synthesis of cesium lead halide perovskite quantum dots with controllable size and composition. *Nano Res.*, 9:1994–2006, 2016.

[22] I. Lignos, S. Stavrakis, G. Nedelcu, L. Protesescu, A.J. deMello, and M.V. Kovalenko. Synthesis of cesium lead halide perovskite nanocrystals in a droplet-based microfluidic platform: fast parametric space mapping. *Nano Lett.*, 16:1869–1877, 2016.

[23] R.W. Epps, K.C. Felton, C.W. Coley, and M. Abolhasani. Automated microfluidic platform for systematic studies of colloidal perovskite nanocrystals: towards continuous nano-manufacturing. *Lab on a Chip*, 17:4040–4047, 2017.

[24] S. Ye, M. Yu, M. Zhao, J. Song, and J. Qu. Low temperature synthesis of high-quality all-inorganic cesium lead halide perovskite nanocrystals in open air and their upconversion luminescence. *J. Alloys Compd.*, 730:62–70, 2018.

[25] Q.A. Akkerman, M. Gandini, F. Di Stasio, P. Rastogi, F. Palazon, G. Bertoni, J.M. Ball, M. Prato, A. Petrozza, and L. Manna. Strongly emissive perovskite nanocrystal inks for high-voltage solar cells. *Nat. Energy*, 2:16194, 2017.

[26] S. Wei, Y. Yang, X. Yang, L. Wang, L. Huang, and D D. Pan. Room-temperature and gram-scale synthesis of $CsPbX_3$ (X= Cl, Br, I) perovskite nanocrystals with 50-85% photoluminescence quantum yields. *Chem. Comm.*, 52:7265–7268, 2016.

[27] T.C. Jellicoe, J.M. Richter, H.F. Glass, M. Tabachnyk, R. Brady, S.E. Dutton, A. Rao, R.H. Friend, D. Credgington, N.C. Greenham, and M.L. Böhm. Synthesis and optical properties of lead-free cesium tin halide perovskite nanocrystals. *J. Am. Chem. Soc.*, 138:2941–2944, 2016.

[28] M. Leng, Y. Yang, K. Zeng, Z. Chen, Z. Tan, S. Li, J. Li, B. Xu, D. Li, M.P. Hautzinger, and Y. Fu. All-inorganic bismuth-based perovskite quantum dots with bright blue photoluminescence and excellent stability. *Adv. Funct. Mater.*, 28:1704446–1704457, 2018.

[29] Q.A. Akkerman, G. Rain, M.V. Kovalenko, and L. Manna. Genesis, challenges and opportunities for colloidal lead halide perovskite nanocrystals. *Nat. Mater.*, doi:10.1038/s41563-018-0018-4, 2018.

[30] B.A. Koscher, J.K. Swabeck, N.D. Bronstein, and A.P. Alivisatos. Essentially trap-free $CsPbBr_3$ colloidal nanocrystals by postsynthetic thiocyanate surface treatment. *J. Am. Chem. Soc.*, 139:6566–6569, 2017.

[31] M.A. Becker, R. Vaxenburg, G. Nedelcu, P.C. Sercel, A. Shabaev, M.J. Mehl, J.G. Michopoulos, S.G. Lambrakos, N. Bernstein, J.L. Lyons, and T. Stferle. Bright triplet excitons in caesium lead halide perovskites. *Nature*, 553:189, 2018.

[32] M. Sakata, T. Nishiwaki, and J. Harada. Neutron diffraction study of the structure of cubic $CsPbBr_3$. *J. Phys. Soc. Jpn*, 47:232–233, 1979.

[33] C.K. Möller. Crystal structure and photoconductivity of caesium plumbohalides. *Nature*, 182:1436, 1958.

[34] F. Bertolotti, L. Protesescu, M.V. Kovalenko, S. Yakunin, A. Cervellino, S.J. Billinge, M.W. Terban, J.S. Pedersen, N. Masciocchi, and A. Guagliardi. Coherent nanotwins and dynamic disorder in cesium lead halide perovskite nanocrystals. *ACS Nano*, 11:3819–3831, 2017.

[35] M. Cola, V. Massarotti, R. Riccardi, and C. Sinistri. Binary systems formed by lead bromide with (Li, Na, K, Rb, Cs and Tl) Br, a DTA and diffractometric study. *Z. Naturforsch. A*, 26:1328–1332, 1971.

[36] R.X. Yang, J.M. Skelton, E.L. da Silva, J.M. Frost, and A. Walsh. Spontaneous octahedral tilting in the cubic inorganic cesium halide perovskites $CsSnX_3$ and $CsPbBr_3$ (X= F, Cl, Br, I). *J. Phys. Chem. Lett.*, 8:4720–4726, 2017.

[37] D. Zhang, S. W. Eaton, Y. Yu, L. Dou, and P. Yang. Solution-phase synthesis of cesium lead halide perovskite. *J. Am. Chem. Soc.*, 137:9230–9233, 2015.

[38] Y. Bekenstein, B. A. Koscher, S. W. Eaton, P. Yang, and A. P. Alivisatos. Highly luminescent colloidal nanoplates of perovskite cesium lead halide and their oriented assemblies. *J. Am. Chem. Soc.*, 137:16008–16011, 2015.

[39] P. Cottingham and R.L. Brutchey. On the crystal structure of colloidally prepared $CsPbBr_3$ quantum dots. *Chem. Comm.*, 52:5246–5249, 2016.

[40] R.E. Beal, D.J. Slotcavage, T. Leijtens, A.R. Bowring, R.A. Belisle, W.H. Nguyen, G.F. Burkhard, E.T. Hoke, and M.D. McGehee. Cesium lead halide perovskites with improved stability for tandem solar cells. *J. Phys. Chem. Lett.*, 7:746–751, 2016.

[41] W.J. Yin, Y. Yan, and S.H. Wei. Anomalous alloy properties in mixed halide perovskites. *J. Phys. Chem. Lett.*, 5:3625–3631, 2014.

[42] A. Swarnkar, A.R. Marshall, E.M. Sanehira, B.D. Chernomordik, D.T. Moore, J.A. Christians, T. Chakrabarti, and J.M. Luther. Quantum dot-induced phase stabilization of α-$CsPbI_3$ perovskite for high-efficiency photovoltaics. *Science*, 354:92–95, 2016.

[43] W. Shockley and H.J. Queisser. Detailed balance limit of efficiency of p-n junction solar cells. *J. Appl. Phys.*, 32:510–519, 1961.

[44] *http://nptel.ac.in/courses/115102025/4*.

[45] A.P. Alivisatos. Semiconductor clusters, nanocrystals and quantum dots. *Science*, 271:933–937, 1996.

[46] M. El Kurdi, G. Fishman, S. Sauvage, and P. Boucaud. Band structure and optical gain of tensile-strained germanium based on a 30 band k-p formalism. *J. Appl. Phys.*, 107:013710, 2010.

[47] T.K.P. Luong, V. Le Thanh, A. Ghrib, M. El Kurdi, and P. Boucaud. Making germanium, an indirect band gap semiconductor, suitable for light-emitting devices. *Adv. Nat. Sci.: Nanosci. Nanotechnol.*, 6:015013, 2015.

[48] Y. Kanemitsu, H. Uto, and Y. Masumoto. On the origin of visible photoluminescence in nanometer-size Ge crystallites. *Appl. Phys. Lett.*, 61(18):2187–2189, 1992.

[49] M. Zacharias and P. Fauchet. Blue luminescence in films containing Ge and GeO_2 nanocrystals: the role of defects. *Appl. Phys. Lett.*, 71:380–382, 1997.

[50] S. Okamoto and Y. Kanemitsu. Photoluminescence properties of surface-oxidized Ge nanocrystals: surface localization of excitons. *Phys. Rev. B*, 54:16421, 1996.

[51] Y. Kanemitsu. Mechanism of visible photoluminescence from oxidized silicon and germanium nanocrystallites. *Thin Solid Films*, 276:44–46, 1996.

[52] S. Takeoka, M. Fujii, S. Hayashi, and K. Yamamoto. Size-dependent near-infrared photoluminescence from Ge nanocrystals embedded in SiO_2 matrices. *Phys. Rev. B*, 58(12):7921–7925, 1998.

[53] S. Takeoka, M. Fujii, S. Hayashi, and K. Yamamoto. Decay dynamics of near-infrared photoluminescence from Ge nanocrystals. *Appl. Phys. Lett.*, 74(11):1588–1560, 1999.

[54] S. Saeed, C. de Weerd, P. Stallinga, F.C.M. Spoor, A.J. Houtepen, L.D.A. Siebbeles, and T. Gregorkiewicz. Carrier multiplication in germanium nanocrystals. *Light Sci. Appl.*, 4:e251, 2015.

[55] A.J. Nozik. Nanoscience and nanostructures for photovoltaics and solar fuels. *Nano Lett*, 10:2735–2741, 2010.

[56] *http://didagostino.blogspot.nl/p/blog-page.html*.

[57] B. Trauzettel D.V. Bulaev, D. Loss, and G. Burkard. Spin qubits in graphene quantum dots. *Nat. Phys.*, 3:192–196, 2007.

[58] M. Bacon, S.J. Bradley, and T. Nann. Graphene quantum dots. *Part. Part. Syst. Char.*, 31:415–428, 2014.

[59] Y. Shin, J. Park, D. Hyun, J. Yang, J.H. Lee, J.H. Kim, and H. Lee. Acid-free and oxone oxidant-assisted solvothermal synthesis of graphene quantum dots using various natural carbon materials as resources. *Nanoscale*, 7:5633–5637, 2015.

[60] Y. Shin, J. Park, D. Hyun, J. Yang, and H. Lee. Generation of graphene quantum dots by the oxidative cleavage of graphene oxide using the oxone oxidant. *New J. Chem.*, 39:2425–2428, 2015.

[61] J. Peng, W. Gao, B.K. Gupta, Z. Liu, R. Romero-Aburto, L. Ge, L. Song, L.B. Alemany, X. Zhan, G. Gao, and S.A. Vithayathil. Graphene quantum dots derived from carbon fibers. *Nano Lett.*, 12:844–849, 2012.

[62] D.B. Shinde and V.K. Pillai. Electrochemical preparation of luminescent graphene quantum dots from multiwalled carbon nanotubes. *Chem. Eur. J.*, 18:12522–12528, 2012.

[63] A.H. Castro Neto, F. Guinea, and N.M.R. Peres. Drawing conclusions from graphene. *Phys. World*, 19:11–34, 2006.

[64] J. Tauc. Electron impact ionization in semiconductors. *J. Phys. Chem. Sol.*, 8:219–223, 1959.

[65] K.G. McKay and A.B. McAfee. Electron multiplication in silicon and germanium. *Phys. Rev.*, 91:1079, 1953.

[66] J.E. Castle. *Practical surface analysis by Auger and X-ray photoelectron spectroscopy. In: Surface and Interface Analysis*, volume 6,302. John Wiley and Sons Ltd, Chichester, 1984.

[67] V.I. Klimov. Spectral and dynamical properties of multiexcitons in semiconductor nanocrystals. *Annu. Rev. Phys. Chem.*, 58:635–673, 2007.

[68] A.J. Nozik. Quantum dot solar cells. *Phys. E,*, 14:115–120, 2002.

[69] O.E. Semonin, J.M. Luther, S. Choi, H.Y. Chen, J. Gao, A.J. Nozik, and M.C. Beard. Peak external photocurrent quantum efficiency exceeding 100% via MEG in a quantum dot solar cell. *Science*, 334:1530–1533, 2011.

[70] M.C. Hanna, M.C. Beard, and A.J. Nozik. Effect of solar concentration on the thermodynamic power conversion efficiency of quantum-dot solar cells exhibiting multiple exciton generation. *J. Phys. Chem. Lett.*, 3:2857–2862, 2012.

[71] M.C. Beard, J.M. Luther, O.E. Semonin, and A.J. Nozik. Third generation photovoltaics based on multiple exciton generation in quantum confined semiconductors. *Acc. Chem. Res.*, 46:1252–1260, 2012.

[72] M.T. Trinh, A.J. Houtepen, J.M. Schins, T. Hanrath, J. Piris, W. Knulst, A.P.L.M. Goossens, and L.D.A. Siebbeles. In spite of recent doubts carrier multiplication does occur in PbSe nanocrystals. *Nano Lett.*, 8:1713–1718, 2008.

[73] M. Aerts, T. Bielewicz, C. Klinke, F.C. Grozema, A.J. Houtepen, and J.M. Schins amd L. D.A. Siebbeles. Highly efficient carrier multiplication in PbS nanosheets. *Nat. Commun.*, 5:3789–3794, 2014.

[74] G. Nair, S.M. Geyer, L.Y. Chang, and M.G. Bawendi. Carrier multiplication yields in PbS and PbSe nanocrystals measured by transient photoluminescence. *Phys. Rev. B*, 78:125325–125335, 2008.

[75] R.J. Ellingson, M.C. Beard, J.C. Johnson, P. Yu, O.I. Micic, A.J. Nozik, A. Shabaev, and A.L. Efros. Highly efficient multiple exciton generation in colloidal PbSe and PbS quantum dots. *Nano Lett.*, 5:865–871, 2005.

[76] G. Nair and M.G. Bawendi. Carrier multiplication yields of CdSe and CdTe nanocrystals by transient photoluminescence spectroscopy. *Phys. Rev. B*, 76:081304–081308, 2007.

[77] D. Timmerman, J. Valenta, K. Dohnalova, W.D.A.M. de Boer, and T. Gregorkiewicz. Step-like enhancement of luminescence quantum yield of silicon nanocrystals. *Nat. Nanotech.*, 6:710–713, 2011.

[78] J.W. Luo, A. Franceschetti, and A. Zunger. Carrier multiplication in semiconductor nanocrystals: Theoretical screening of candidate materials based on band-structure effects. *Nano Lett.*, 8:3174–3181, 2008.

[79] K.J. Tielrooij, J.C.W. Song, S.A. Jensen, A. Centeno, A. Pesquera, A. Zurutuza Elorza, M. Bonn, L.S. Levitov, and F.H.L. Koppens. Photoexcitation cascade and multiple hot-carrier generation in graphene. *Nat. Phys.*, 9:248–252, 2013.

[80] A. Kulkarni, W.H. Evers, S. Tomić, M.C. Beard, D. Vanmaekelbergh, and L.D.A. Siebbeles. Efficient step-like carrier multiplication in percolative networks of epitaxially connected PbSe nanocrystals. *ACS Nano*, 12:378–348, 2017.

[81] S.V. Kershaw and A.L. Rogach. Carrier multiplication mechanisms and competing processes in colloidal semiconductor nanostructures. *Mater.*, 10:1095, 2017.

[82] M.A. Leontiadou, C.T. Smith, C. Lydon, and D.J. Binks. *Charge dynamics in colloidal quantum dots: recombination, trapping and multiple exciton generation. In: Nanostructured Materials for Type III Photovoltaics.* RSC Nanoscience and Nanotechnology, 2017.

[83] C.T. Smith, M.A. Leontiadou, P.C.J. Clark, C. Lydon, N. Savjani, B.F. Spencer, W.R. Flavell, P. OBrien, and D.J. Binks. Multiple exciton generation and dynamics in InP/CdS colloidal quantum dots. *J. Phys. Chem. C*, 121:2099–2107, 2017.

[84] A. Al-Otaify, S.V. Kershaw, S. Gupta, A.L. Rogach, G. Allan, C. Delerue, and D.J. Binks. Multiple exciton generation and ultrafast exciton dynamics in HgTe colloidal quantum dots. *Phys. Chem. Chem. Phys.*, 15:16864–16873, 2013.

[85] D.J. Binks. Multiple exciton generation in nanocrystal quantum dots-controversy, current status and future prospects. *Phys. Chem. Chem. Phys.*, 13:12693–12704, 2011.

[86] S.K. Stubbs, S.J.O. Hardman, D.M. Graham, B.F. Spencer, W.R. Flavell, P. Glarvey, O. Masala, N.L. Pickett, and D.J. Binks. Efficient carrier multiplication in InP nanoparticles. *Phys. Rev. B*, 81:081303, 2010.

[87] C. Smith and D. Binks. Multiple exciton generation in colloidal nanocrystals. *Nanomater.*, 4:19–45, 2013.

[88] A. Manzi, Y. Tong, J. Feucht, E-P. Yao, L. Polavarapu, A.S. Urban, and J. Feldmann. Resonantly enhanced multiple exciton generation through below-band-gap multi-photon absorption in perovskite nanocrystals. *Nat. Commun.*, 9:1518, 2018.

[89] N.S. Makarov, S. Guo, O. Isaienko, W. Liu, I. Robel, and V.I. Klimov. Spectral and dynamical properties of single excitons, biexcitons, and trions in cesium-lead-halide perovskite quantum dots. *Nano Lett.*, 16:2349–2362, 2016.

[90] L.H. Tizei, Y.C. Lin, M. Mukai, H. Sawada, A.Y. Lu, L.J. Lia, K. Kimoto, and K. Suenaga. Exciton mapping at subwavelength scales in two-dimensional materials. *Phys. Rev. Lett.*, 114:107601, 2015.

[91] T. Sasaki, H. Sawada, F. Hosokawa, Y. Sato, and K. Suenaga. Aberration-corrected STEM/TEM imaging at 15kv. *Ultramicroscopy*, 145:5055, 2014.

[92] S. Morishita, M. Mukai, K. Suenaga, and H. Sawada. Atomic resolution imaging at an ultralow accelerating voltage by a monochromatic transmission electron microscope. *Phys. Rev. Lett.*, 117:153004, 2016.

[93] J. Lin, L. Gomez, C. de Weerd, Y. Fujiwara, T. Gregorkiewicz, and K. Suenaga. Direct observation of band structure modifications in nanocrystals of $CsPbBr_3$ perovskite. *Nano Lett.*, 16(11):7198–7202, 2016.

[94] R. Saran, A. Heuer-Jungemann, A.G. Kanaras, and R.J. Curry. Giant bandgap renormalization and exciton-phonon scattering in perovskite nanocrystals. *Adv. Opt. Mater.*, 5, 2017.

[95] R.D. Schaller, V.M. Agranovich, and V.I. Klimov. High-efficiency carrier multiplication through direct photogeneration of multi-excitons via virtual single-exciton states. *Nat. Phys.*, 1:189–194, 2005.

[96] R.D. Schaller, M. Sykora, J.M. Pietryga, and V.I. Klimov. Seven excitons at a cost of one: Redefining the limits for conversion efficiency of photons into charge carriers. *Nano Lett.*, 6:424–429, 2006.

[97] M.T. Trinh, R. Limpens, W.D.A.M. de Boer, J.M. Schins, L.D.A. Siebbeles, and T. Gregorkiewicz. Direct generation of multiple excitons in adjacent silicon nanocrystals revealed by induced absorption. *Nat. Photon.*, 6:316–322, 2012.

[98] M.C. Beard, K.P. Knutsen, P. Yu, J.M. Luther, Q. Song, W.K. Metzger, R.J. Ellingson, and A.J. Nozik. Multiple exciton generation in colloidal silicon nanocrystals. *Nano Lett.*, 7:2506–2512, 2007.

[99] M.C. Beard, A.G. Midgett, M. Law, O.E. Semonin, R.J. Ellingson, and A.J. Nozik. Variations in the quantum efficiency of multiple exciton generation for a series of chemically treated PbSe nanocrystal films. *Nano Lett.*, 9:836–845, 2009.

[100] E.M.L.D. de Jong, G. Yamashita, L. Gomez, M. Ashida Y. Fujiwara, and T. Gregorkiewicz. Multiexciton lifetime in all-inorganic $CsPbBr_3$ perovskite nanocrystals. *J. Phys. Chem. C.*, 121:1941–1947, 2017.

[101] M.C. Beard, A.G. Midgett, M.C. Hanna, J.M. Luther, B.K. Hughes, and A.J. Nozik. Comparing multiple exciton generation in quantum dots to impact ionization in bulk semiconductors: Implications for enhancement of solar energy conversion. *Nano Lett.*, 10:3019–3027, 2010.

[102] F.C.M. Spoor, S. Tomić, A.J. Houtepen, and L.D.A. Siebbeles. Broadband cooling spectra of hot electrons and holes in PbSe quantum dots. *ACS Nano*, 11:6286–6294, 2017.

[103] W.D.A.M. de Boer, T. Gregorkiewicz, H. Zhang, W.J. Buma, A.N. Poddubny, A.A. Prokofiev, and I.N Yassievich. Self-trapped exciton state in Si nanocrystals revealed by induced absorption. *Phys. Rev. B*, 85:1614091–1614095, 2012.

[104] E.M.L.D. de Jong, W.D.A.M. de Boer, I.N. Yassievich, and T. Gregorkiewicz. Trapping time of excitons in Si nanocrystals embedded in a SiO_2 matrix. *Phys. Rev. B*, 95:195312, 2017.

[105] A.V. Gert and I.N. Yassievich. Role of surface self-trapped excitons in the energy relaxation of photoexcited silicon nanocrystals. *Semiconduct.*, 49:492–497, 2015.

[106] T.M. Demkiv, S.V. Myagkota, T. Malyi, A.S. Pushak, V.V. Vistovskyy, P.M. Yakibchuk, O.V. Shapoval, N.E. Mitina, A.S. Zaichenko, and A.S. Voloshinovskii. Luminescence properties of $CsPbBr_3$ nanocrystals dispersed in a polymer matrix. *J. Lumin.*, 198:103–107, 2018.

[107] C. de Weerd, J. Lin, L. Gomez, Y. Fujiwara, K. Suenaga, and T. Gregorkiewicz. Hybridization of single nanocrystals of Cs_4PbBr_6 and $CsPbBr_3$. *J. Phys. Chem. C*, 121:19490–19496, 2017.

[108] D.J. Norris and M.G. Bawendi. Measurement and assignment of the size-dependent optical spectrum in CdSe quantum dots. *Phys. Rev. B*, 53:16338, 1996.

[109] J. Valenta, R. Juhasz, and J. Linnros. Photoluminescence spectroscopy of single silicon quantum dots. *Appl. Phys. Lett.*, 80:1070–1072, 2002.

[110] M.D. Kapetanakis, W. Zhou, M.P. Oxley, J. Lee, M.P. Prange, S.J. Pennycook, J.C. Idrobo, and S.T. Pantelides. Low-loss electron energy loss spectroscopy: An atomic-resolution complement to optical spectroscopies and application to graphene. *Phys. Rev. B*, 92:125147, 2015.

[111] R. Erni and N.D. Browning. Quantification of the size-dependent energy gap of individual CdSe quantum dots by valence electron energy-loss spectroscopy. *Ultramicroscopy*, 107:267–273, 2007.

[112] O.L. Krivanek, M.F. Chisholm, V. Nicolosi, T.J. Pennycook, G.J. Corbin, N. Dellby, M.F. Murfitt, C.S. Own, Z.S. Szilagyi, M.P. Oxley, and S.T. Pantelides. Atom-by-atom structural and chemical analysis by annular dark-field electron microscopy. *Nature*, 464:571–574, 2010.

[113] J. de Roo, M. Ibánez, P. Geiregat, G. Nedelcu, W. Walraven, J. Maes, J.C. Martins, I. Van Driessche, M.V. Kovalenko, and Z. Hens. Highly dynamic ligand binding and light absorption coefficient of cesium lead bromide perovskite nanocrystals. *ACS Nano*, 10:2071–2081, 2016.

[114] D. Steiner, A. Aharoni, U. Banin, and O. Millo. Level structure of InAs quantum dots in two-dimensional assemblies. *Nano Lett.*, 6:2201, 2006.

[115] P.D. Nellist and S.J. Pennycook, editors. *Scanning Transmission Electron Microscopy: Imaging and Analysis*. Springer Science & Business Media, 2011.

[116] Y. Yuan, Z. Liu, Z. Liu, L. Peng, Y. Li, and A. Tang. Photoluminescence and self-assembly of cesium lead halide perovskite nanocrystals: Effects of chain length of organic amines and reaction temperature. *Appl. Surf. Sci.*, 405:280–288, 2017.

[117] D. Amgar, A. Stern, D. Rotem, D. Porath, and L. Etgar. Tunable length and optical properties of $CsPbX_3$ (X = Cl, Br, I) nanowires with a few unit cells. *Nano Lett.*, 17:1007–1013, 2017.

[118] M. Imran, F. Di Stasio, Z. Dang, C. Canale, A.H. Khan, J. Shamsi, R. Brescia, M. Prato, and L. Manna. Colloidal synthesis of strongly fluorescent $CsPbBr_3$ nanowires with width tunable down to the quantum confinement regime. *Chem. Mater.*, 28:6450–6454, 2016.

[119] D. Zhang, Y. Yu, Y. Bekenstein, A.B. Wong, A.P. Alivisatos, and P. Yang. Ultrathin colloidal cesium lead halide perovskite nanowires. *J. Am. Chem. Soc.*, 138:13155–13158, 2016.

[120] S. Seth and A. Samanta. A facile methodology for engineering the morphology of $CsPbX_3$ perovskite nanocrystals under ambient condition. *Sci. Rep.*, 6:37693, 2016.

[121] Q.A. Akkerman, S.G. Motti, A.R. Srimath Kandada, E. Mosconi, V. DInnocenzo, G. Bertoni, S. Marras, B.A. Kamino, L. Miranda, F. De Angelis, and A. Petrozza. Solution synthesis approach to colloidal cesium lead halide perovskite nanoplatelets with monolayer-level thickness control. *J. Am. Chem. Soc.*, 138:1010–1016, 2016.

[122] J. Shamsi, Z. Dang, P. Bianchini, C. Canale, F. Di Stasio, R. Brescia, M. Prato, and L. Manna. Colloidal synthesis of quantum confined single crystal $CsPbBr_3$ nanosheets with lateral size control up to the micrometer range. *J. Am. Chem. Soc.*, 138:7240–7243, 2016.

[123] F. Somma, P. Aloe, S. Lo Mastro, C. Giampaolo, M. Nikl, K. Nitsch, P. Fabeni, and G.P. Pazzi. Free and localised exciton of ternary nanocrystals in CsX-PbX_2 thin films (X= Cl, Br, I). *Radiat. Eff. Defects Solids*, 156:103–107, 2001.

[124] M. Nikl, E. Mihokova, K. Nitsch, F. Somma, C. Giampaolo, G.P. Pazzi, P. Fabeni, and S. Zazubovich. Photoluminescence of Cs_4PbBr_6 crystals and thin films. *Chem. Phys. Lett.*, 306:280–284, 1999.

[125] S. Kondo, K. Amaya, and T. Saito. Localized optical absorption in :Cs_4PbBr_6. *J. Phys. Cond. Mat.*, 14:2093, 2002.

[126] Q.A. Akkerman, S. Park, E. Radicchi, F. Nunzi, E. Mosconi, F. De Angelis, R. Brescia, P. Rastogi, M. Prato, and L. Manna. Nearly monodisperse insulator Cs_4PbX_6 (X= Cl, Br, I) nanocrystals, their mixed halide compositions, and their transformation into $CsPbX_3$ nanocrystals. *Nano Lett.*, 17:1924–1930, 2017.

[127] F. Palazon, C. Urso, L. De Trizio, Q.A. Akkerman, S. Marras, F. Locardi, I. Nelli, M. Ferretti, M. Prato, and L. Manna. Postsynthesis transformation of insulating Cs_4PbBr_6 nanocrystals into bright perovskite $CsPbBr_3$ through physical and chemical extraction of CsBr. *ACS Energy Lett.*, 2:2445–2448, 2017.

[128] R.H. Andrews, S.J. Clark, J.D. Donaldson, J.C. Dewan, and J. Silver. Solid-state properties of materials of the type Cs_4MX_6 (where M= Sn or Pb and X= Cl or Br). *J. Chem. Soc.*, 4:767–770, 1983.

[129] M. Velázquez, A. Ferrier, S. Péchev, P. Gravereau, J.P. Chaminade, X. Portier, and R. Moncorgé. Growth and characterization of pure and Pr^{3+}-doped Cs_4PbBr_6 crystals. *J. Crystal Growth*, 310:5458–5463, 2008.

[130] G. Conte, F. Somma, and M. Nikl. Nanocrystalline $CsPbBr_3$ thin films: a grain boundary opto-electronic study. *Phys. Status Solidi C*, 2:306–309, 2005.

[131] C. de Weerd, L. Gomez, H. Zhang, W.J. Buma, G. Nedelcu, M.V. Kovalenko, and T. Gregorkiewicz. Energy transfer between inorganic perovskite nanocrystals. *J. Phys. Chem. C*, 120(24):13310–13315, 2016.

[132] V. Babin, P. Fabeni, E. Mihokova, M. Nikl, G.P. Pazzi, N. Zazubovich, and S. Zazubovich. Luminescence of Cs_4PbX_6 aggregates in as-grown and in annealed CsBr:Pb single crystals. *Phys. Status Solidi B*, 219:205–214, 2000.

[133] M.I. Saidaminov, J. Almutlaq, S. Sarmah, I. Dursun, A.A. Zhumekenov, R. Begum, J. Pan, N. Cho, O.F. Mohammed, and O.M. Bakr. Pure Cs_4PbBr_6: highly luminescent zero-dimensional perovskite solids. *ACS Energy Lett.*, 1:840–845, 2016.

[134] J.H. Cha, J.H. Han, W. Yin, C. Park, Y. Park, T.K. Ahn, J.H. Cho, and D.Y. Jung. Photoresponse of $CsPbBr_3$ and Cs_4PbBr_6 perovskite single crystals. *J. Phys. Chem. Lett.*, 8:565–570, 2017.

[135] Y. Rakita, N. Kedem, S. Gupta, A. Sadhanala, V. Kalchenko, M.L. Bohm, M. Kulbak, R.H. Friend, D. Cahen, and G. Hodes. Low-temperature solution-grown $CsPbBr_3$ single crystals and their characterization. *Cryst. Growth Des.*, 16:5717–5725, 2016.

[136] R. Aceves, V. Babin, M.B. Flores, P. Fabeni, A. Maaroos, M. Nikl, K. Nitsch, G.P. Pazzi, R.P. Salas, I. Sildos, and N. Zazubovich. Spectroscopy of $CsPbBr_3$ quantum dots in CsBr:Pb crystals. *J. Lumin.*, 93:27–41, 2001.

[137] L.N. Quan, R. Quintero-Bermudez, O. Voznyy, G. Walters, A. Jain, J.Z. Fan, X. Zheng, Z. Z. Yang, and E.H. Sargent. Highly emissive green perovskite nanocrystals in a solid state crystalline matrix. *Adv. Mater.*, 29:1605945–1605951, 2017.

[138] L. Xu, J. Chen, J. Song, J.Li, J. Xue, Y Y. Dong, B. Cai, Q. Shan, B. Han, and H. Zeng. Double-protected all-inorganic perovskite nanocrystals by crystalline matrix and silica for triple-modal anti-counterfeiting codes. *ACS Appl. Mater. Int.*, 9:26556–26564, 2017.

[139] F. Palazon, F. Di Stasio, S. Lauciello, R. Krahne, M. Prato, and L. Manna. Evolution of $CsPbBr_3$ nanocrystals upon post-synthesis annealing under an inert atmosphere. *J. Mater. Chem. C*, 4:9179–9182, 2016.

[140] J.B. Hoffman, A.L. Schleper, and P.V. Kamat. Transformation of sintered $CsPbBr_3$ nanocrystals to cubic $CsPbI_3$ and gradient $CsPbBr_xI_{3-x}$ through halide exchange. *J. Am. Chem. Soc.*, 138:8603–8611, 2016.

[141] T. Hanrath. Colloidal nanocrystal quantum dot assemblies as artificial solids. *J. Vac. Sci. Technol.*, 30:030802, 2012.

[142] N. Soetan, W.R. Erwin, A.M. Tonigan, D.G. Walker, and R. Bardhan. Solvent-assisted self-assembly of $CsPbBr_3$ perovskite nanocrystals into one-dimensional superlattice. *J. Phys. Chem. C*, 121:18186–18194, 2017.

[143] M.V. Kovalenko and M.I. Bodnarchuk. Lead halide perovskite nanocrystals: From discovery to self-assembly and applications. *CHIMIA Int. J. Chem.*, 71:461–470, 2017.

[144] M.V. Kovalenko, L. Protesescu, and M.I. Bodnarchuk. Properties and potential optoelectronic applications of lead halide perovskite nanocrystals. *Science*, 358:745–750, 2017.

[145] W.D.A.M. de Boer, D. Timmerman, K. Dohnalova, I.N. Yassievich, H. Zhang, W.J. Buma-vand, and T. Gregorkiewicz. Red spectral shift and enhanced quantum efficiency in phonon-free photoluminescence from silicon nanocrystals. *Nat. Nanotech.*, 5:878, 2010.

[146] T. Udayabhaskararao, M. Kazes, L. Houben, H. Lin, and D. Oron. Nucleation, growth, and structural transformations of perovskite nanocrystals. *Chem. Mater.*, 29:1302–1308, 2017.

[147] L. Gomez, J. Lin, C. de Weerd, L. Poirier, S.C. Boehme, E.L. von Hauff, Y. Fujiwara, K. Suenaga, and T. Gregorkiewicz. Extraordinary interfacial stitching between single all-inorganic perovskite nanocrystals. *ACS Appl. Mater. Int.*, 10:5984–5991, 2018.

[148] M.P. Boneschanscher, W.H. Evers, J.J. Geuchies, T. Altantzis, B. Goris, F.T. Rabouw, S.A.P. van Rossum, H.S.J. van der Zant, L.D.A. Siebbeles, G. van Tendeloo, I. Swart, J. Hilhorst, A.V. Petukhov, S. Bals, and D. Vanmaekelbergh. Long-range orientation and atomic attachment of nanocrystals in 2D honeycomb superlattices. *Science*, 344:1377–1380, 2014.

[149] M. Kulbak, D. Cahen, and G. Hodes. How important is the organic part of lead halide perovskite photovoltaic cells? Efficient $CsPbBr_3$ cells. *J. Phys. Chem. Lett.*, 6:2452–2456, 2015.

[150] V.L. Nguyen, B.G. Shin, D.L. Duong, S.T. Kim, D. Perello, Y.J. Lim, Q.H. Yuan, F. Ding, H.Y. Jeong, H.S. Shin, S.M. Lee, S.H. Chae, Q.A. Vu, and S.H. Lee. Seamless stitching of graphene domains on polished copper (111) foil. *Adv. Mater.*, 27:1376–1382, 2015.

[151] E. Rabani, D.R. Reichman, P.L. Geissier, and L.E. Brus. Drying-mediated self-assembly of nanoparticles. *Nature*, 426:271–274, 2003.

[152] J. Li, X. Yuan, P. Jing, J. Li, M. Wei, J. Hua, J. Zhao, and L. Tian. Temperature-dependent photoluminescence of inorganic perovskite nanocrystal films. *RSC Adv.*, 6:78311–78316, 2016.

[153] X. Li, D. Yu, F. Cao, Y. Gu, Y. Wei, Y. Wu, J. Song, and H. Zeng. Healing all-inorganic perovskite films via recyclable dissolution-recyrstallization for compact and smooth carrier channels of optoelectronic devices with high stability. *Adv. Funct. Mater.*, 26:5903–5912, 2016.

[154] S.M. Menke and R.J. Holmes. Exciton diffusion in organic photovoltaic cells. *Energy Environ. Sci.*, 7:499–512, 2014.

[155] G. Allan and C. Delerue. Energy transfer between semiconductor nanocrystals: Validity of Förster's theory. *Phys. Rev. B*, 75:195311–1 – 195311–8, 2007.

[156] S.A. Crooker, J.A. Hollingsworth, S. Tretiak, and V.I. Klimov. Spectrally resolved dynamics of energy transfer in quantum-dot assemblies: Towards engineered energy flows in artificial materials. *Phys. Rev. Lett.*, 89:1868021–1868024, 2002.

[157] M. Lunz, A.L. Bradley, W.Y. Chen, and Y.K. Gunko. Förster resonant energy transfer in quantum dot layers. *Superlattices and Microstructures*, 47:98 – 102, 2010.

[158] R. Limpens, A. Lesage, P. Stallinga, A.N. Poddubny, M. Fujii, and T. Gregorkiewicz. Resonant energy transfer in Si nanocrystal solids. *J. Phys. Chem. C.*, 119:19565–19570, 2015.

[159] J. Yin, D. Cortecchia, A. Krishna, S. Chen, N. Mathews, C. Grimsdale, and C. Soci. Interfacial charge transfer anisotropy in polycrystalline lead iodide perovskite films. *J. Phys. Chem. Lett.*, 6:1396–1402, 2015.

[160] J.I. Pankove. *Optical Processes in Semiconductors.* Dover: New York, 1971.

[161] J.R. Lakowicz. *Principles of Fluorescence Spectroscopy.* Springer US, 2006.

[162] S. Mayilo, J. Hilhorst, A.S. Susha, C. Hohl, T. Franzl, T.A. Klar, A.L. Rogach, and J. Feldmann. Energy transfer in solution-based clusters of CdTe nanocrystals electrostatically bound by calcium ions. *J. Phys. Phys.Chem. C,*, 112:14589–14594, 2008.

[163] J. Pan, S.P. Sarmah, B. Murali, I. Dursum, W. Peng, and M.R. Parida. Air-stable surface-passivated perovskite quantum dots for ultra-robust, single- and two-photon-induced amplified spontaneous emission. *J. Phys. Chem. Lett.*, 6:5027–5033, 2015.

[164] B. Luo, Y.-C. Pu, S. A. Lindley, Y. Yang, L. Lu, Y. Li, X. Li, and J. Z. Zhang. Organolead halide perovskite nanocrystals: branched capping ligands control crystal size and stability. *Angew. Chem. Int. Ed.*, 55:8864–8868, 2016.

[165] B. Dubertret, P. Skourides, D.J. Norris, V. Noireaux, A.H. Brivanlou, and A. Libchaber. In vivo imaging of quantum dots encapsulated in phospholipid micelles. *Science*, 298:1759–1762, 2002.

[166] Gao X., Cui Y., Levenson R.M., Chung L.W., and Nie S. In vivo cancer targeting and imaging with semiconductor quantum dots. *Nat. Biotechnol.*, 22:969–976, 2004.

[167] S. Huang, Z. Li, L. Kong, N. Zhu, A. Shan, and L. Li. Enhancing the stability of $CH_3NH_3PbBr_3$ quantum dots by embedding in silica spheres derived from tetramethyl orthosilicate in waterless toluene. *J. Am. Chem. Soc.*, 138:5749–5752, 2016.

[168] H. Huang, B. Chen, Z. Wang, T.F. Hung, A.S. Susha, H. Zhong, and A.L. Rogach. Water resistant $CsPbX_3$ nanocrystals coated with polyhedral oligomeric silsesquioxane and their use as solid state luminophores in all-perovskite white light-emitting devices. *Chem. Sci.*, 7:5699–5703, 2016.

[169] W. Mehnert and K. Mader. Solid lipid nanoparticles: production, characterization and applications. *Adv. Drug Delivery Rev.*, 47:165–196, 2001.

[170] R.H. Muller, M. Radtke, and S.A. Wissing. Solid lipid nanoparticles (SLN) and nanostructured lipid carriers (NLC) in cosmetic and dermatological preparations. *Adv. Drug Deliver. Rev.,*, 54:S131–S155, 2002.

[171] E.J. Henderson, A.J. Shuhendler, P. Prasad, V. Baumann, F. Maier-Flaig, D.O. Faulkner, U. Lemmer, X.Y. Wu, and G.A. Ozin. Colloidally stable silicon nanocrystals with near-infrared photoluminescence for biological fluorescence imaging. *Small*, 17:2507–2516, 2011.

[172] G-H. Chai, Y. Xu, S-Q. Chen, B. Cheng, F-Q. Hu, J. You, Y-Z. Du, and H. Yuan. Transport mechanisms of solid lipid nanoparticles across Caco-2 cell monolayers and their related cytotoxicology. *ACS Appl. Mater. Interfaces*, 8:5929–5940, 2016.

[173] F-Q. Hu, S-P. Jiang, Y-Z. Du, H. Yuan, Y-Q. Ye, and S. Zeng. Solid lipid nanoparticles of stearic acid for the drug delivery of paliperidone. *Colloid. Surface B,*, 45:167–173., 2005.

[174] A. Kosmala, R. Wright, Q. Zhang, and P. Kirby. Synthesis of silver nano particles and fabrication of aqueous Ag inks for inkjet printing. *Mater. Chem. Phys.*, 29:1075–1080, 2011.

[175] W. Jiang, B.Y.S. Kim, J.T. Rutka, and W.C.W. Chan. Nanoparticle-mediated cellular response is size-dependent. *Nat. Nanotech.*, 3:145–150, 2008.

[176] A. Kojima, K. Teshima, Y. Shirai, and T. Miyasaka. Organometal halide perovskites as visible-light sensitizers for photovoltaic cells. *J. Am. Chem. Soc.*, 131(17):6050–6051, 2009.

[177] S.S. Shin, E.J. Yeom, W.S. Yang, S. Hur, M.G. Kim, J. Im, J. Seo, J.H. Noh, and S.I. Seok. Colloidally prepared La-doped $BaSnO_3$ electrodes for efficient, photostable perovskite solar cells. *Science*, 356(6334):167–171, 2017.

[178] K. Yoshikawa, H. Kawasaki, W. Yoshida, T. Irie, K. Konishi, K. Nakano, T. Uto, D. Adachi, M. Kanematsu, and H. Uzu K. Yamamoto. Silicon heterojunction solar cell with interdigitated back contacts for a photoconversion efficiency over 26%. *Nat. Energy*, 20(2):17032, 2017.

[179] L.M. Pazos-Outón, M. Szumilo, R. Lamboll, J.M. Richter, M. Crespo-Quesada, M. Abdi-Jalebi, H.J. Beeson, Vrućinić, M. Alsari, H.J. Snaith, and B. Ehrler. Photon recycling in lead iodide perovskite solar cells. *Science*, 351:1430–1433., 2016.

[180] F. Palazon, F. Di Stasio, Q.A. Akkerman, R. Krahne, M. Prato, and L. Manna. Polymer-free films of inorganic halide perovskite nanocrystals as UV-to-white color-conversion layers in LEDs. *Chem. Mater.*, 28:2902–2906, 2016.

[181] T. Xuan, X. Yang, S. Lou, J. Huang, Y. Liu, J. Yu, H. Li, K.L. Wong, C. Wang, and J. Wang. Highly stable $CsPbBr_3$ quantum dots coated with alkyl phosphate for white light-emitting diodes. *Nanoscale*, 9:15286–15290, 2017.

[182] J. Li, L. Xu, T. Wang, J. Song, J. Chen, J. Xue, Y. Dong, B. Cai, Q. Shan, B. Han, and H. Zeng. 50-fold EQE improvement up to 6.27% of solution-processed all-inorganic perovskite $CsPbBr_3$ QLEDs via surface ligand density control. *Adv. Mater.*, 29:1603885, 2017.

[183] Z. Wei, A. Perumal, R. Su, S. Sushant, J. Xing, Q. Zhang, S.T. Tan, H.V. Demir, and Q. Xiong. Solution-processed highly bright and durable cesium lead halide perovskite light-emitting diodes. *Nanoscale*, 8:18021–18026, 2016.

[184] Y. Wang, X. Li, J. Song, L. Xiao, H. Zeng, and H. Sun. All-inorganic colloidal perovskite quantum dots: A new class of lasing materials with favorable characteristics. *Adv. Mater.*, 27:7101–7108, 2015.

[185] S. Yakunin, L. Protesescu, F. Krieg, M.I. Bodnarchuk, G. Nedelcu, M. Humer, G. De Luca, M. Fiebig, W. Heiss, and M.V. Kovalenko. Low-threshold amplified spontaneous emission and lasing from colloidal nanocrystals of cesium lead halide perovskites. *Nat. Commun.*, 6:8056–8064, 2015.

[186] C.Y. Huang, C. Zou, C. Mao, K.L. Corp, Y.C. Yao, Y.J. Lee, C.W. Schlenker, A.K. Jen, and L.Y. Lin. $CsPbBr_3$ perovskite quantum dot vertical cavity lasers with low threshold and high stability. *ACS Photon.*, 4:2281–2289, 2017.

[187] R.J. Sutton, G.E. Eperon, L. Miranda, E.S. Parrott, B.A. Kamino, J.B. Patel, M.T. Hörantner, M.B. Johnston, A.A. Haghighirad, D.T. Moore, and H.J. Snaith. Bandgap-tunable cesium lead halide perovskites with high thermal stability for efficient solar cells. *Adv. Energy Mater.*, 6:1502458, 2016.

[188] D. Zhou, D. Liu, G. Pan, X. Chen, D. Li, W. Xu, X. Bai, and H. Song. Cerium and ytterbium codoped halide perovskite quantum dots: A novel and efficient downconverter for improving the performance of silicon solar cells. *Adv. Mater.*, 29:1704149, 2017.

[189] S. Miura, T. Nakamura, M. Fujii, M. Inui, and S. Hayashi. Size dependence of photoluminescence quantum efficiency of Si nanocrystals. *Phys. Rev. B.*, 73:245333, 2006.

[190] B.S. Richards. Enhancing the performance of silicon solar cells via the application of passive luminescence conversion layers. *Sol. Energ. Mat. Sol. Cells.*, 90:2329–2337, 2006.

[191] M.V. Wolkin, J. Jorne, P. M. Fauchet, G. Allan, and C. Delerue. Electronic states and luminescence in porous silicon quantum dots: the role of oxygen. *Am. Phys. Soc.*, 82(1):197, 1998.

[192] R. Limpens and T. Gregorkiewicz. Spectroscopic investigations of dark Si nanocrystals in SiO_2 and their role in external quantum efficiency quenching. *J. Appl. Phys.*, 114:074304, 2013.

[193] D.C. Lee, J.M. Pietryga, I. Robel, D.J. Werder, R.D. Schaller, and V.I. Klimov. Colloidal synthesis of infrared-emitting germanium nanocrystals. *J. Am. Chem. Soc.*, 131:3436–3437, 2009.

[194] J.G. Veinot. Synthesis, surface functionalization, and properties of freestanding silicon nanocrystals. *Chem. Comm.*, 40:4160–4168, 2006.

[195] J.R. Siekierzycka, M. Rosso-Vasic, H. Zuilhof, and A.M. Brouwer. Photophysics of n-butyl-capped silicon nanoparticles. *J. Phys. Chem.*, 115:20888–20895, 2011.

[196] K. Dohnalova, A.N. Poddubny, A.A. Prokofiev, C.P. Umesh, J.M.J. Paulusse, W. D. A. M. de Boer, H. Zuilhof, and T. Gregorkiewicz. Surface brightens up Si quantum dots: direct bandgap-like size-tunable emission. *Light Sci. Appl.*, 2, 2012.

[197] Y. Wang and A. Hu. Carbon quantum dots: synthesis, properties and applications. *J. Mater. Chem. C.*, 2:6921–6939, 2014.

[198] J. Shen, Y. Zhu, X. Yang, J. Zong, J. Zhang, and C. Li. One-pot hydrothermal synthesis of graphene quantum dots surface-passivated by polyethylene glycol and their photoelectric conversion under near-infrared light. *New J. Chem.*, 36:97–101, 2012.

[199] J. Gu, M.J. Hu, Q.Q. Guo, Z.F. Ding, X.L. Sun, and J. Yang. High-yield synthesis of graphene quantum dots with strong green photoluminescence. *RSC Advances*, 4:50141–50144, 2014.

[200] P.R. Kharangarh, S. Umapathy, and G. Singh. Effect of defects on quantum yield in blue emitting photoluminescent nitrogen doped graphene quantum dots. *J. Appl. Phys.*, 122:145107, 2017.

[201] N. Mohanty, D. Moore, Z. Xu, T.S. Sreeprasad, A. Nagaraja, A.A. Rodriguez, and V. Berry. Nanotomy-based production of transferable and dispersible graphene nanostructures of controlled shape and size. *Nat Comm.*, 3:844, 2012.

[202] F.A. Reboredo and G. Galli. Theory of alkyl-terminated silicon quantum dots. *J. Phys. Chem.*, 109:1072–1078, 2005.

[203] S. Zhu, Y. Song, X. Zhao, J. Shao, J. Zhang, and B. Yang. The photoluminescence mechanism in carbon dots (graphene quantum dots, carbon nanodots, and polymer dots): current state and future perspective. *Nano Research*, 8:355–381, 2015.

[204] L. Ruizendaal, S.P Pujari, V. Gevaerts, J.M. Paulusse, and H. Zuilhof. Bio-functional silicon nanoparticles via thiolene click chemistry. *Chem. Asian J.*, 6:2776–2786, 2011.

[205] C-S Yang, R.A. Bley, S.M. Kauzlarich, H.W.H. Lee, and G.R. Delgado. Synthesis of alkyl-terminated silicon nanoclusters by a solution route. *J. Am. Chem. Soc.*, 121:5191–5195, 1999.

[206] K.A. Pettigrew, Q. Liu, P.P. Power, and S.M. Kauzlarich. Solution synthesis of alkyl-and alkyl/alkoxy-capped silicon nanoparticles via oxidation of mg_2Si. *Chem. of Mater.*, 15:4005–4011, 2003.

[207] Y. Kanemitsu. Visible photoluminescence of nanometer-size Ge crystallites in SiO_2 glassy matrices. *J. Non Cryst. Sol.*, 164:639–642, 1993.

[208] Y. Maeda. Visible photoluminescence from nanocrystallite Ge embedded in a glassy SiO_2 matrix, evidence in support of the quantum-confinement mechanism. *Phys. Rev. B*, 51:1658–1670, 1995.

[209] S.F. Wuister, C. de Mello Donega, and A. Meijerink. Influence of thiol capping on the exciton luminescence and decay kinetics of CdTe and CdSe quantum dots. *J. Phys. Chem. B*, 108:17393–17397, 2004.

[210] P.Y. Yu and M. Cardona, editors. *Fundamentals of Semiconductors: Physics and Materials Properties*. Springer Science & Business Media, 2010.

Summary

Hot electrons in cool nanocrystals

In this work, the main focus is on all-inorganic perovskite nanocrystals (IP-NCs) that are studied from a microscopy and spectroscopy point of view. This encompasses optical-, transient absorption- (TA) and electron energy loss spectroscopies (EELS) and (high resolution) scanning transmission electron microscopy (STEM). Due to a direct band gap and high photoluminescence (PL) efficiencies, the IP-NCs lend themselves very well for these various techniques. Moreover, their outstanding characteristics are the major reason why the IP-NCs recently have attracted a lot of attention. The high potential of this semiconductor nanomaterial for the development of efficient and low-cost devices (e.g. light emitting devices for full-color full-size and micro-displays, photodetectors, solar cells, and lasers) stimulates intensive research, and many remarkable results have been obtained, with the number of related scientific articles growing every day.

In particular, the process of carrier multiplication in semiconductor NCs counteracts the loss of energy through thermalization of hot carriers created upon high-energy photo-excitation. As such, carrier multiplication in all-inorganic $CsPbI_3$ NCs is revealed and described. The evidence is obtained using ultrafast TA spectroscopy, by comparing the photo-induced bleach and absorption dynamics at different excitation energies, typically below and above the threshold energy. Upon excitation with sufficiently high photon energy, an additional fast component appears in the transients due to Auger recombination - which is the generally accepted characteristic fingerprint of carrier multiplication.

TEM imaging allows for direct visualization of NCs, with the high resolution microscopy providing information about their composition, crystal structure, size and shape, aggregation, and ordering when in an ensemble. In addition, recent developments in low-energy monochromatic TEM with advanced aberration correctors, have enabled the combination of STEM and EELS with ultra-high spatial and energy resolutions. The EELS technique can give important insights into the energy structure of individual IP-NCs. In this way, it has been revealed that the energy structure of a (single) IP-NC is different when isolated and in an ensemble, which means that neighboring NCs interact with each other. This technique has also allowed for distinguishing between different polymorphs (semiconductor, insulator, or hybrid materials) of perovskite which typically are simultaneously produced during the synthesis. The characteristics of green-emitting $CsPbBr_3$ and insulating Cs_4PbBr_6 NCs were investigated at a single object level. It has been shown that the two materials co-exist and inevitably hybridize forming nanoparticles with a spherical shape. Herein, the optical characteristics of the parent materials are preserved, allowing for an increased absorption in the UV due to Cs_4PbBr_6, accompanied by the distinctive efficient green emission resulting from $CsPbBr_3$. While performing these measurements, which are typically done on fresh drop-casted NCs, the spontaneous merging of $CsPbBr_3$ NCs was discovered. The aggregation between individual NCs was investigated at the atomic level and showed that the merging process preserves the elemental composition and electronic structure of the $CsPbBr_3$ NCs, and takes place between NCs of different size and orientation. The merging process, however, is arrested by exposure to the electron beam, while at the same time, its interaction with the IP-NCs can induce their damage, transformations and even complete degradation.

Apart from coupling between the IP-NCs, an energy transfer can also take place. By making use of (time-resolved) optical spectroscopy, the spectral changes related to this process are investigated.

This has been specifically observed when IP-NCs of different sizes (but with the same composition) are mixed, because the energy transfer is driven by the band gap energy difference. As such, the transfer always proceeds from small to large NCs. Apart from a resonant transfer of energy, also photon recycling is directed by the NCs size. In contrast to the earlier mentioned energy transfer, this phenomenon proceeds through radiative recombination rather than resonantly, and encompasses reabsorption and re-emission of photons. It was shown that $CsPbBr_3$ NCs - exhibiting the highest efficiency of the three halides - are an excellent host material for photon recycling. As a result, the excitation distribution in the colloid is no longer limited by the pump photon diffusion length, but can occur over longer distances making use of photon recycling.

It is well-known that if IP-NCs of different composition are mixed, anion exchange takes place, which affects the original PL emission. For example, joining colloidal solutions of $CsPbBr_3$ and $CsPbI_3$ NCs, the final product evidently contains $CsPb(Br/I)_3$ NCs, and the resulting PL emission will be centered in between those of the initial materials. Also, the IP-NCs are incompatible with polar solvents. Upon contact with water, they disintegrate and their structure is destroyed. Both of these drawbacks, anion exchange and incompatibility with water, are solved by encapsulation of the IP-NCs in lipid solid structures made of stearic acid. The encapsulated IP-NCs are water-stable and anion-exchange is fully arrested when mixing NCs of different halide composition.

Group IV semiconductor NCs commonly serve as an alternative to direct band gap materials containing toxic and/or rare elements. They are characterized by large abundance, chemical and structural stability and low toxicity. However, their optical properties are inferior to those of II-VI and III-V semiconductor NCs (e.g. CdSe, CdTe, PbSe and InAs) as well as to the perovskite materials. An often sought-after method to improve the efficiency, is through capping the surface with organic ligands. Following this approach, the optical properties of butyl-terminated Si and Ge NCs are studied, and compared to the characteristics of graphene NCs. This comparison reveals a different microscopic origin for absorption and radiative recombination, in all three investigated NC systems.

Samenvatting

Hete elektronen in koude nanokristallen

In deze thesis ligt de nadruk op volledig anorganische perovskiete nanokristallen (*Eng:* all-inorganic perovskite nanocrystals, IP-NCs), welke bestudeerd zijn door middel van spectroscopie en microscopie. Hierbij wordt gebruik gemaakt van de volgende technieken: optische, hyperspectrale transiente absorptie (TA), en elektronen energieverlies spectroscopie (EELS) alsmede elektronenmicroscopie (STEM). De IP-NCs worden gekarakteriseerd door een directe bandkloof en daardoor een hoge fotoluminiscentie-efficiëntie. Dit maakt ze uitermate geschikt voor de zojuist besproken karakterisatietechnieken. Sterker nog, de buitengewone en uitzonderlijke eigenschappen van de IP-NCs zijn één van de voornaamste redenen waarom ze recentelijk bestudeerd worden. Ze zijn zeer geschikt voor, onder andere het gebruik in diodes oftewel LED's, televisieschermen en computer-displays, zonnecellen en lasers. Dit zorgt tot op zekere hoogte voor een stimulans binnen de wetenschap, met als gevolg dat er elke dag nieuwe publicaties verschijnen.

In halfgeleider NCs kan het zogenaamde ladingvermenigvuldigingsproces (*Eng:* carrier multiplication, CM) soms optreden. Het is een proces waarin één hoog-energetisch foton wordt geabsorbeerd, dat vervolgens leidt tot de excitatie van twee of meer elektronen, in plaats van dat het teveel aan energie verloren gaat als warmte. Het is daarom direct in competitie met andere processen zoals het koelen van hete ladingdragers. Dit specifieke proces wordt hier bestudeerd en beschreven in $CsPbI_3$ IP-NCs. Gebruikmakend van TA-spectrocopie, worden de optische transities in de NCs bij hoge en lage excitatie-energie onderzocht, typisch boven en onder tweemaal de bandkloofenergie. Wanneer er voldoende energie geabsorbeerd wordt, zodat Auger-recombinatie plaats kan vinden, zal er in het tijdgerelateerde spectum een karakteristieke component te zien zijn. De verschijning van deze extra component wordt in het algemeen als bewijs aangenomen voor het plaatsvinden van CM.

Voor het visualiseren van IP-NCs wordt gebruik gemaakt van STEM. Op deze manier kan er informatie worden verstrekt met betrekking tot de kristalstructuur, compositie, grootte en vorm wanneer ze zich in een ensemble van NCs bevinden. Door recente ontwikkelingen op het gebied van EELS en STEM met verbeterde aberratie, is het mogelijk om deze twee technieken te combineren, waarbij er een extreem hoge resolutie (zowel ruimtelijk als in energie) op nagehouden wordt. Op deze manier kan tegelijkertijd zowel de grootte als de bandkloofenergie van een enkel nanokristal verkregen worden. Het blijkt dat geïsoleerde NCs in vergelijking met NCs in een ensemble een andere energiestructuur hebben, en dat er een interactie plaatsvindt tussen aangrenzende NCs. Deze techniek is onder andere ook geschikt om een onderscheid te kunnen maken tussen verschillende polymorfen van hetzelfde materiaal. De polymorfen kunnen (ongemerkt) tijdens hetzelfde syntheseproces vervaardigd worden en hun optische eigenschappen worden vaak door elkaar gehaald. Daarom zijn hier geïsoleerde NCs van beide composities - $CsPbBr_3$ en Cs_4PbBr_6 - bestudeerd, waarbij gebleken is dat $CsPbBr_3$ uitzonderlijk licht uitzendt in het zichtbare gedeelte van het spectrum en dat Cs_4PbBr_6 een isolator is. Ook is gebleken dat er een $CsPbBr_3$/Cs_4PbBr_6-hybride gevormd kan worden die de eigenschappen van de originele composities combineerd. Tijdens het uitvoeren van onze experimenten, werd tevens voor het eerst een nog niet bekende eigenschap van de IP-NCs opgemerkt: het fuseren van aangrenzende NCs. Het is ook gebleken dat tijdens dit proces de structuur en compositie van de NCs behouden worden, en dat het fuseren plaatsvindt tussen NCs met verschillende grootte en oriëntatie. De fusie kan tegengegaan worden door de NCs bloot te stellen aan de electronenbundel maar, tegelijkertijd, kan deze blootstelling tot gevolg hebben dat de NCs vernietigd worden, dus enige voorzichtigheid is geboden.

Naast een interactie vindt er ook een overdracht van energie plaats tussen aangrenzende NCs. Door gebruik te maken van tijdgerelateerde fotoluminiscentie zijn de veranderingen in de verkregen spectra ten gevolge van deze resonante energie-overdracht in kaart gebracht. De energie-overdracht komt met name in NCs met verschillende grootte maar gelijke compositie voor, omdat deze overdracht altijd plaatsvindt van kleine naar grotere NCs. Op eenzelfde manier wordt het recyclen van fotonen bestudeerd. In tegenstelling tot het hiervoor genoemde proces, gebeurt dit door middel van re-absorptie en re-emissie van fotonen, dat dientengevolge niet resonant is. Het recyclen van fotonen is bij uitstek in $CsPbBr_3$ NCs bestudeerd, omdat zij de hoogste fotoluminiscentie-efficiëntie hebben (binnen de IP-NCs-familie). Het resultaat van deze bevinding is dat de distributie van het excitatielicht niet langer gelimiteerd wordt door de diffusielengte, maar langere afstanden kan bereiken door middel van het recycleproces.

Het is algemeen bekend dat wanneer IP-NCs van verschillende halogeen-composities worden gemengd, dit direct invloed uitoefend op de fotoluminiscentie. Als bijvoorbeeld, oplossingen met daarin $CsPbBr_3$ en $CsPbI_3$ NCs bij elkaar worden gebracht, zal de uiteindelijke mix $CsPb(Br/I)_3$ NCs bevatten. Het bijbehorende fotoluminiscentie spectrum heeft dan een maximum dat precies tussenin de maxima ligt die horen bij de originele materialen. Daarnaast kunnen de IP-NCs niet in contact gebracht worden met polaire oplossingsmiddelen. In dat geval zal hun structuur direct vernietigd worden zodra ze in contact komen met bijvoorbeeld water. Een uitweg op de twee hierboven genoemde nadelen wordt aangedragen door de IP-NCs te kapselen in lipoïden, die in principe bestaan uit stearinezuur. De ingekapselde NCs zijn zodoende stabiel in water, en NCs met verschillende halogeen-composities kunnen gemengd worden zonder dat de ionen-verwisselijk plaatsvindt en hun emissiekleur wordt beïnvloed.

Als laatste wordt de groep IV halfgeleider-NCs besproken. Zij dienen als een interessant alternatief voor veel gebruikte directe bandkloof-materialen, welke vaak giftige elementen bevatten. Deze elementen zijn in overvloed aanwezig op aarde en/of makkelijk te vergaren, hebben een sterke, stabiele structuur en zijn niet of bijna niet giftig. Een groot nadeel is, dat hun optische eigenschappen inferieur zijn aan die van de II-VI en III-V halfgeleider-NCs (zoals CdSe, CdTe, PbSe en InAs) alsmede aan die van de perovskieten. Een vaak gebruikte methode om de efficiëntie van NCs te verbeteren, is het aanbrengen van organische moleculen op het oppervlak. Om dit te bestuderen, hebben wij de optische eigenschappen van Silicium en Germanium NCs met butyl-moleculen op hun oppervlak, vergeleken met de optische eigenschappen van grafeen NCs. Het is gebleken dat voor alledrie de materialen, het mechanisme dat verantwoordelijk is voor absorptie- en emissieprocessen niet op dezelfde procedure is gebaseerd.

A

Appendix

A Materials and Methods

A.1 Perovskites synthesis

The $CsPbI_3$ NCs (Chapter 2) were synthesized following a slightly modified method of Protesescu *et al*. [5] First, Cs-oleate was prepared by mixing 0.814 g of Cs_2CO_3 with 40 mL of ODE and 2.5 mL of OA; all reactants were dried at 120 °C for 1 h for water removal. The mixture was stirred at 150 °C in inert atmosphere until completion of the reaction. For the NCs formation, 5 mL of ODE and 0.188 mmol of PbI_2 were dried for 1 h at 120 °C in N_2 atmosphere. After removal of H2O, 0.5 mL of dried OLA and 0.5 mL of dried OA were added to the reaction flask and the temperature was raised up to 180 °C. After complete solvation of the $PbBr_2$ salt, 0.4 mL of the Cs-oleate solution previously warmed up was injected. A few seconds later, the NCs solution was quickly cooled down with an ice-water bath. The product was purified by centrifugation and subsequently redispersed in hexane.

The $CsPbBr_3$ NCs (Chapters 3 and 4) were synthesized according to the protocol reported by Protesescu *et al*. Here, 70 mg of $PbBr_2$ is mixed with 5 mL of ODE, 0.5 mL of OLA and 0.5 mL of OA in N_2 atmosphere at the desired reaction temperature (100 °C - 200 °C, reactants were priorly dried). After complete solvation of the $PbBr_2$ salt, 0.4 mL of a warm Cs-oleate solution in ODE is injected in the reaction flask and the NCs are formed instantaneously. After few seconds reaction, the product is cooled down quickly with an ice-water bath. The NCs are washed by several centrifugation steps and redispersed in toluene. The size could be tuned with the reaction temperature: the higher the temperature, the larger the size.

A.2 Butyl-terminated QDs synthesis

The C-Si and C-Ge QDs were synthesized via a wet chemical method adapted from Kauzlarich *et al.* (Chapter 10). First, the reaction system was made oxygen free by consecutively flushing with argon and applying a vacuum. Then, magnesium silicide (germanide) was added to the reaction vessel. The system was loaded with 500 ml of n-octane which was bubbled with argon previously.

Subsequently, 5.2 ml of bromine was carefully added to the mixture and allowed to stir at room temperature for 2 hours after which the mixture was refluxed for 60 hours at 130 °C. During this reaction, the bromo-octanes which form as a major side product are removed by efficient evaporation and fresh n-octane is added to the reaction. The bromine groups were replaced with butyl groups by adding n-butyllithium (5.2 ml) and the whole mixture was left for overnight stirring at room temperature. The excess lithium reagent was quenched by using 30 ml methanol and stirred for 45 mins. The reaction mixture was filtered and washed repeatedly with aqueous hydrochloric acid solution to remove lithium salts. The hexane fraction was subjected to rotatory evaporator to remove any hexane present. The reaction mixture was subjected to column purification using silica column chromatography using hexane and ethylacetate as the mobile phase.

A.3 Graphene QDs synthesis

Graphene oxide (GO, 100 mg) was synthesized by Hummers method. GO film was first individually dispersed in concentrated DMF (100 mL) with oxone (2 g). The mixture solution was sonicated for 1 h. Then, the mixture was transferred to an autoclave (100 ml) and was heated up to 140 for 10 h. The resulting product was then cooled to room temperature and was filtered through a 100 nm nano-porous membrane to separate the carbon based materials. The resulting product solution was further dialyzed in a dialysis bag (retained molecular weight: 2000 Da) for 3 days. See also Ref. [60].

A.4 Encapsulation of the NCs in stearic acid structures

1 mL of the dispersed IP-NCs in toluene (20 mg mL^{-1}) was mixed with 1.5 mg of stearic acid and the mixture was heated up to 75 °C in order to melt the lipid ($\sim$10 min). Thereafter, the organic dispersion was added to a water solution of 0.5 wt% P188 being the volume ratio 1:5 and the two phase system was sonicated for 5 min in a cold water bath ($\sim$10 °C). The micro-emulsion was stirred at room temperature overnight in an open vessel to let the toluene evaporate. Then, the product was washed twice by centrifugation (5000 rpm - 10 minutes) and redispersed in Milli-Q water.

Stearic acid, also called Octadecanoic Acid, is one of the most common long-chain fatty acids, it is a waxy solid with the chemical formula $C_{17}H_{35}CO_2H$. It is found primarily in animal derivatives, but in vegetable fats as well. It is used in a variety of cosmetics and personal care products.

A.5 Ultrafast transient absorption spectroscopy

In the TA experiment for UV pump energies (station 1, $>$4 eV), a Mai Tai-SP (Mountain View, U.S.A.) diode-pumped, mode-locked Ti:sapphire laser, operating at 1 kHz with $\sim$100 fs pulse width and $\sim$3 mJ pulse energy for an output wavelength of 800 nm, was used as a coherent light source. A frequency regulator reduced the output frequency to 200 Hz. A beam splitter was used to separate the beam and to generate the pump and probe pulses. An optical parametric amplifier (OPA), TOPAS-C (Light Conversion, Vilnius, Lithuania) in combination with a BBO crystal, was used to generate the desired pump energy. The pump beam was guided through a delay stage (SGSP 26-200). The probe signal consisted of white light that was generated by using a sapphire crystal, and was spectrally resolved before reaching the detector: a 0.5 m imaging triple grating spectrogram, SpectraPro 2500i

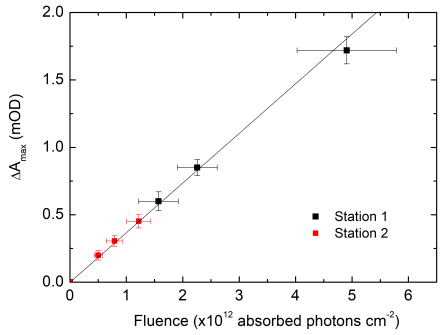

Figure A.1: The number of generated carriers *vs* the absorbed photon fluence. At both stations, the number of generated carriers determined from the PIB maximum as a function of the absorbed photon fluence is shown for 500 nm excitation. It can be seen that the data points follow the same linear dependence.

(Acton Research Corporation, Acton, U.S.A.) and an air-cooled CCD camera, PIXIS 256 (Princeton Instruments, Trenton, U.S.A.) were used.

For the remaining pump energies (station 2, <4 eV), the sample was excited with a ∼150 fs laser pulse (Light Conversion Pharos-SP operating at 2.5 kHz and combined with an Orpheus OPA) and probed using a multichannel detection of visible / near-infrared (500 - 800 nm) probe pulses (Ultrafast Systems Helios). The broad band probe pulses were generated in a sapphire crystal using 1030 nm pump light. We note that the experiments at low pump energies have been repeated at station 1 and the results were subsequently compared. The experiments yielded identical characteristics and as such, validate the results (see figure A.1).

The TA signal is defined as the difference of the optical density (OD) of the excited state and the ground state and is obtained as:

$$
\begin{aligned}
OD &= log_{10}\Big(\frac{I_{total\ indicent\ light}}{I_{transmitted\ light}}\Big) = \Delta OD \\
&= OD_{pump+probe} - OD_{probe} \\
&= log_{10}\Big(\frac{I_{total}}{I_{pump+probe}}\Big) - log_{10}\Big(\frac{I_{total}}{I_{probe}}\Big) \\
&= log_{10}\Big(\frac{I_{total} \cdot I_{probe}}{I_{pump+probe} \cdot I_{total}}\Big) \\
&= log_{10}\Big(\frac{I_{probe}}{I_{pump+probe}}\Big)
\end{aligned}
$$

i.e.

$$\Delta OD(t,\lambda) = log_{10}\frac{I_{off}(\lambda)}{I_{on}(\lambda)}$$

where $I_{off}(\lambda)$ and $I_{on}(\lambda)$ are the transmitted probe fluences with the pump pulse on and off, respectively. While performing the TA experiments, the colloid was stirred to avoid potential charging, although, the stirring of the sample did not induce any difference in the measured dynamics.

A.6 Linear absorption spectroscopy

The optical density was measured in a LAMBDA 950 UV/VIS/NIR spectrophotometer (PerkinElmer). A combination of a tungsten-halogen and deuterium lamps was used together with a PMT and Peltier cooled PbS detector, providing a detection range of E_{det} = 0.4 - 5.6 eV. The solvent absorption was measured separately and subtracted from the sample spectrum.

A.7 Photoluminescence spectroscopy

The PL has been studied under excitation by a Nd:YAG-pumped optical parametric oscillator (OPO) (repetition rate f $\sim$ 100 Hz, pulse width δt = 5 ns, excitation energy E_{exc} = 2.88 eV), and collected under a right-angle geometry and subsequently detected by a CCD (Hamamatsu S10141-1108S) coupled to a spectrometer (Solar, M266) or a PMT (Hamamatsu R9110). The spectra were corrected for the spectral sensitivity of the setup.

The samples were also placed in an integrating sphere to determine the PL QY, using a 150 W xenon lamp coupled to a spectrometer (Solar, MSA-130) as an excitation source. The PL emission and excitation light are scattered diffusively in the integrating sphere and detected by the CCD.

The PLE was recorded using a Jobin Yvon FluoroLog spectrofluorometer (Horiba) equipped with a 450 W xenon lamp (250-700 nm) coupled to a monochromator to provide a range of selective excitation wavelengths. The emission was collected in right-angle geometry and was corrected for the spectral sensitivity of the setup.

The time-resolved PL measurements were performed using a LifeSpec II (Edinburgh Instruments) time-correlated single photon counting (TCSPC) fluorescence lifetime spectrometer, with a 230-850 nm detection range (MCP-PMT). A picosecond pulsed diode laser (λ_{det} = 375 nm, EPL series) provided a 100 ps pulse width. A right angle between excitation and emission beam paths was maintained to avoid detecting scattered excitation light.

A.8 Transmission electron microscopy

All STEM and EELS experiments were performed at the National Institute of Advanced Industrial Science and Technology (AIST) in Tsukuba. The NCs were dropcasted onto an Au quantifoil TEM grid with the coverage of monolayer graphene, and left shortly to dry. STEM imaging and EELS experiments were performed on a JEOL ARM200 microscope equipped with a Schottky thermal emission gun, a JEOL double Wien filter monochromator, probe delta corrector and a Gatan Quantum GIF spectrometer modified for low primary energy operation (15 - 60 keV) with high stability. The experiments were carried out in high-energy resolution mode, where a slit of 0.5 μm was used for energy selection. In this condition, the electron probe has a ZLP with energy FWHM around 50 meV, a current of $\sim$8 pA, and convergence semi-angle of 33 mrad. The EELS collection semi-angle was 11 mrad. The energy dispersion of the spectrometer was set to 10 meV/channel. A Gatan cryo-holder was used to cool down the sample to -110 °C with liquid nitrogen to reduce carbon redeposition and thermal excitation during all the imaging and EELS collection experiments. Dual EELS acquisition was applied where the un-saturated ZLP is used to align the simultaneously

acquired high-loss spectrum (which has much longer exposure time than the ZLP) to correct for any energy drift during the acquisition. The probe size for the valence-loss EELS measurements was about 1.6 Å, providing an ultrahigh spatial resolution during the collection of the EEL spectra. [90–92] All data are raw, without filtering.

For the merging experiments, we drop-casted IP-NCs on amorphous carbon/graphene TEM grids and stored them at room conditions for the spontaneous merging of NCs to occur. Room conditions refer to a typical ambient environment with moderate humidity. To probe the effect of humidity, we drop-casted the same amount of colloidal NCs solution onto two identical grids, and stored them separately under lower (∼20% RH) and higher (∼60% RH) relative humidity conditions, at room temperature. To test the effect of temperature, we used a cooling or heating in-situ sample holder (Gatan) in order to reach the temperature ranges between -110 °C - 90°C and 90 °C - 260 °C, respectively. The electron beam irradiated exposure samples/areas regions are defined to be the regions were exposed to the electron imaging beam directly after drop-casting and subsequent cooling or heating.

A.9 Determination of the band gap energy from the EEL spectra

The spectra were first smoothed by Savitzky-Golay filter with a 10 or 20-point mesh window. We then took the first derivative (the slope of the curve) of the smoothed spectra. Since the step-function-like onset corresponds to a sharp peak in its first derivative, we determine the apex of the peak as the band gap value and the full-width-half-maximum (FWHM) of the peak as the experimental error.

A.10 Fitting procedure using the effective mass theory

From the effective mass theory [210] where the exciton is assumed in a spherical potential well with radius r, the increase of the band gap due to the confinement of the exciton can be expressed as:

$$E_{NC\ band\ gap} = E_{Bulk\ band\ gap} + \frac{\hbar^2\pi^2}{2\mu r^2} - E_{B,exciton} \tag{A.1}$$

where μ is the effective mass of the exciton. Since the exciton binding energy in $CsPbBr_3$ is small ($\sim$ 40 meV), [5] we fitted the measured band gap value into the above equation ignoring the last term of the equation. It should be noted, however, that for non-cubic NCs, such as our $CsPbBr_3$ NCs, the spherical potential is not really applicable and provides only a very approximate description of the QC effect; a more suitable description requires individual confinement in all three dimensions.

A.11 X-ray diffraction measurements

The powder XRD measurement was carried out on a benchtop MiniFlex II X-ray Diffractometer (Rigaku), from 5 to 50 degrees with a turning speed of 2.5 °/min.

A.12 Electrical measurements

For this purpose, the films were fabricated by drop-casting the NCs dispersion onto Au interdigitated electrodes with a 5 μm channel width (DropSens G-IDEAU5). Immediately before drop-casting, the electrodes were electrochemically cleaned in H_2SO_4. The frequency-resolved electrical

measurements were performed in the dark, at 0 V bias voltage and an AC amplitude of 20 mV, using a Metrohm-Autolab electrochemical impedance spectroscopy setup (PGSTAT302N) equipped with a FRA32M module.

A.13 Correction for reabsorption

The optical density (OD) or absorbance (A) is given by:

$$A = -\log_{10} T \tag{A.2}$$

where T is the *transmittance*. From the basic logarithmic rules we find easily:

$$10^{-A} = T \quad \rightarrow \quad 10^{A} = T^{-1} \tag{A.3}$$

The Lambert-Beer law describes how the light is attenuated if it passes through a medium:

$$\log_{10} \frac{I_0(\lambda)}{I(\lambda)} = OD = \epsilon c d \tag{A.4}$$

as (also) described in the book of Joseph R. Lakowicz (p. 56). With some rearranging and rewriting we find:

$$\begin{array}{lcl} \frac{I_0(\lambda)}{I(\lambda)} & = & 10^{OD} \\ I_0(\lambda) & = & \mathrm{I}(\lambda)\ 10^{OD} \\ I_0(\lambda) & = & \mathrm{I}(\lambda)\ 10^{A} \\ I_0(\lambda) & = & \mathrm{I}(\lambda)\ \mathrm{T}^{-1} \end{array}$$

or

$$I_0(\lambda) = \frac{I(\lambda)}{T} \tag{A.5}$$

By definition, the transmittance is given by:

$$T = e^{-\tau} \tag{A.6}$$

where τ is the optical depth. The emitted light travels over a certain distance *d* through the sample (from excitation spot to cuvette edge). The traveling light is attenuated by the absorption coefficient $\alpha(\lambda)$ of the sample. So the optical depth is given by:

$$\tau = \alpha(\lambda) d \tag{A.7}$$

Using equations A.5, A.6 and A.7 we can write:

$$I_0(\lambda) = \frac{I(\lambda)}{e^{\tau}} \quad \rightarrow \quad \frac{I(\lambda)}{e^{-\alpha(\lambda) d}} \tag{A.8}$$

which is exactly equation 6-20 from the book of Jacques I. Pankove (p. 137) and the formula we used to correct our spectra. The absorption coefficient is determined from the (measured) steady-state absorption spectrum, by measuring the transmittance.

List of publications

This thesis is based on the following publications:

1. C. de Weerd, T. Gregorkiewicz and L. Gomez. All-inorganic perovskite nanocrystals: microscopy insights in structure and optical properties. *Adv. Opt. Mater.*, 6 (2018) Invited progress report - Chapters 1 and 9.

2. C. de Weerd, L. Gomez, A. Capretti, D.M. Lebrun, E. Matsubara, J. Lin, M. Ashida, F.C.M. Spoor, L.D.A. Siebbeles, A.J. Houtepen, K. Suenaga, Y. Fujiwara and T. Gregorkiewicz. Efficient carrier multiplication in $CsPbI_3$ perovskite nanocrystals. *Nat. Commun.* Under Review (2018) - Chapter 2.

3. J. Lin, L. Gomez, C. de Weerd, Y. Fujiwara, T. Gregorkiewicz and K. Suenaga. Direct observation of band structure modifications in nanocrystals of $CsPbBr_3$ perovskite. *Nano Lett.*, 16 (2016) - Chapter 3.

4. C. de Weerd, J. Lin, L. Gomez, Y. Fujiwara, K. Suenaga and T. Gregorkiewicz. Hybridization of single nanocrystals of Cs_4PbBr_6 and $CsPbBr_3$. *J. Phys. Chem. C*, 121 (2017) - Chapter 4.

5. L. Gomez, J. Lin, C. de Weerd, L. Poirier, S.C. Boehme, E. von Hauff, Y. Fujiwara, K. Suenaga and T. Gregorkiewicz. Extraordinary interfacial stitching between single all-inorganic perovskite nanocrystals. *ACS Appl. Mater. Int.*, 10 (2018) - Chapter 5.

6. C. de Weerd, L. Gomez, H. Zhang, W.J. Buma, G. Nedelcu, M.V. Kovalenko and T. Gregorkiewicz. Energy transfer between inorganic perovskite nanocrystals. *J. Phys. Chem. C*, 120 (2016) - Chapter 6

7. L. Gomez, C. de Weerd, J.L. Hueso and T. Gregorkiewicz. Color-stable water-dispersed cesium lead halide perovskite nanocrystals. *Nanoscale*, 9 (2016) - Chapter 7.

8. C. de Weerd, A. Capretti, L. Gomez, L. Poirier and T. Gregorkiewicz. Photon recycling in $CsPbBr_3$ perovskite nanocrystals. In preparation (2018) - Chapter 8.

9. C. de Weerd, Y. Shin, E. Marino, J. Kim, H. Lee, S. Saeed and T. Gregorkiewicz. Comparison of the optical properties of graphene and alkyl-terminated Si and Ge quantum dots. *Sci. Rep.*, 7 (2017) - Chapter 10.

Other publications by the author:

10. B. Mitchell, E. Herrmann, J. Lin, L. Gomez, C de Weerd, Y. Fujiwara, K. Suenaga and T. Gregorkiewicz. Measuring the practical particle-in-a-box: orthorhombic perovskite nanocrystals. *Eur. J. Phys*, in press (2018).

11. M.O. Nestoklon, S.V. Goupalov, R.I. Dzhioev, O.S. Ken, V.L. Korenev, Y.G. Kusrayev, V.F. Sapega, C. de Weerd, L. Gomez, T. Gregorkiewicz, J. Lin, K. Suenaga, Y. Fujiwara, L.B. Matyushkin and I.N. Yassievich. Optical orientation and alignment of excitons in ensembles of inorganic perovskite nanocrystals. *Phys. Rev. B*, 97 (2018).

12. N.X. Chung, R. Limpens, C. de Weerd, A. Lesage, M. Fujii and T. Gregorkiewicz. Towards practical carrier multiplication: donor/acceptor co-doped Si nanocrystals in SiO_2. *ACS Photon.*, DOI:10.1021/acsphotonics.8b00144 (2018).

13. C. de Weerd, F.C.M. Spoor, L.D.A. Siebbeles and T. Gregorkiewicz. Twee voor de prijs van één in germanium quantum dots. *Nederlands Tijdschrijft voor de Natuurkunde*, 81 (2015).

14. S. Saeed, C. de Weerd, P. Stallinga, F.C.M. Spoor, A.J. Houtepen, L.D.A. Siebbeles and T. Gregorkiewicz. Carrier multiplication in germanium nanocrystals. *Light: Sci. Appl.*, 4, e251 (2014).

Acknowledgements

This final part is usually the most read Chapter of the thesis: the acknowledgments. Why this is somehow much more appealing is a mystery to me because surely, how can there be a more interesting read than my research?! Nevertheless, here I get the chance to thank and address everyone who has been a major support for me during my very, extremely, tough time as a PhD researcher. So sit back, and enjoy.

First of all, I would like to thank... my cats! No just kidding: the person who definitely deserves the first call for gratitude is my promoter Prof. dr. Tom Gregorkiewicz. I find it amazing how you can inspire people and bring out the best in everyone; in me. I remember starting in your group as an unexperienced, incoherently presenting and talking (quite nervous) master student. I remember the first international conference where I gave my first talk - sheepishly - and I recall our last Physics@Veldhoven conference, where I proudly (but completely unaware) presented myself as a post-doc in the group of Prof. Tom Gregorkiewicz. This to great amusement to the rest of the group and most of my promotion committee members, who also happened to be there. In any case, it only stresses more how much I have learned from you during the past five years. There was never a moment things could not be discussed and your door is always open. My thanks for all your support and the opportunities you have given me.

Next in line are my group members, especially Leyre. There are many reasons I've asked you to be one of my paranymphs. Without your addition to the group I doubt my PhD would have been as successful as it is now. We are a great team and it has only been effortless and a pleasure working with you. I wish you all the best and luck in your further career. Antonio and Emanuele, my two favorite Italians :p we should visit again the epic swan-guy, eat many cannoli and enjoy some more tropical rains! Arnon, Bart, Elinore, Chung, Lucas, some of you have already left TGG but we shared a lot, worked together, visiting conferences and it has been a great time together as a group. Lucas, I hope you will enjoy your PhD as much as I did and wish you all the best and success.

I have been lucky to collaborate with two fantastic groups in Japan: the group of Prof. Fujiwara at Osaka University and the group of dr. Suenaga at the AIST research center in Tsukuba. It has been my pleasure visiting your labs and I would like to thank you for giving me the opportunity to finalize some experiments. I also want to thank Prof. Ashida and Prof. Matsubara and Delphine for their help and support with the experiments during my stay in Osaka. And thank you Junhao, for your help and support with the EELS experiments. I also want to express my gratitude to Prof. Laurens Siebbeles, who is also in my committee, for allowing me to use the ultrafast setup. All these collaborations have lead to fruitful experiments and beautiful papers, and this nice thesis. I would also like to thank the remaining members of my promotion committee for taking the time to evaluate this thesis and your efforts during shared projects: Prof. Wim Sinke, Prof. Jan Linnros, Prof. Jaime Gomez Rivas, Prof. Mark Golden, Prof. Peter Schall and Prof. Hong Zhang.

Next in line are my friends. First of all Michèle, who is going on an amazing adventure and unfortunately cannot be present during the defense. We have known each other basically all our lives and I hope it will stay like that. May many more holidays, adventures and krokantie garanties en daar, en daar, en DAARR's cross our paths. Tamira, you are one of those instant friends. We

saw each other and decided we'd be best friends from that day on <3. You are the sweetest most warm and caring person with a character I know! Tamara, best partner ever! We have shared so much, went through all those competitions together - with related highs and lows. I'm happy you'll stand by me once again as my paranymph! Merrit, dude, moge wij nog vele dansjes doen. Thanks to Nerds for being nerds and Team from Den Haag for becoming my friends. Paaldansjuffies: I'm part of a great, fun team and I'm thankful for that.

Of course I want to thank my parents who have ever been supportive and stimulated my long path towards finishing my PhD successfully. You are always there for me and I cannot be thankful enough for that. Harry, thank you for being the best bonus-vader ever. I'm delighted to see how you and my Mom are happy together also with Shiva. Heleen, you are making my Dad happy which makes me happy. Daan en Rosan, my bonus brother and sister :) I also want to thank Huize de Jong: Ina, Henri, Jip, Chantal, Sam, Henk en Joke. I'm looking forward to another week of cappo'tjes and koekjes and playing with Finn and Liam in the swimming pool. Tante Joke en Oom Rob and the whole Mulder family, it would be too much to name everyone but I'm grateful I've come from such a warm and loving family. Lieve Fien, even though we do not see each that often: wat in een goed vat zit verzuurd niet.

And of course I have to note that I am very happy with all the love and attention of Stapper and Fitz. Although, not so much at 4am in the morning. They will be extra thought of when I'm defending this thesis on World's Animals day the 4th of October. But the very last person who earns this special position of eternal gratitude is Liefje or: lief, liefjuuuh, liehief, LIEFFIE! You are always there for me, copes with my hangry moments and my gnarls and snarls from time to time. Without you, my PhD journey would have been less pleasant. I love you to the moon and back!